

Copyright
by
James Ryan Phillips
2017

**The Thesis Committee for James Ryan Phillips
Certifies that this is the approved version of the following thesis:**

**Field Evaluation of Reinforced Asphalt Overlays using Strain
Measurements**

**APPROVED BY
SUPERVISING COMMITTEE:**

Supervisor:

Jorge G. Zornberg

Gholam Hossein Roodi

**Field Evaluation of Reinforced Asphalt Overlays using Strain
Measurements**

by

James Ryan Phillips

Thesis

Presented to the Faculty of the Graduate School of

The University of Texas at Austin

in Partial Fulfillment

of the Requirements

for the Degree of

Master of Science in Engineering

The University of Texas at Austin

December 2017

Dedication

This is for my father, who never left my side throughout this journey.

Acknowledgements

I would like to thank Dr. Jorge Zornberg for his guidance throughout my research and for the many opportunities he has presented to me. I could not imagine where I would be if Dr. Zornberg had not convinced me to do research with him during my undergrad. I would also like to thank the University of Texas at Austin for being the best school on the face of the earth and for accepting me with open arms. I would also like to thank the Texas Department of Transportation for their funding and assistance with the project installation and details. I would also like to thank Mike Samueloff and the Huesker team for providing materials and assistance with my project. I would also like to thank all the members of our research group for the positive discussions and insights they have provided. Our team is very unique, to say the least, and I will never forget our experiences together. I would like to specifically thank the veteran researchers: Chris Armstrong, Hossein Roodi, Amr Morsy, Subu Sankaranarayanan, Larson Snyder, Jakob Walter, and Jose Martinez Dauhajre for their friendship and guidance through the ups and downs of graduate school. You guys have been by my side from the beginning, showing nothing but positivity and support. I am thankful for the teams that helped with installation and testing of our project site along US77: Federico Castro, Luming Yang, Liming Zheng, and the veteran researchers previously mentioned. This project would have never been possible without the early morning and overnight installation sessions. I am also thankful for the assistance and friendship of the students visiting from Brazil: Paulo Henrique Rossi Vieira, Ivan Martins, and Elisson Pereira da Silva. I learned as much from you as you did from me and I know each of you has a bright future ahead. Lastly, I want to thank my friends and family who have supported me unconditionally

throughout my schooling. Y'all always said the end would come sooner than you realize, and here we are.

Abstract

Field Evaluation of Reinforced Asphalt Overlays using Strain Measurements

James Ryan Phillips, M.S.E.

The University of Texas at Austin, 2017

Supervisor: Jorge G. Zornberg

The design of paved surfaces under different geological, environmental, and inclement scenarios is a topic of major relevance within the geotechnical and transportation engineering discipline. Roads and other paved surfaces should be adequately maintained for both civilian and commercial operations to thrive. Pavement deterioration is inevitable as are the associated maintenance costs. Techniques to prevent and mitigate pavement deterioration typically become more expensive as the expected service life is increased. This research focuses on the inclusion and evaluation of geosynthetic-reinforced asphalt overlays. Specifically, polyester (PET) and polyvinyl (PVA) geogrid reinforcement was installed and evaluated using strain measurements from subsurface asphalt layers to further understand the associated structural benefits and mitigation of reflective cracking. The presence of interlayer reinforcements is expected to increase the service life of constructed overlays and eventually lead to less overall costs in road maintenance.

A field monitoring site located along US77 in Lee County, Texas is the focus of this research. This road is a four-lane highway that has shown significant reflective cracking through multiple overlays. PET and PVA geosynthetic-reinforcements were installed in 500 ft. sections followed by an unreinforced control section. Each of these sections was instrumented with asphalt strain gages placed at two inches below the surface of the overlay. The strain gages were arranged in the longitudinal and transverse directions located in the right wheel path as well as between the wheel paths. Two sensors in each section were placed on a preexisting crack. A testing campaign was

conducted one year after installation that included vehicle passes by a heavy dump truck and a pickup truck. The passes were conducted directly over the sensors in the wheel path as well as offset towards the shoulder. Static testing was also performed by the heavy truck, in which the truck stopped directly on each sensor for a period of time. Falling weight deflectometer (FWD) tests were also conducted on each sensor to assess the development of the strains from each drop. The sensor configuration allowed the comparison of measured strains between the two types of reinforcement as well as between the reinforced sections and the unreinforced section.

The PET reinforced section was found to consistently develop lower strains under traffic loads than the control section, both in terms of longitudinal strain in the wheel paths and over preexisting crack locations. The PVA reinforcement also showed the development of lower strains over preexisting cracks than the control section. Both reinforced sections showed development of higher strains than the control section in the area between the wheel paths, indicating the load was distributed over a comparatively greater area, which is expected to ultimately lead to comparatively low rutting.

Table of Contents

List of Tables	xii
List of Figures.....	xiii
Chapter 1. Introduction	1
1.1 Motivation.....	1
1.2 Overall Objective.....	2
1.3 Specific Objectives.....	2
1.4 Thesis Structure.....	3
Chapter 2. Literature Review	4
2.1 Geosynthetics in Pavement Systems	4
2.2 Mitigation of Reflective Cracking	4
2.3 Mechanisms of Asphalt Reinforcement.....	5
2.4 Previous Studies on Reinforced Asphalt.....	8
2.5 Asphalt Reinforcement Installation Method.....	11
2.6 Concerns Regarding Asphalt Reinforcement.....	11
Chapter 3. Project Details.....	13
3.1 Site Characterization.....	13
3.1.1 Location	13
3.1.2 Subgrade Soil Information.....	15
3.1.3 Site Conditions	16
3.1.4 Previous Site Construction	18
3.1.5 Pre-Construction Evaluation.....	19
3.1.5.1 GPR.....	19
3.1.5.2 FWD	20
3.1.5.3 Traffic Counts.....	20
3.2 Field Testing Design.....	21
3.2.1 Materials	21
3.2.2 Test Section Location.....	22

3.2.3	Test Section Sequence	25
3.2.4	Sensor Locations.....	25
3.3	Installation of Geosynthetic Reinforcements	28
3.3.1	Overlay Construction	28
3.3.2	Reinforcement Installation	30
3.3.3	Sensor Installation.....	32
3.4	Collection of Field Data	34
3.4.1	Strain Measurements Using Asphalt Strain Gages.....	34
3.4.2	Asphalt Strain Gages.....	37
3.4.2	Data Logger.....	37
3.4.2.1	DATAQ data logger.....	37
3.4.2.2	National Instruments (NI) data logger	39
Chapter 4.	Field Testing Campaign	41
4.1	Identification of Sensor Locations	41
4.2	Vehicle Passes	43
4.3	Falling Weight Deflectometer Testing	44
4.4	Static Loading.....	45
Chapter 5.	Results of Field Campaign	47
5.1	Controlled Testing Campaign.....	47
5.1.1	Traffic Loading.....	47
5.1.1.1	Data Evaluation	47
5.1.1.2	Heavy Load Passes Directly Over Sensors	49
5.1.1.3	Light Load Passes Directly Over Sensors.....	59
5.1.1.4	Effect of Driving Offset of Sensors.....	66
5.1.2	Falling Weight Deflectometer Tests.....	68
5.1.2.1	Data Analysis.....	69
5.1.2.2	Comparison of Strain Data.....	70
5.1.3	Static Testing.....	74
5.1.3.1	Data Analysis.....	74

5.1.3.2	Comparison of Strain Data.....	75
5.2	Discussion	80
5.2.1	Structural Benefits from Geosynthetics in Asphalt Overlays	80
5.2.2	Mitigation of Reflective Cracks by Geosynthetics in Asphalt Overlays.....	81
Chapter 6.	Conclusions	82
References.....		85

List of Tables

Table 1: Atterberg Limit of Luling Clay	16
Table 2: Physical properties of HaTelit products.....	22

List of Figures

Figure 1: Use of geosynthetics in mitigation of reflective cracking in asphalt overlays: a) Roadway designed without geosynthetics, b) Roadway designed with geosynthetics (Zornberg 2017a.)	6
Figure 2: Crack propagation theory: a) Preexisting cracks below overlay without reinforcement; b) Preexisting cracks below overlay with reinforcement; c) Stress distribution without reinforcement; d) Stress distribution with reinforcement (Paris and Erdogan 1963)	7
Figure 3: Schematic of test setup (Khodaii et al. 2009).....	8
Figure 4: Progression of reflective cracks at 20° C for: a) geogrid reinforced (embedded at one-third) overlay; b) unreinforced overlay (Khodaii et al. 2009).....	9
Figure 5: Detail of extracted specimen: a) preexisting cracks stopped at grid location; b) top down cracking in the reinforced section (Montestruque, et al. 2012).	10
Figure 6: a) Test layout; b) crack propagation equipment; c) crack activity meter (Montestruque, et al. 2012).	11
Figure 7: US77 overlay project location: a) relative to Austin; b) within Lee County; c) Google Earth view	14
Figure 8: US77 subgrade properties: a) USDA soil survey; b) sieve analysis; c) swell test	15
Figure 9: Images of transverse cracking along US77.....	17
Figure 10: Images of longitudinal cracking along US77.....	18
Figure 11: GPR scan of US77 before overlay construction	19

Figure 12: Asphalt and base thickness back calculated from FWD at US77	20
Figure 13: US77 traffic counts: a) northbound; b) southbound	21
Figure 14: GPR scan on US77 before overlay construction	23
Figure 15: GPR scan of chosen test section location.....	23
Figure 16: Elevation profile for US77	24
Figure 17: Overhead view of US77 overlay	24
Figure 18: US77 test section layout.....	25
Figure 19: Sensor layout for: a) Section 1; b) Section 2; c) Section 3.....	27
Figure 20: Approximate sensor location within each section.....	28
Figure 21: US77 overlay construction during: a) tack coat application for chip seal; b) aggregate placement for chip seal; c) asphalt placement; d) asphalt leveling	29
Figure 22: Interlayer installation sequence: a) looping tow strap through tack truck bumper and evening the strap; b) tack application and initial installment; c) continued installment and monitoring.....	31
Figure 23: Sensor installation steps: a) pavement marking; b) pavement cutting; c) sensor placement	33
Figure 24: Patch placed over the sensors in: a) Section 1; b) Section 2; c) Section 3	34
Figure 25: Strain gage output: a) functioning sensor under traffic; b) erratic sensor output under traffic; c) excessive noise; d) not responding under traffic (Timm et al., 2004).....	35
Figure 26: Methodology for reducing strain gage data (Scholz, 2010).....	36
Figure 27: ASG 152: a) image; b) specifications.....	37
Figure 28: DATAQ data acquisition: a) data logger; b) strain gage amplifiers.....	38

Figure 29: Specification sheet for: a) DATAQ data logger; b) strain gage amplifier	39
Figure 30: National Instruments data acquisition system components: a) PCI-E 6323 multifunction I/O device; b) SCXI 1349 adapter; c) SCXI 1520 strain/bridge input module; d) SCXI 1001 chassis; e) SCXI 1314 terminal block.....	40
Figure 31: Handheld GPR for sensor location: a) GPR device; b) scan showing sensor flanges; c) permanent marking for sensor location.....	42
Figure 32: Vehicles used for trafficking: a) heavy load (dump truck); b) light load (pickup truck).....	43
Figure 33: Vehicle pass diagram for: a) direct passes; b) offset passes	44
Figure 34: FWD equipment used during controlled testing campaign.....	45
Figure 35: Maneuvering dump truck directly on the sensors during static testing	46
Figure 36: Example asphalt strain gages data recorded under controlled trafficking: a) heavy load (dump truck) trafficking; b) light load (pickup truck)....	48
Figure 37: Example of vehicle pass strain data shown in: a) tabular form; b) bar and whisker plot.....	49
Figure 38: Section 1 Strain Response for Heavy Loading: a) trafficking at 15mph; b) trafficking at 25mph.....	51
Figure 39: Section 2 Strain Response for Heavy Loading: a) trafficking at 15mph; b) trafficking at 25mph.....	52
Figure 40: Section 3 Strain Response for Heavy Loading: a) trafficking at 15mph; b) trafficking at 25mph.....	53
Figure 41: Longitudinal ASG in Wheel Path Not on Crack Section 1 and Section 3 for Heavy Loading: a) trafficking at 15mph; b) trafficking at 25mph...	55

Figure 42: Transverse ASG in Wheel Path Not on Crack Section 1 and Section 3 for Heavy Loading: a) trafficking at 15mph; b) trafficking at 25mph...56

Figure 43: Transverse ASG Between Wheel Paths Not on Crack Section 2 and Section 3 for Heavy Loading: a) trafficking at 15mph; b) trafficking at 25mph. 57

Figure 44: Longitudinal ASG in Wheel Path on Crack Section 1 and Section 3 for Heavy Loading: a) trafficking at 15mph; b) trafficking at 25mph...58

Figure 45: Longitudinal ASG Between Wheel Paths on Crack Section 2 and Section 3 for Heavy Loading: a) trafficking at 15mph; b) trafficking at 25mph.59

Figure 46: Section 1 Strain Response for Light Loading: a) trafficking at 15mph; b) trafficking at 25mph..... 60

Figure 47: Section 2 Strain Response for Light Loading: a) trafficking at 15mph; b) trafficking at 25mph..... 61

Figure 48: Section 3 Strain Response for Light Loading: a) trafficking at 15mph; b) trafficking at 25mph..... 62

Figure 49: Longitudinal ASG in Wheel Path Not on Crack Section 1 and Section 3 for Light Loading: a) trafficking at 15mph; b) trafficking at 25mph. 63

Figure 50: Transverse ASG Between Wheel Paths Not on Crack Section 2 and Section 3 for Light Loading: a) trafficking at 15mph; b) trafficking at 25mph. 64

Figure 51: Longitudinal ASG in Wheel Path on Crack Section 1 and Section 3 for Light Loading: a) trafficking at 15mph; b) trafficking at 25mph. 65

Figure 52: Longitudinal ASG Between Wheel Paths on Crack Section 2 and Section 3 for Light Loading: a) trafficking at 15mph; b) trafficking at 25mph.66

Figure 53: Heavy Load Offset Passes at: a) 15mph; b) 25mph..... 67

Figure 54: Typical strain response from FWD drops: a) Plotted; b) Tabulated with peak values from each drop; c) shown in stacked column chart..... 69

Figure 55: Longitudinal strain in wheel path away from a crack for FWD testing71

Figure 56: Transverse strain between wheel paths away from a crack for FWD testing 72

Figure 57: Longitudinal strain in wheel path on a crack for FWD testing..... 73

Figure 58: Longitudinal strain between wheel paths on a crack for FWD testing 74

Figure 59: Static Loading by Heavy Load for Sensor 14..... 75

Figure 60: Longitudinal strain in wheel path away from a crack for static testing77

Figure 61: Transverse strain between wheel paths away from a crack for static testing 78

Figure 62: Longitudinal strain in wheel path on a crack for static testing 79

Figure 63: Longitudinal strain between wheel paths on a crack for static testing 80

Chapter 1. Introduction

1.1 MOTIVATION

The design of paved surfaces under different geological, environmental, and inclement scenarios is a topic of major relevance within the geotechnical and transportation engineering discipline. Roads and other paved surfaces should be adequately maintained for both civilian and commercial operations to thrive. Pavement deterioration is inevitable as are the associated maintenance costs but recent advances in preventative measures and pavement rehabilitation have helped to mitigate these costs. The use of geosynthetic interlayer reinforcement is becoming increasingly used in roadways, runways, and other paved surfaces. This technique has shown significant promise in the extension of pavement service life that lead to lower maintenance costs.

Enhancing pavements with geosynthetic is becoming a common practice where flexible and rigid pavements are being rehabilitated via the construction of asphalt overlays. Interlayer geosynthetics are produced in various configurations, including a geogrid, geotextile, or composite forms. When utilized properly, geosynthetic interlayers have been reported to minimize moisture infiltration, decrease stresses, and decrease the propagation of reflective cracks. While geosynthetics have often been used for stabilization of base and subgrade layers, their use as a reinforcing interlayer within hot mix asphalt has been comparatively less common. This might be due to the lack of experimental data on reinforcing interlayer geosynthetics. The use of a geosynthetic interlayer is expected to result in structural benefits in the pavement. However, the underlying reinforcement mechanisms and interaction with pavement layers have not yet been fully understood.

Flexible pavements consist primarily of aggregate and bitumen. The aggregate provides resistance to compressive forces but has no effect the on tensile strength. Bitumen is the glue that holds the aggregate together and provides a still relatively low tensile strength. Therefore, a pavement mixture does not perform well under tensile stresses. As vehicles pass over a pavement section, vertical loads cause the upper portion of the pavement section to be under horizontal compression. Similar to a beam, the lower portion of a given pavement section develops tensile stresses. As the pavement is repeatedly loaded from traffic, the area of tensile strain becomes weaker and can eventually fail due to fatigue. It is at this location that geosynthetics can be placed to decrease the magnitude of tensile strains. Interlayer geosynthetics

are commonly manufactured using materials with comparatively high tensile strength. When bonded to a flexible pavement, the overall system has an increased tensile capacity. Under vehicle loading, the geosynthetic tensile strength is mobilized, which decreases the overall tensile strains exhibited by the pavement. Consequently, the service life of the pavement is extended.

Beam tests have been conducted on reinforced pavement specimens but type of results have not reproduced the conditions associated with dynamic traffic loading. Therefore, this research aims at improving the understanding of strains development in reinforced asphalt layers under actual field conditions and for different loading conditions. Specifically, a field site containing two test sections with different interlayer reinforcing materials and a control section was constructed for this study. The influence of the geosynthetics was examined through strain measurements collected immediately below the installed interlayer. The findings of this study are expected to provide relevant information on the structural benefits of geosynthetic interlayers under actual traffic conditions.

1.2 OVERALL OBJECTIVE

The overall objective of this research is to evaluate the benefits associated with the use of asphalt geosynthetic-reinforcements within flexible pavements. This study investigates the strain response of pavement sections during the post-construction period of an asphalt overlay constructed using different interlayer reinforcements. Traffic loading involved multiple passes of a loaded vehicle as well as a pickup truck to represent heavy commercial and private vehicles. This information is expected to provide understanding on the mechanisms in reinforced asphalt overlays with emphasis on the structural improvements. Testing was conducted on field sections that were specifically constructed for this research.

1.3 SPECIFIC OBJECTIVES

In order to achieve the overall objective, this research seeks the following specific objectives:

- Construct a field site with different sections involving geosynthetic interlayer reinforcements and instrumentation to assess different loading mechanisms.

- Compare the performance of reinforced pavement sections with that of an unreinforced pavement section.
- Compare the performance of different geosynthetic reinforcement products within reinforced pavement sections.
- Compare the horizontal strains that develop within overlay sections associated with different loading mechanisms.
- Understand the structural benefits of interlayer reinforcement.
- Understand the effect of interlayer reinforcement in mitigation of reflective cracking.

1.4 THESIS STRUCTURE

This thesis includes 6 chapters. Chapter 1 includes the motivation and objectives for this research. Chapter 2 provides the background information on the key components associated with this research. This information includes the geosynthetic interlayer applications, benefits of geosynthetic-reinforced pavement structures, and use of asphalt strain gages within pavement structures. Chapter 3 includes the US77 overlay project information, project site details, basis for section location and design, geosynthetic materials, instrumentation, installation details, and data acquisition. Chapter 4 provides information regarding the controlled testing campaign conducted at the project site. Chapter 5 includes the field monitoring results from the pavement sections obtained from a sequence of field testing programs. Chapter 6 includes the final discussion and conclusion based on the obtained results, which compares the reinforced sections with different products to the control section.

Chapter 2. Literature Review

2.1 GEOSYNTHETICS IN PAVEMENT SYSTEMS

Geosynthetics have been used to enhance performance of various pavement layers. Zornberg (2017a, 2017b) discussed the various functions (including separation, filtration, reinforcement, stiffening, and drainage) that geosynthetics can potentially fulfill when used in different pavement layers. Specifically, geosynthetics have been used in base stabilization applications to fulfill a stiffening function and in subgrade stabilization to fulfill the stiffening, reinforcement, separation, and drainage function (e.g., Al-Qadi et al., 2008; Zornberg et al., 2012). Design properties to fulfill stiffening and reinforcement functions may be distinctively different (e.g., Roodi, 2016; Roodi and Zornberg, 2017; Zornberg et al., 2017). Geosynthetics have also been used within the hot mix asphalt concrete to enhance its structural capacity or to mitigate reflective cracking between asphalt layers (e.g., Perkins et al., 2010; Ferrotti et al. 2012; Brown et al., 2001). A concern regarding this application is a de-bonding effect which is described as the loss of adhesion between adjacent asphalt layers due to presence of the inclusion (e.g., Zamora-Barraza et al., 2010; Roodi et al., 2017). This research aims at gaining better understanding on the impact of geosynthetic reinforcement interlayer in hot mix asphalt. Aspects of the literature that are particularly relevant to this application are discussed next.

2.2 MITIGATION OF REFLECTIVE CRACKING

Reflective cracking (RC) is a major distress type in new asphalt layers constructed on previously cracked pavements. Reflective cracking typically develop in a new asphalt overlay at the location of preexisting cracks within the old pavement. The repeated loading from traffic can trigger bending and/or shear stresses of high intensity at the crack location. Reflective cracking can also occur due to thermal expansion or contraction within the pavement. As these cracks reach the surface, the pavement becomes vulnerable to moisture infiltration that may lead to early failure. (Zornberg 2017a). There are four main reflective cracking mitigation methods. First, reflective cracking can be mitigated by modifying or strengthening the existing pavement surface. The fracture resistance of asphalt mixture can be improved by using asphalt rubber modified mixture and polymer modified asphalt mixture (Zhang et al. 2012). Varying the thickness of HMA overlays is also an option for RC mitigation (Vismara, et al. 2012). Second, treatments of existing pavements minimize RC. Such treatments usually involve milling, reclamation, or recycling of the existing pavement. Full depth reclamation is also a rehabilitation strategy for low volume roads (Jones, et al. 2016). Third, interlayer systems can be used in road rehabilitations. The concept behind the interlayer systems is to dissipate tensile strength at the existing crack tip. Various types of interlayers have

been used, including chip seals, interlayer stress absorbing composite, asphalt-rubber membrane interlayer, and fabrics. Lastly, geosynthetic interlayers have been used to mitigate the early development of reflective cracks. This is done through one or a combination of functions, including reinforcement, separation (or protection), and barrier (Perkins et al. 2010).

2.3 MECHANISMS OF ASPHALT REINFORCEMENT

As previously mentioned, a geosynthetic interlayer can provide reinforcement, separation, and a barrier for a pavement. The reinforcement function describes the development of tensile forces in the geosynthetic at the location of a crack that reduces the stresses felt by the bituminous material. The separation function refers to the geosynthetic providing a layer that allows horizontal deformations without transferring this movement through the new overlay. The barrier function corresponds to the waterproofing of the old pavement through bitumen-impregnated nonwoven geotextiles. More recent studies have reported that geosynthetic interlayers can not only mitigate the development of reflective cracks, but also increase the structural capacity of a pavement. Figure 1 a. shows a typical example of reflective cracking induced by localized stresses at the crack tip. In a geosynthetic-reinforced pavement, such as the one shown in Figure 1 b., the crack reaches the reinforcement then stops as the geosynthetic minimizes the induced stresses (Zornberg 2017a).

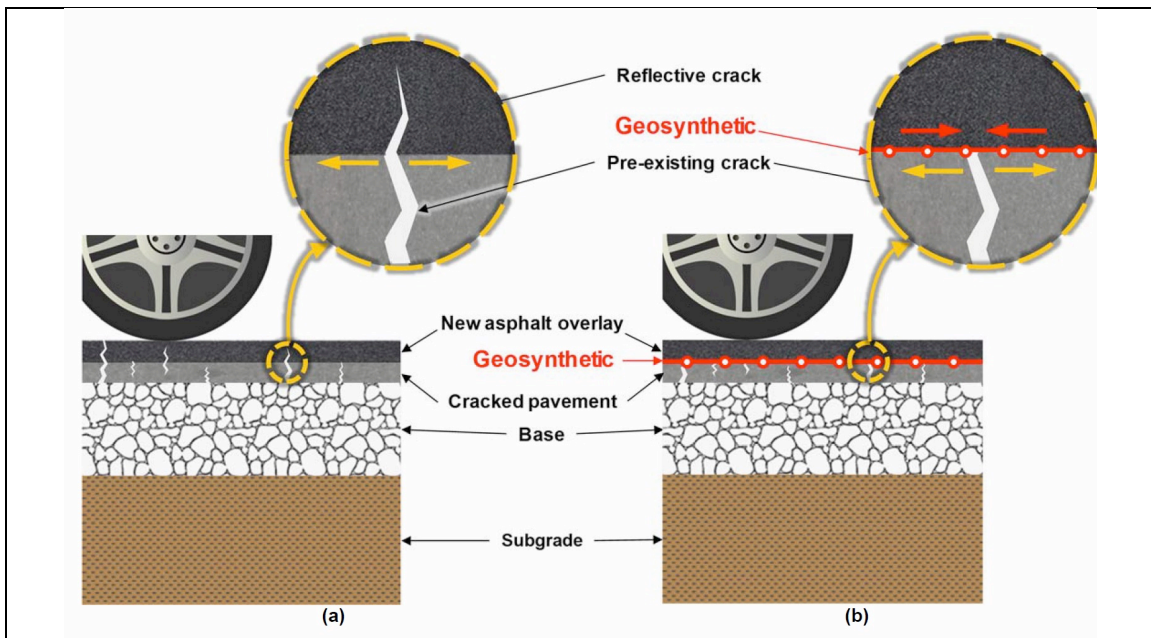


Figure 1: Use of geosynthetics in mitigation of reflective cracking in asphalt overlays:
 a) Roadway designed without geosynthetics, b) Roadway designed with geosynthetics (Zornberg 2017a.)

Asphalt reinforcements typically involve grids made of materials with high tensile strength and comparatively high stiffness. The open structure facilitates aggregate interlock between paving courses and restrains lateral movement of the aggregates. This structure enhances through-hole bearing capacity and allows stresses to be transferred to the grid by means of the interlocking aggregates of the asphalt layers. Square mesh aim at allowing equal lateral movements in both directions, while rectangular meshes restrict more lateral movement in one direction than the other. The size of the open structure should allow large aggregates to penetrate through. Otherwise, inadequately compacted spots may remain and could result in insufficient adhesion with the overlay (Nguyen, et al. 2013).

Reflection cracking is influenced by many factors such as interlayer stiffness and thickness, crack width, overlay stiffness and thickness, and depth of installation. Crack propagation theory helps to better understand crack reflecting mechanisms. Paris and Erdogan (1963) introduced the empirical fracture mechanics law that can be expressed as:

$$dc/dN = Ak^n \text{ (Paris and Erdogan, 1963)}$$

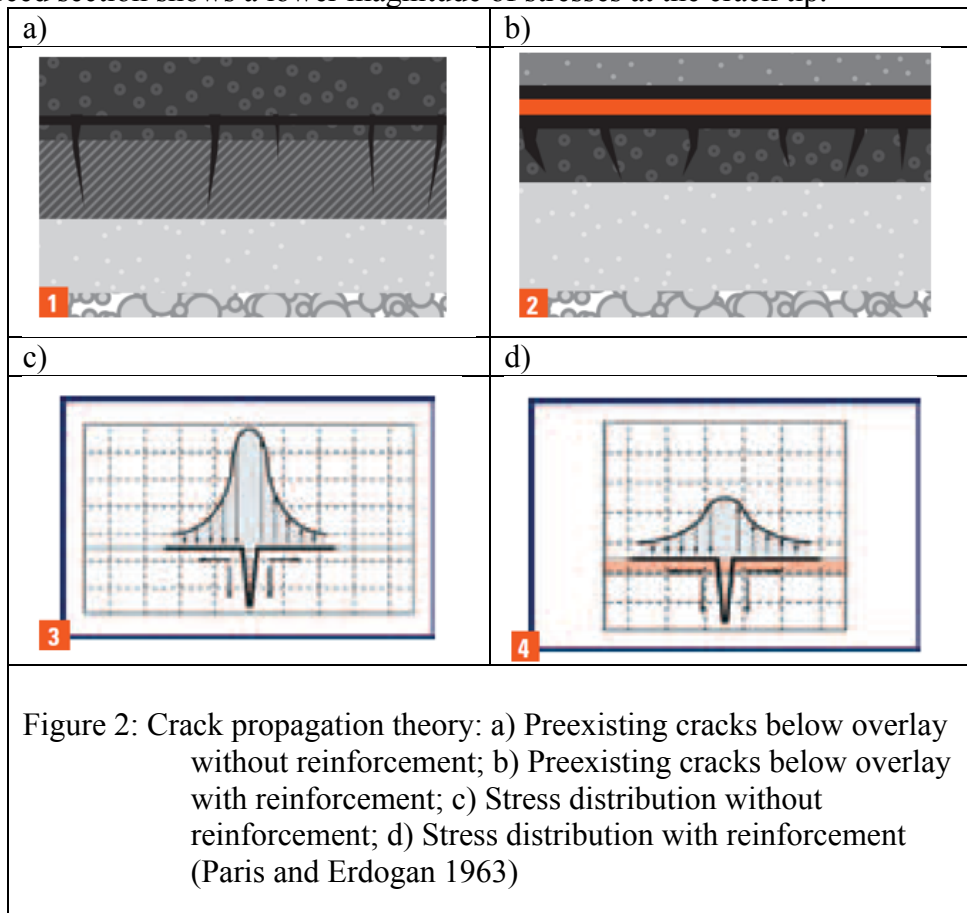
c = Crack length;

N = Number of load cycles to failure;

K = Stress intensity factor at crack tip;

A, n = Fracture properties of the material.

If the stress intensity factor at the crack tip decreases, the crack propagation will also decrease. This is theoretically possible with the inclusion of a reinforcement layer, which may reduce the tensile stress at the crack tip, as shown in Figure 2 b. (Paris and Erdogan 1963). At first, the crack propagates upward until it reaches the reinforcing interlayer. It then moves laterally until there is no longer sufficient energy available to move any further. Figure 2 c. and d. show the distribution of stresses from the crack. The reinforced section shows a lower magnitude of stresses at the crack tip.



Consequently, the interlayers may reduce the presence of reflective cracks in an overlay by creating a stress absorbing layer at the tip of an existing crack. Reinforcement adds tensile strength that is mobilized at small strains in the overlay. Thus, reinforcement interlayers reduce a pavement's susceptibility to cracking by increasing the pavement's flexural strength at low strains.

2.4 PREVIOUS STUDIES ON REINFORCED ASPHALT

The effects of geosynthetic overlays have been studied using several experimental approaches. One of such experimental setups involved testing an overlay placed on a preexisting pavement model with a synthetic crack. The overlay was repeatedly loaded by a hydraulic dynamic loading frame applying a force through a circular loading plate. Figure 3 shows the test setup for this experiment.

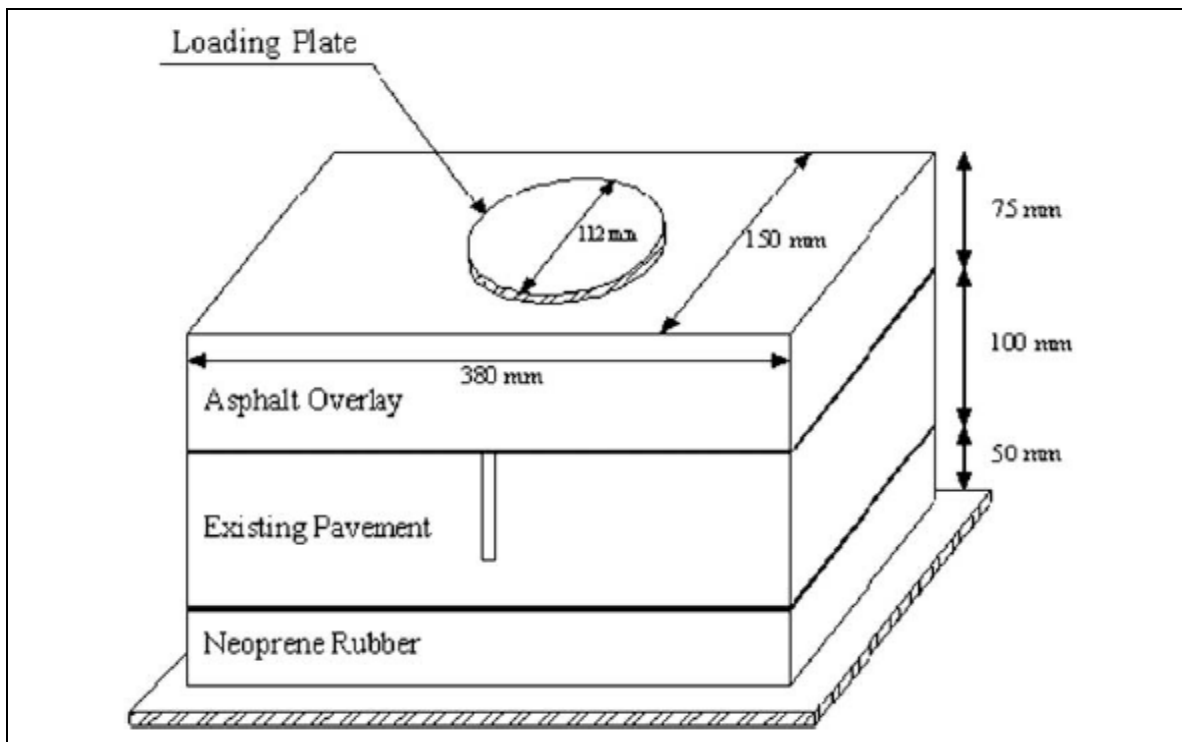
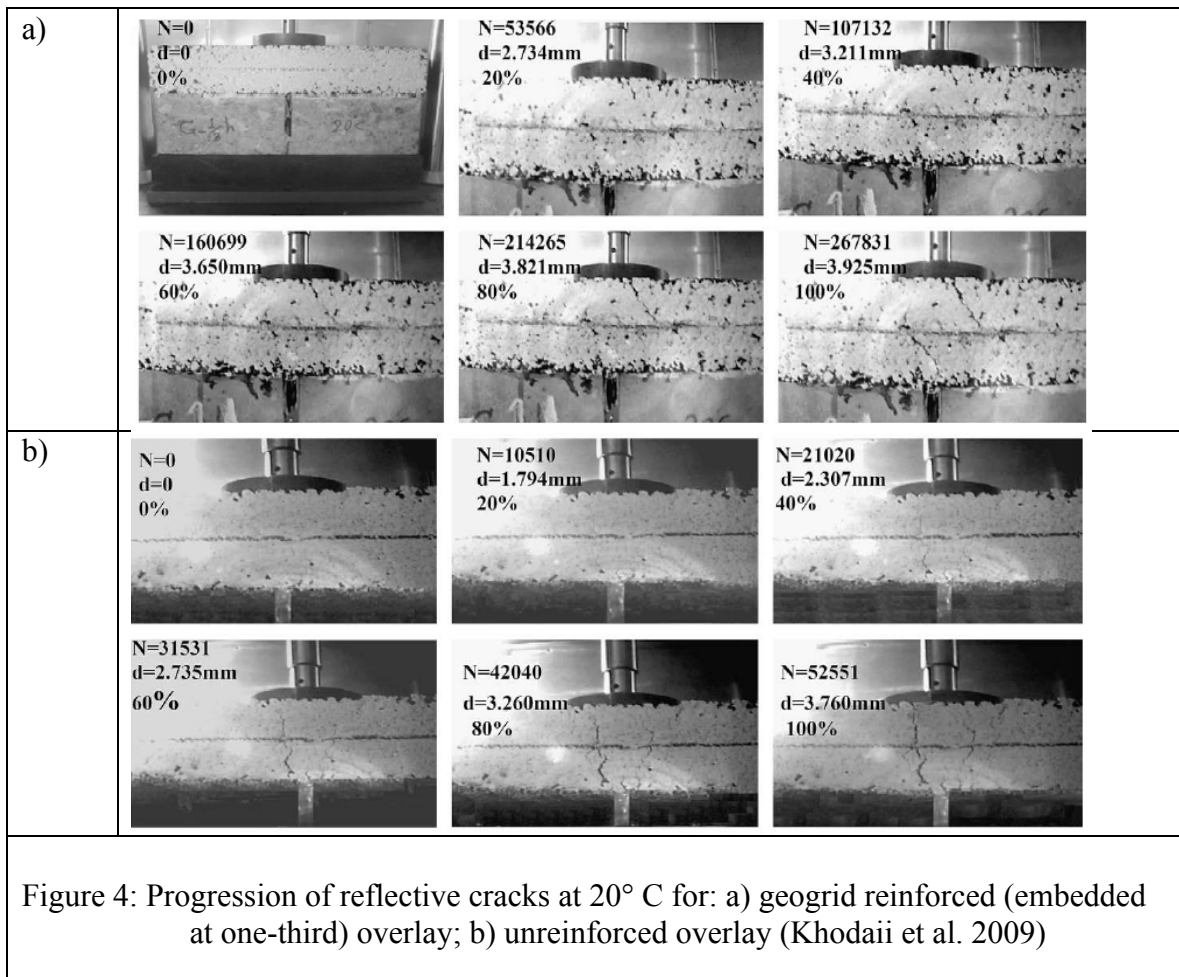


Figure 3: Schematic of test setup (Khodaii et al. 2009)

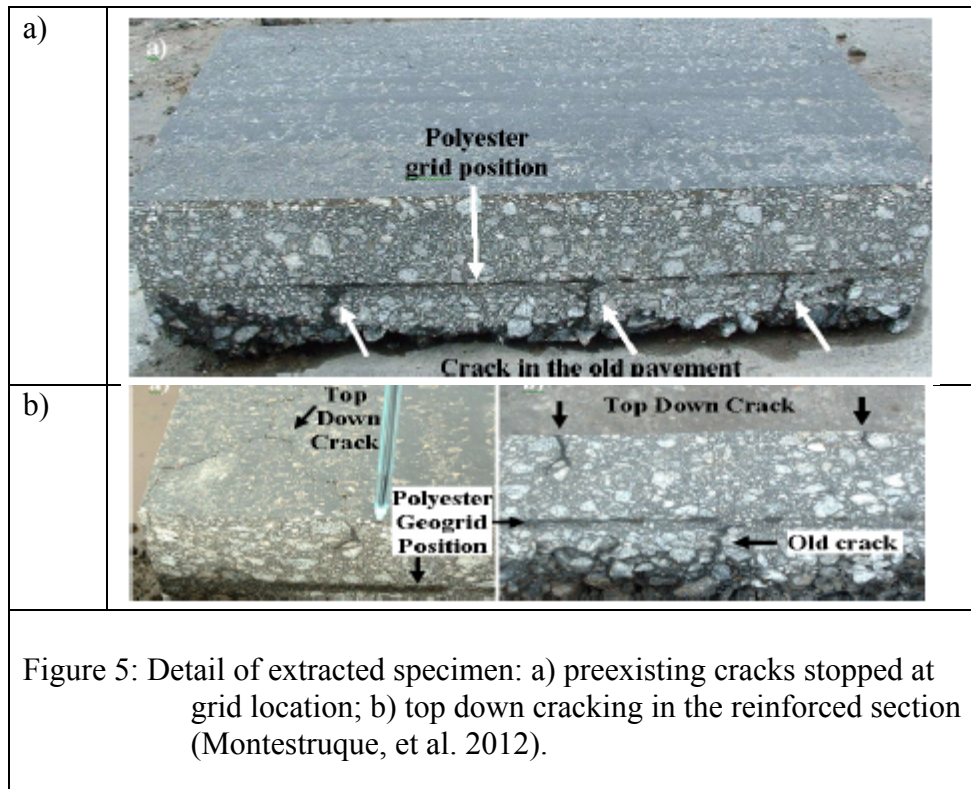
The width of the crack was varied between 10 and 20mm and the existing pavement was modeled by both a concrete and asphalt concrete slab. The location of the geosynthetic was varied between half, one-third, and at the bottom of the overlay. Figure

4 shows two test specimens: reinforced at one-third overlay embedment and unreinforced. The unreinforced specimen develops noticeable reflective cracking around 20, 000 cycles, whereas the reinforced specimen does not show obvious cracking through 100,000 cycles. This study concluded that geogrid inclusion in the asphalt leads to a significant increase in overlay performance regarding resistance to cracking and rutting (Khodaii et al. 2009).

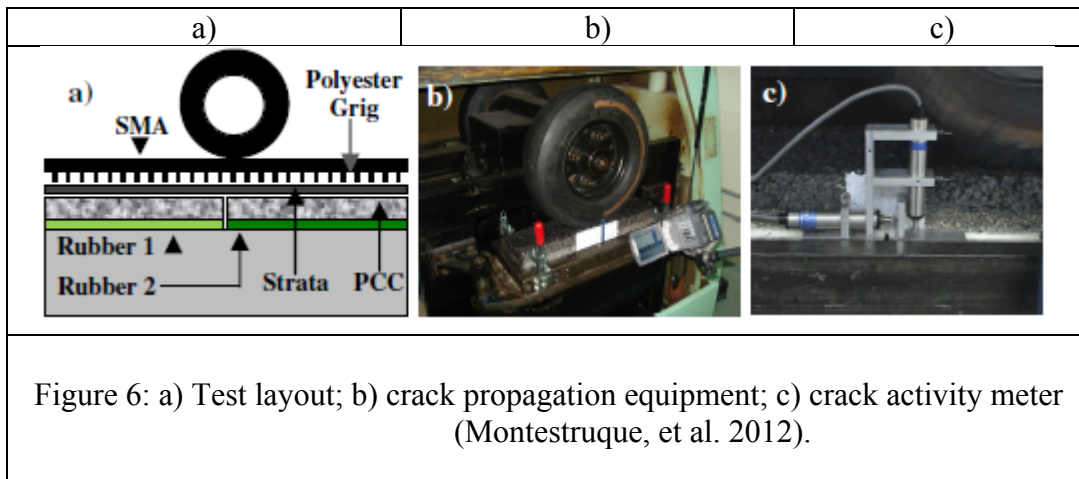


A series of tests were performed by Montestruque et al. (2012) on a field site with a 100m long test section. This section contained 50m of polyester interlayer reinforcement and 50m of unreinforced pavement. The entire length was contained preexisting cracks and had a 70mm overlay. A traffic simulator performed repeated cycles on the pavement sections. At 192 cycles, the unreinforced section shows clear reflective cracks. The reinforced section started showing cracks at 220 cycles. After pieces of the asphalt were extruded, it was determined that the reinforced section did not show reflective cracks, but instead showed top down fatigue cracking. Figure 5 shows the

extruded samples. In conclusion, the reinforcing polyester grid interrupted the crack propagation in the field specimens (Montestruque, et al. 2012).



Another test conducted by Montestruque et al. (2012) used a setup for wheel tracking rutting test to perform a wheel reflective cracking test. This testing series used three overlay systems: first was 60mm of HMA, second was the addition of 20mm of relief asphalt layer (strata), and third was the addition of a polyester grid. A crack activity meter (CAM) was used to measure crack behavior during the testing. The testing apparatus included the overlay, a preexisting asphalt layer containing a joint and a layer below the preexisting pavement with different rubber membranes. The rubber membranes had different densities in order to impose a differential vertical movement in the joint. Figure 6 shows the test setup and equipment used for this experiment. In conclusion, the strata had a retarding effect on crack initiation and propagation, and the reinforcing polyester grid interrupted the crack propagation (Montestruque, et al. 2012).



2.5 ASPHALT REINFORCEMENT INSTALLATION METHOD

Proper installation techniques of asphalt reinforcement are essential to achieve good bonding between the existing pavement and the new HMA overlay. The installation method for reinforced overlay in pavement construction involves four steps. First is surface preparation. It usually includes crack seal, milling, and leveling up. It is also important to clean any foreign material from before the reinforcement is placed to maximize the bond between the new layers. Second is tack coat application. The applied tack coat rate is usually 0.2 gal/yd² minimum at temperatures ranging from 20° to 50° C. The application rate has to provide enough tack to bond with the entire reinforcing surface. The tack coat also has to be properly distributed across the installation area. Third is geosynthetic placement, which involves unrolling the reinforcement evenly without creases to ensure the grid is placed in tension. Some manufacturers also recommend overlapping a portion of the reinforcement's edge when placing rolls side by side. Fourth is construction and compaction of the HMA overlay. The reinforcement is expected to be driven on by construction vehicles during this last step (Nguyen, et al. 2013).

2.6 CONCERNS REGARDING ASPHALT REINFORCEMENT

Several factors may affect the performance of geogrid-reinforced overlays, such as remedial work before overlay construction, installation quality, variability of strength in existing asphalt, base, and subgrade layers, traffic volume, and presence of moisture. The performance of asphalt reinforcement can range from clear success and increased overlay performance to failure. Failure has been reported to involve de-bonding that occurs between the new overlay and the existing pavement. De-bonding can lead to

increased deterioration of the new overlay due to excessive movement that results in pot holes or alligator cracking (Sobhan et al., 2003). This has influenced the use of different bonding products. Some reinforcements include a geotextile bonded to a geogrid, where the geotextile facilitates bonding when heated during the construction of the HMA overlay. These geotextiles can also be used to absorb the tack coat. The tack coat can range in effectiveness. The use of polymer-modified asphalt emulsion and pure asphalt cement has been reported to be highly successful (Chen et al., 2013).

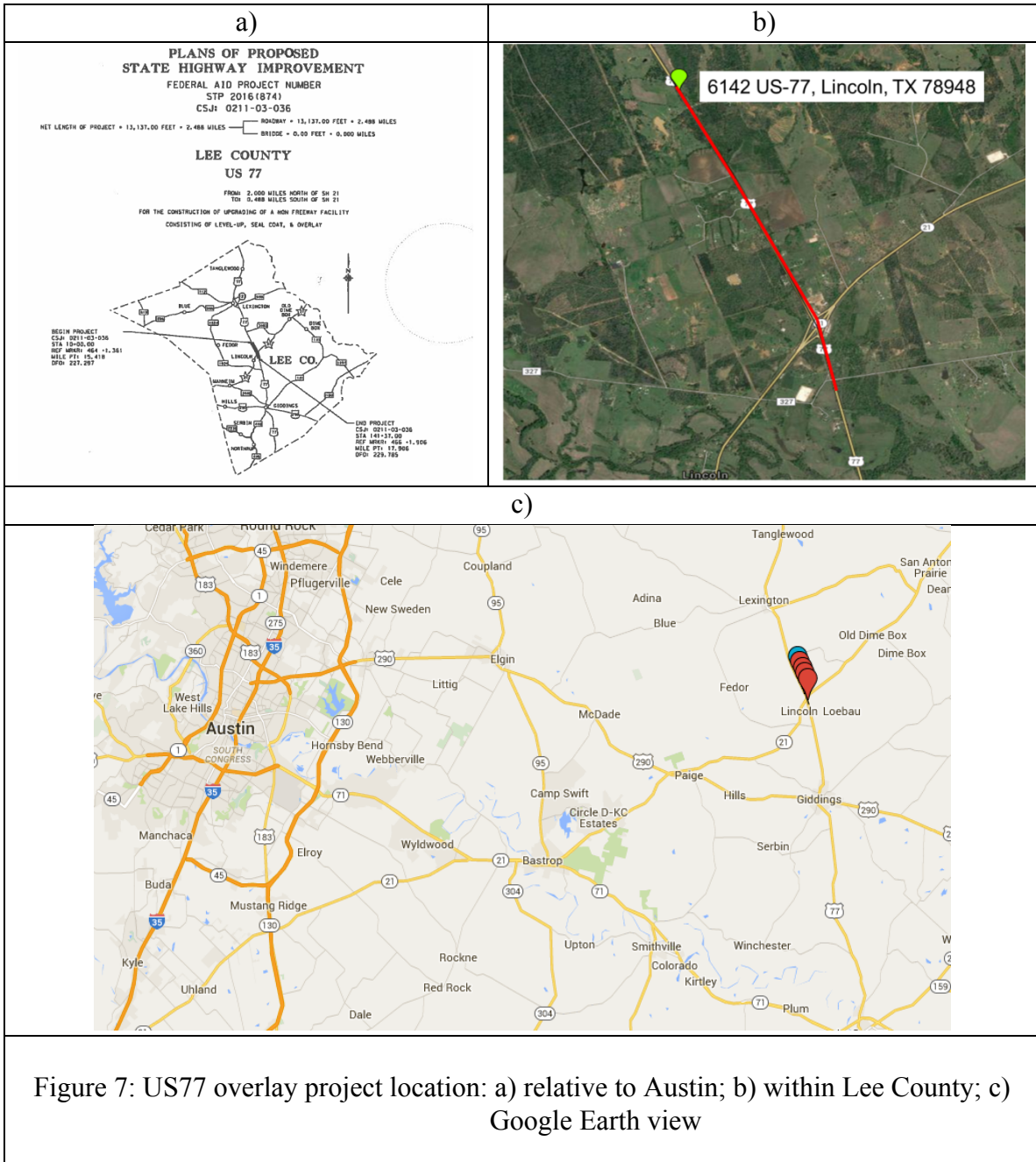
Proper installation of asphalt reinforcement is also essential for the bonding of the HMA overlay. A common mistake has been the lack of surface treatment of the preexisting asphalt. It is necessary to clean any foreign material from the road before placing the reinforcement. Also, any creases formed from unrolling the grid can result in air voids. This can be fixed by cutting the excess portion and compacting it before the overlay is placed, which allows the reinforcement to remain in tension (Vanelstraete et al., 2000).

Chapter 3. Project Details

3.1 SITE CHARACTERIZATION

3.1.1 Location

The location of the field monitoring project investigated in this study is Lee County, Texas, at the area along US-77 where it intersects with SH-21. The total length of the overlay project is 2.488 miles (see Figure 7 a.). It extends 2.0 miles north and 0.488 miles south of the SH-21 intersection. The coordinates of the intersection is (30.305556° N, -96.952500° S). An approximate address to the north end of the overlay is shown in Figure 7 b. Figure 7 c. includes a map showing the project location relative to Austin. It is approximately 57 miles from the University of Texas at Austin via Highway 290.



3.1.2 Subgrade Soil Information

The bulk of the overlay lies within an outcrop of Luling clay with some areas of Crockett gravelly fine sandy loam as shown by the soil survey map shown in Figure 8 a. A sample of the Luling clay was collected from the site to test the basic geotechnical properties of the soil.

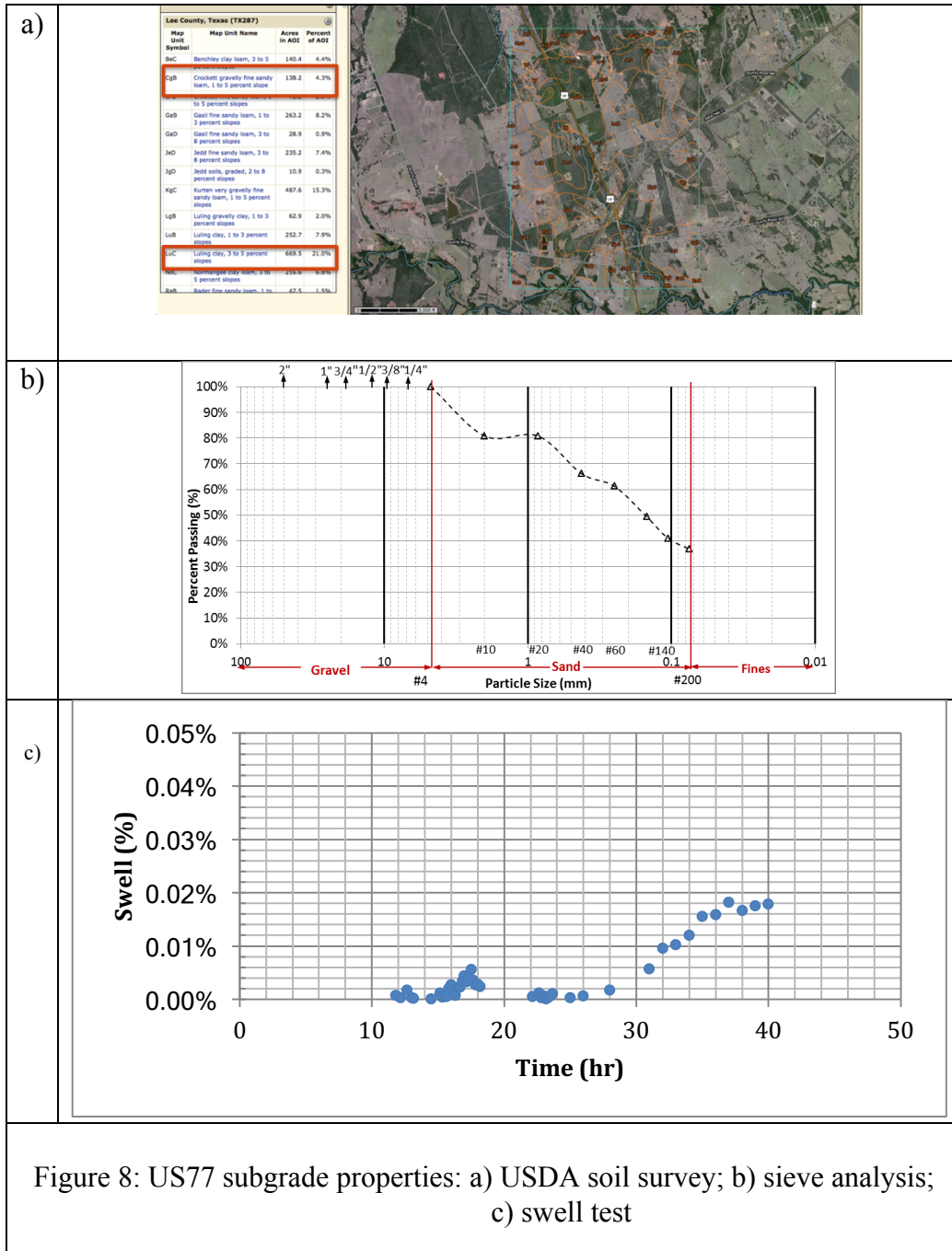


Table 1: Atterberg Limit of Luling Clay			
Test #	1	2	3
Predicted Liquid Limit, LL	36	36	36
Selected Liquid Limit, LL	36	36	36
Plastic Limit, PL	19	19	
Plasticity Index, PI	16	18	
Average Liquid Limit, LL	36		
Average Plastic Limit, PL	19		
Average Plasticity Index, PI	17		

Table 1 shows the results from Atterberg limit tests. The average liquid limit was found to be 36 and the average plastic limit is 19. This gives a plasticity index of 17, with the soil classifying as low plasticity clay (CL) based on the USCS classification. Figure 8 b. shows the results from the sieve analysis. The gradation curve indicates that the soil contains approximately 63% sand size particles and 37% fines. A one-dimensional swelling test using an oedometer setup was performed following *ASTM D4546 Method A* targeting a dry of optimum condition prescribed by NAVFAC at 125 psf. The strain versus time curve for the test is shown in Figure 8 c. After 40 hours, the soil swelled less than 0.02%. Based on these results, the soil was considered to be non-expansive.

3.1.3 Site Conditions

Photos taken during a field visit to US77 provided visual evaluation of the road conditions. Transverse and longitudinal cracks were detected, as shown in Figure 9 and Figure 10.



Figure 9: Images of transverse cracking along US77

The transverse cracks found along US77 would typically extend across an entire lane of the road and repeated in a uniform matter. There was a significant vertical depression at the crack locations and they could be noticed while driving over them. The uniform spacing of the cracks suggests the presence of subsurface joints.



Figure 10: Images of longitudinal cracking along US77

The longitudinal cracks were more commonly found along the outer edge of the right hand lane. These areas included significant settlement of the shoulder, which indicates shear failure. The majority of the longitudinal cracks were found within one mile north of the SH21 intersection.

3.1.4 Previous Site Construction

Limited information is available about the history of US77 construction and maintenance work. The construction of the asphalt concrete mixture (ACM) at the area north of the SH21 intersection took place in 1999. The area south of SH21 underwent

ACM construction in 2001. A seal coat was placed in 2011 on the existing ACM. Minor maintenance efforts have been completed since 2011, including crack sealing and placement of an overlay in small areas where there was significant settlement. It was reported that the old roadway consisted of Portland cement concrete pavement. The joints in the concrete pavement are believed to be the main source for the significant transverse cracks along the roadway.

3.1.5 Pre-Construction Evaluation

Prior to the new overlay construction, TxDOT conducted field tests along US77. These tests included ground penetrating radar (GPR) scans and falling weight deflectometer (FWD) tests. Traffic counts were also taken in each direction during a 24-hour period.

3.1.5.1 GPR

The ground penetrating radar (GPR) provides information on the subsurface conditions of pavement structures. It sends discreet pulses of radar energy into a pavement system and captures reflections from each layer interface within the structure. It can send up to 50 pulses per second and be conducted at speeds up to 70mph. It is a simple way to determine layer thicknesses, changes in pavement structure, and identify subsurface defects.

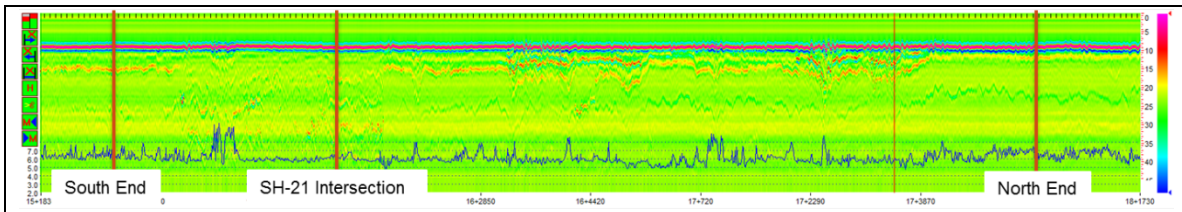


Figure 11: GPR scan of US77 before overlay construction

Figure 11 shows the scan performed before the 2016 overlay construction. At the left end of the image is the southern end of the proposed overlay. The intersection of SH21 and US77 is also shown near the south end point. The north end point of the overlay is marked on the right hand side. An important observation from this image is the variability in subsurface conditions between the 16+2850 and 17+3870 station markers. Specifically, this section shows significant changes in the pavement structure as well as the subgrade.

3.1.5.2 FWD

The falling weight deflectometer (FWD) is a trailer mounted device that delivers a transient force impulse to the pavement surface. The impulse load can range from 2,500 to 27,000 lbs. It typically has a number of deflection sensors spaced 12 inches apart, which measure surface deflections. The FWD is most commonly used for back calculating pavement layer moduli and thicknesses.

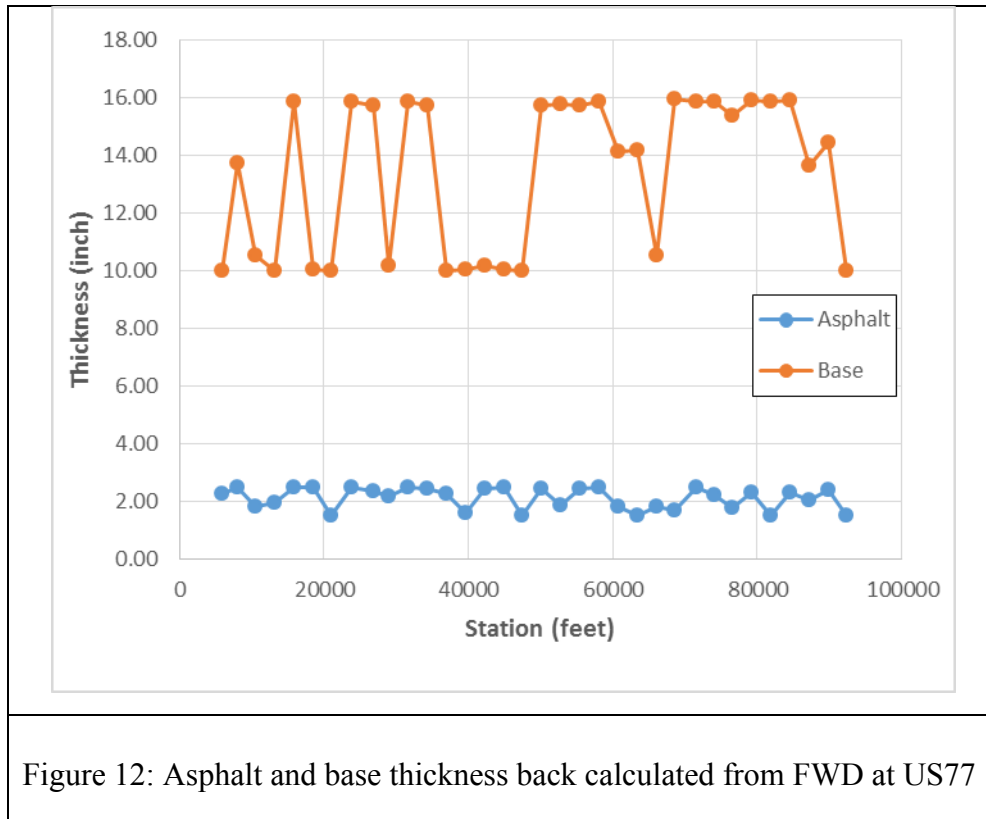


Figure 12: Asphalt and base thickness back calculated from FWD at US77

Figure 12 shows the asphalt and base thicknesses that were back calculated from the FWD testing along US77. The asphaltic layer shows a reasonably consistent thickness of 2 inches. The base thickness ranges from 10 to 16 inches. Due to the inherent error associated with the back calculation, these results were only used for additional confirmation of pavement layer characteristics.

3.1.5.3 Traffic Counts

Traffic counts were taken along US77 north of the SH21 intersection before the construction took place. The counts were performed in each direction for a 24-hour period. The information is presented in hourly intervals and broken down by axle configuration.

a)										b)									
Location ID	144C1_NB	Located On	US0077	Community	-	Location ID	144C1_SB	Located On	US0077	Community	-								
Counted By	TCDS_Combined	Between		County	Lee	Counted By	TCDS_Combined	Between		County	Lee								
Start Date	7/11/2016	And		Module		Start Date	7/11/2016	And		Module									
Start Time	12:30:00 PM	Direction	NB	Agency	Texas DOT	Start Time	12:30:00 PM	Direction	SB	Agency	Texas DOT								
		Source	Syst_Combine	Owner ID	daniel.fox-baker			Source	Syst_Combine	Owner ID	daniel.fox-baker								
FHWA-Scheme F Classification																			
Start Time	Motor cycle	Car	Light Truck	Bus	2A SU	3A SU	>3A SU	<SA 2U	SA 2U	>SA 2U	<6A >2U	6A >2U	>6A >2U	14	15	Total			
12:00 AM	5	2	7	2	2	2	0	4	8	1	1	0	0	0	0	34			
1:00 AM	3	3	13	2	4	3	0	1	1	1	0	0	0	0	1	32			
2:00 AM	3	0	5	0	2	1	0	4	3	1	0	0	2	0	0	21			
3:00 AM	2	1	5	0	1	1	0	2	9	1	3	0	4	0	0	29			
4:00 AM	2	0	2	0	1	2	0	1	7	9	4	0	2	0	0	24			
5:00 AM	2	5	10	0	0	1	0	3	9	4	2	0	2	0	0	38			
6:00 AM	3	7	28	1	5	3	0	7	6	3	6	0	1	0	0	70			
7:00 AM	9	24	68	2	13	12	1	14	2	6	6	0	6	0	1	164			
8:00 AM	5	24	73	2	6	6	0	9	9	6	2	0	2	0	0	144			
9:00 AM	8	47	93	4	7	12	1	15	13	11	6	0	12	0	0	229			
10:00 AM	9	31	79	0	11	8	0	27	9	8	4	0	10	0	0	196			
11:00 AM	4	70	112	4	15	11	3	18	17	21	13	0	4	0	0	292			
12:00 PM	12	57	125	0	8	16	0	24	9	7	7	1	4	0	1	272			
1:00 PM	12	73	92	0	16	12	2	21	11	10	7	0	10	0	1	267			
2:00 PM	14	74	125	1	13	10	2	46	5	15	8	0	4	0	1	318			
3:00 PM	14	50	87	0	9	14	2	29	9	15	10	0	9	0	0	248			
4:00 PM	14	71	114	0	8	12	0	37	8	13	6	0	5	0	0	288			
5:00 PM	18	82	158	1	16	25	4	51	12	16	1	0	14	0	3	401			
6:00 PM	8	50	99	0	10	13	0	20	10	8	5	0	6	0	0	230			
7:00 PM	12	47	55	0	3	5	0	26	10	7	2	0	6	0	0	123			
8:00 PM	8	20	37	0	3	2	0	17	9	1	2	0	8	0	0	107			
9:00 PM	5	24	38	4	7	0	0	10	4	1	2	0	1	0	0	96			
10:00 PM	3	18	22	1	2	1	0	6	7	9	1	0	1	0	2	73			
11:00 PM	1	9	9	0	2	2	0	3	2	4	0	0	2	0	0	30			
TOTAL	177	789	1456	24	165	174	1	394	185	168	99	1	114	0	11	3776			

Location ID	144C1_NB	Located On	US0077	Community	-	Location ID	144C1_SB	Located On	US0077	Community	-					
Counted By	TCDS_Combined	Between		County	Lee	Counted By	TCDS_Combined	Between		County	Lee					
Start Date	7/11/2016	And		Module		Start Date	7/11/2016	And		Module						
Start Time	12:30:00 PM	Direction	NB	Agency	Texas DOT	Start Time	12:30:00 PM	Direction	SB	Agency	Texas DOT					
		Source	Syst_Combine	Owner ID	daniel.fox-baker			Source	Syst_Combine	Owner ID	daniel.fox-baker					
FHWA-Scheme F Classification																
Start Time	Motor cycle	Car	Light Truck	Bus	2A SU	3A SU	>3A SU	<SA 2U	SA 2U	>SA 2U	<6A >2U	6A >2U	>6A >2U	14	15	Total
12:00 AM	4	3	3	3	1	0	0	0	3	0	1	1	2	0	0	21
1:00 AM	3	3	12	2	4	3	0	3	5	2	2	0	0	0	0	39
2:00 AM	1	3	6	0	0	1	0	5	7	1	0	0	2	0	0	26
3:00 AM	3	3	4	0	2	2	0	0	6	0	1	0	0	0	0	21
4:00 AM	0	6	16	0	1	0	0	2	5	0	0	1	1	0	0	32
5:00 AM	2	35	29	0	5	1	0	5	9	5	2	0	2	0	0	95
6:00 AM	7	58	56	0	5	12	0	13	3	9	4	0	6	0	0	173
7:00 AM	14	122	107	0	7	13	0	33	13	8	7	0	13	0	3	340
8:00 AM	15	65	61	1	1	14	0	24	20	9	4	0	12	0	2	228
9:00 AM	14	76	74	1	6	20	2	25	24	22	13	0	17	0	0	294
10:00 AM	7	52	87	0	1	12	0	20	16	15	5	0	4	0	1	210
11:00 AM	4	40	73	1	14	3	1	30	13	2	3	0	2	0	0	175
12:00 PM	8	60	70	0	2	13	2	25	11	6	1	0	4	0	3	205
1:00 PM	8	68	77	5	7	16	3	22	7	8	4	0	3	0	0	228
2:00 PM	6	80	90	0	9	14	0	24	9	9	8	0	7	0	0	256
3:00 PM	6	74	70	0	3	10	0	12	9	11	2	0	6	0	0	203
4:00 PM	6	77	60	0	3	16	3	24	14	9	4	1	8	0	2	227
5:00 PM	8	74	95	0	4	16	0	9	15	7	5	0	9	0	0	210
6:00 PM	5	65	72	0	2	10	1	20	15	13	4	1	6	0	1	215
7:00 PM	5	32	47	0	2	6	0	9	11	4	3	1	6	0	1	127
8:00 PM	2	38	27	1	1	4	0	6	12	2	0	2	4	0	0	99
9:00 PM	2	19	18	0	1	3	0	5	18	4	3	0	4	0	1	78
10:00 PM	3	18	15	1	0	3	0	7	8	6	5	0	3	0	0	69
11:00 PM	3	7	9	1	0	1	0	4	2	2	2	0	2	0	0	48
TOTAL	136	1087	1178	16	81	199	13	297	265	155	89	7	126	0	15	3651

Figure 13: US77 traffic counts: a) northbound; b) southbound

Figure 13 shows the traffic counts in each direction along US77. The northbound direction shows the highest volume of vehicles between the hours of 7am and 7pm during which 3,222 vehicles were counted. The total count for the day was 3,776 vehicles. The southbound traffic showed the highest volume during the hours of 6am to 6pm, totaling 2,996 vehicles. The total number of southbound vehicles for the day was 3,651. Furthermore, the multi-unit vehicles counted in a day is 976 in the northbound direction and 948 in the southbound direction.

3.2 FIELD TESTING DESIGN

3.2.1 Materials

The geogrid products used in this study are manufactured by Huesker Inc. and commercialized under the name of HaTelit. HaTelit products are designed to be flexible, high-strength, and temperature resistant grids to increase the effective reinforcement of asphalt layers. They offer good resistance to installation damage when driven over by asphalt trucks and pavers, as well as during compaction. They can be installed on milled surfaces and are resistant to degradation in alkaline environments. The bitumen coating and interlocking capabilities of the grid allow for strong bonding between reinforcement and asphalt layers

Two different types of interlayer geosynthetics were used in the US77 test sections. One of the geosynthetics, HaTelit C 40/17, is comprised of a reinforcement grid made from high-modulus polyester yarns (PET) with a lightweight nonwoven geotextile backing. The second geosynthetic was HaTelit XP, which is comprised of a reinforcement grid made from polyvinyl alcohol (PVA) with a lightweight non-woven geotextile backing. The product specifications are shown in Table 2.

Table 2: Physical properties of HaTelit products

Test name	Test standard	HaTelit C40/17	HaTelit XP50
Mass/Unit Area	ASTM D-5261	270 g/m ²	210 g/m ²
Aperture Size	Measured	40 x 40 mm	40 x 40 mm
Open Area of Grid	CWO 22125	>80 %	>80 %
Wide Width Tensile Strength Machine Direction (MD)	ASTM D-6637	50 kN/m	>50 kN/m
Cross-Machine Direction (CMD)	ASTM D-6637	50 kN/m	>50 kN/m
Tensile Strength @ 3% Strain	ASTM D-6637	12 kN/m	>22 kN/m
Elongation at Break	ASTM D-6637	<10 %	<6%
Shrinkage @ 375° F for 15 min		<1%	
Melting Point	ASTM D-276	255° C	

3.2.2 Test Section Location

Test sections were constructed at the northernmost end of the overlay construction, approximately two miles north of the intersection between US77 and SH21. The test section location was chosen based on a number of factors, including the uniform thickness of different layers as observed from GPR results based on a scan completed before the overlay construction. This is shown in Figure 14 and Figure 15.

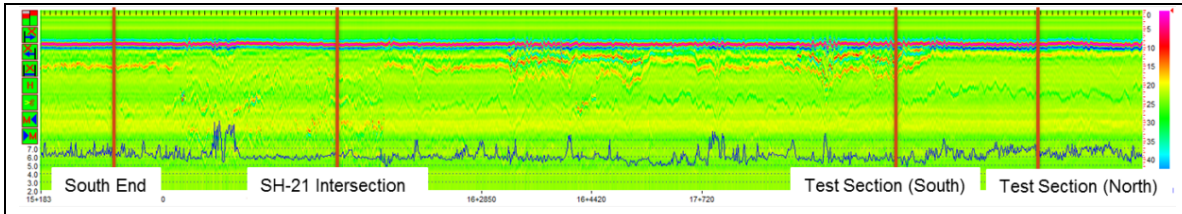


Figure 14: GPR scan on US77 before overlay construction

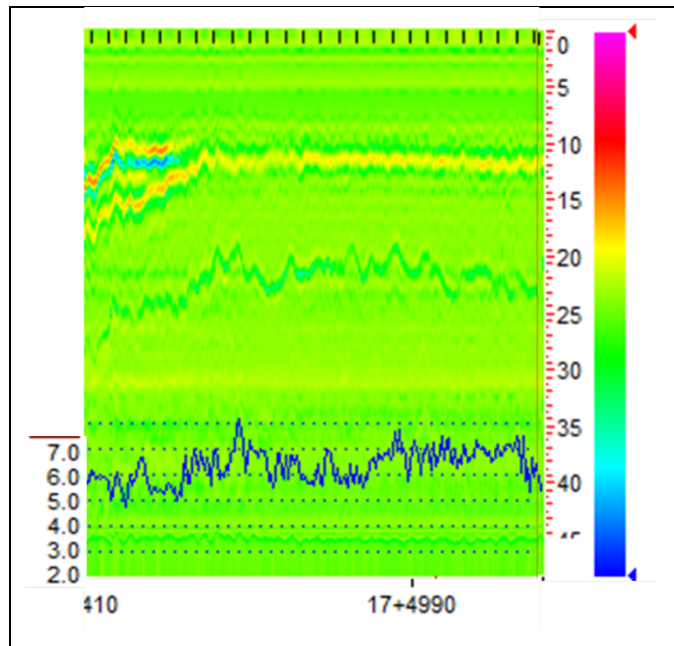


Figure 15: GPR scan of chosen test section location

Figure 14 shows the entire scan of the US77 overlay. Relevant locations are marked on the image indicating the beginning and end of the test sections as well as the overlay. Figure 15 shows the same scan zoomed in to the proposed area for the test sections. This location was chosen based on the uniformity of the pavement, base, and subgrade layer thicknesses.

The second reason for the selected location of the test sections was to minimize acceleration/deceleration. It was determined that the areas with relatively small elevation changes and curvature would be beneficial. The elevation profile and overhead view of the site were used for this matter.



Figure 16: Elevation profile for US77



Figure 17: Overhead view of US77 overlay

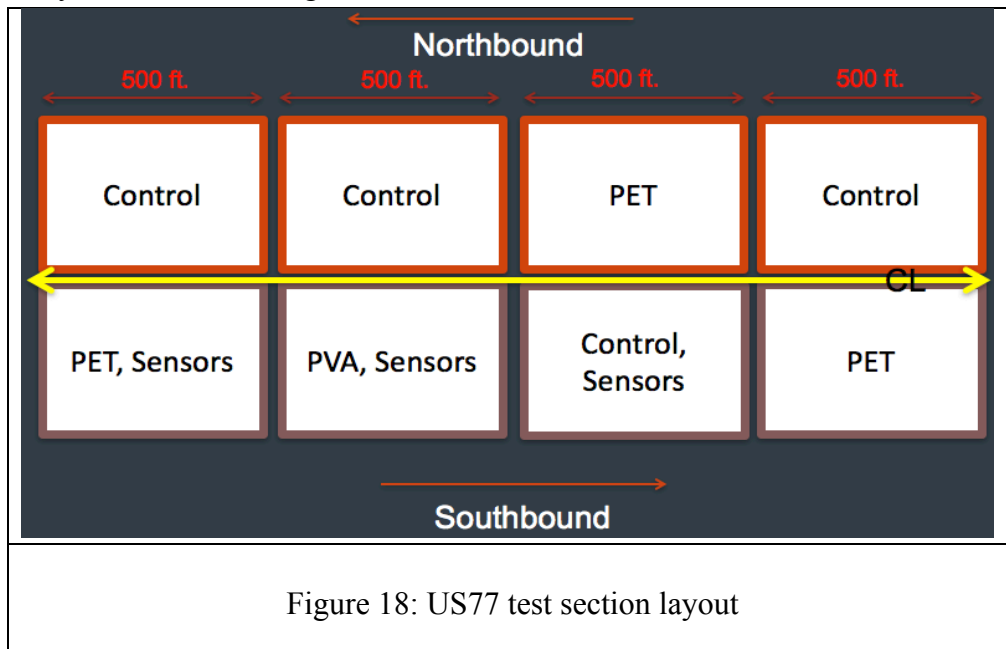
Figure 16 shows the elevation profile for the length of the proposed overlay. The far left end of the image is the north endpoint of the overlay and the far right end is the south endpoint. The smallest elevation change over the necessary length for the test sections was identified at the north end of the overlay. Figure 17 shows comparatively small curvature at the proposed test section location.

Lastly, the pavement condition was evaluated to find the best area for test section installation. It was decided that an area with preexisting cracks would be best, since one

of the main objectives for placing interlayer reinforcements is to retard reflective cracking. Condition surveys revealed a significant number of transverse cracking at the northern end of the project.

3.2.3 Test Section Sequence

When travelling southbound from the north end of the overlay, the sequence of test sections includes PET reinforcement, PVA reinforcement, control section, and a repeat PET reinforcement. The sections were named Section 1, Section 2, Section 3, and Section 4. The order of the reinforcements was determined based on ease of installation. A repeat section of the PET grid was installed because this interlayer reinforcement was deemed as a cost-effective product. On the other side of the road in the northbound direction, reinforcement was only installed parallel to the control section. This was done so a side by side comparison of reinforced versus unreinforced could be performed while minimizing changes in the subgrade. The order of the northbound sections is control, PET reinforcement, control, control, ending at the north end of the overlay. The test section layout is shown in Figure 18.



3.2.4 Sensor Locations

Asphalt strain gages (ASGs) were installed in the right hand lane of Section 1, Section 2, and Section 3. The original installation plan included placing sensors in

Section 4 but time constraints during installation did not allow for it. In each section, four strain gages were installed in the right hand wheel path, and two strain gages between the wheel paths. Within the wheel path, one sensor was installed in the longitudinal direction on a pre-existing crack, two of the sensors were installed in the longitudinal direction away from a crack, and the last sensor was installed in the transverse direction away from a crack. Between the wheel paths, one sensor was installed in the longitudinal direction on a pre-existing crack, and the other sensor was installed in the transverse direction away from a crack. The orientation of the strain gage was determined to assess the difference in strains in the longitudinal and transverse directions. Sensors were placed on cracks to assess the effect of reinforcement regarding mitigation of reflective cracks. The sensor configuration for each section is shown in Figure 19.

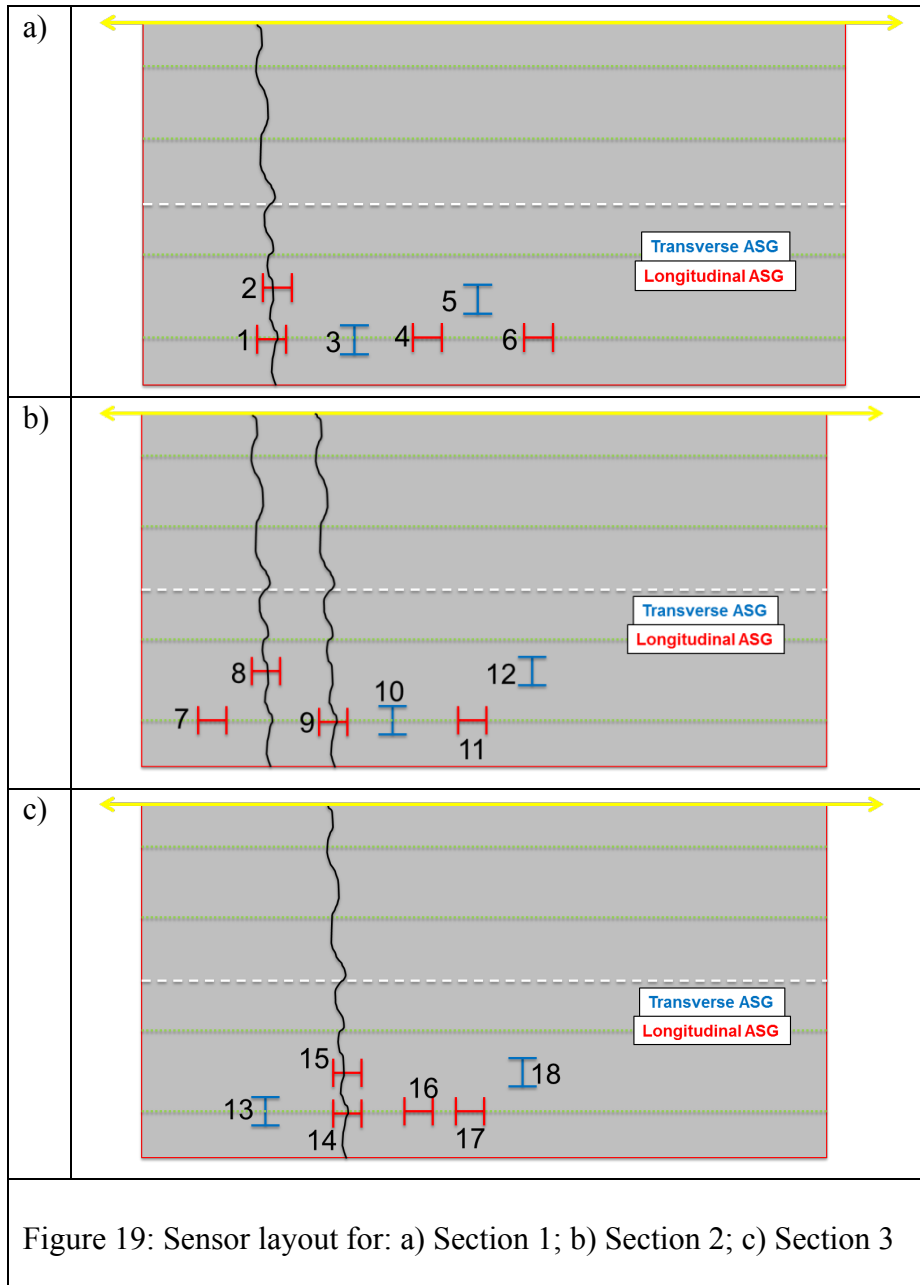
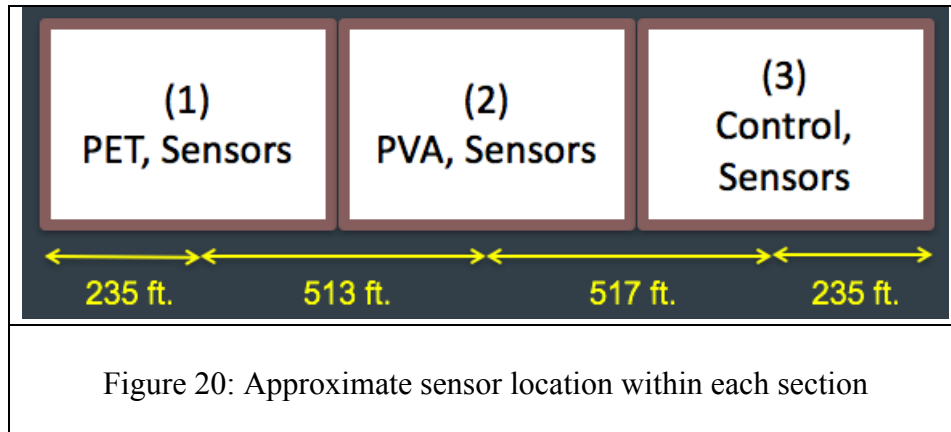


Figure 19 shows the individual sensor layout for each of the instrumented sections. The sensor number is shown next to the relative location. As mentioned, six strain gages were installed in each section. The sensor location within each section was chosen based on the presence of a transverse crack near the middle of the 500 ft. length. Figure 20 shows the approximate location where the sensor wires extended to the edge of the pavement and were connected to the data logger.



3.3 INSTALLATION OF GEOSYNTHETIC REINFORCEMENTS

3.3.1 Overlay Construction

The contractor in charge of the US77 overlay construction is a company called Knife River. The pre-construction meeting took place on August 5, 2016. From August 8 to August 12, full depth repair and level up was performed on certain areas of the road. On August 19, an extra area of level up was performed at a location north of the overlay itself. The overlay construction began August 23 on the inside lane of the northbound direction. The plan was to overlay one lane each day to minimize lane closures. The inside lane of the southbound direction was finished on August 24, followed by the outside lane of the northbound direction on August 25, then the outside lane of the southbound direction on August 26. The overlay was finalized on August 27 by adding the lane striping and reflectors. The overlay itself consisted of a chip seal placed on asphalt cement (AC20 & TY PD GR 4 AGGR & ACP TY “D”) with a 1.5 inch type “D” asphalt overlay. Rolling compactors were then used to meet the thickness and density requirements.

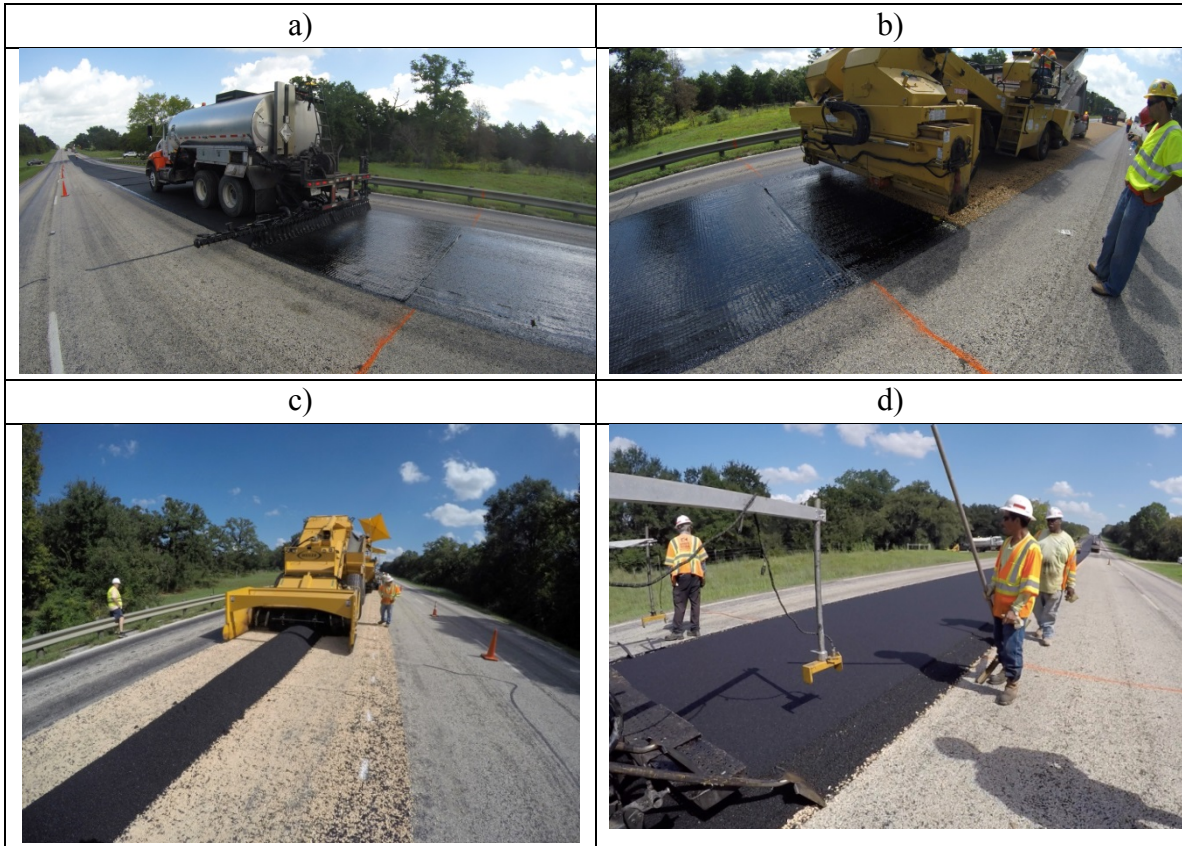


Figure 21: US77 overlay construction during: a) tack coat application for chip seal; b) aggregate placement for chip seal; c) asphalt placement; d) asphalt leveling

Figure 21 shows the construction sequence for the pavement installation. The first step after reinforcement placement was to apply the tack coat used for the chip seal. Then, a truck containing the aggregate fed the chip spreader, which dropped the aggregate on the fresh tack coat. Placement of the HMA was conducted next. A truck containing the HMA unloaded through an opening in the bottom of the trailer. The paving finisher then collected the HMA with an auger and spread it across the width of the lane. The last step was to compact the asphalt to the desired density and thickness. This was done by vibratory rolling compactors that followed the paver. It took a number of passes to reach proper compaction specifications.

3.3.2 Reinforcement Installation

The installation of the geosynthetics was completed first thing each morning before placing the chip seal and pavement. The order of installation was the same as the overlay construction. It started with the northbound inside lane with one roll of the PET geogrid. Day 2 was the southbound inside lane and one roll of the PET geogrid was installed in Section 1, then the PVA geogrid in Section 2, no grid in Section 3, and a repeated PET geogrid in Section 4. Day 3 was northbound outside lane and one roll of the PET geogrid was installed next to Section 3. Day 4 involved southbound outside lane after the sensors had been installed. One roll of the PET geogrid was installed in Section 1, then the PVA geogrid in Section 2, no grid in Section 3, and a repeated PET geogrid in Section 4.



Figure 22: Interlayer installation sequence: a) looping tow strap through tack truck bumper and evening the strap; b) tack application and initial installment; c) continued installment and monitoring

Figure 22 shows the main aspects of the geosynthetic installation sequence. The first step in the installation was to clean the road surface with large rolling sweepers and cut away any vegetation off the shoulders. The geosynthetic rolls were then placed at the beginning of previously marked sections. The tack truck sprayed a small amount of tack coat to adhere to the end of the roll as shown in Figure 22 a. A steel rod was fed through

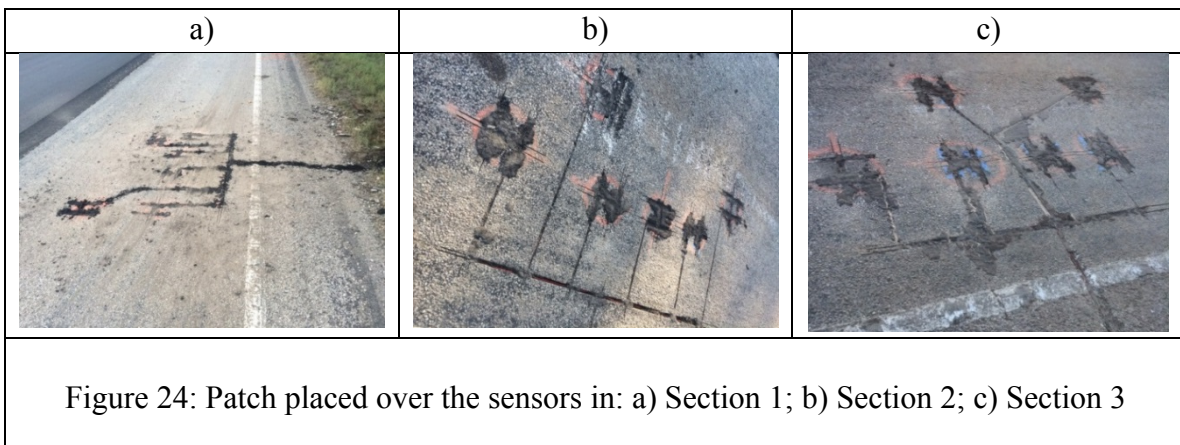
the center of each roll. A tow strap was looped through the rear bumper of the tack truck then attached to each end of the rod. Once the strap was even, the tack truck began spraying the tack coat while pulling the roll as shown in Figure 22 b. The geosynthetic was then unrolled on to the fresh tack coat. Figure 22 c. shows the tack truck unrolling the geosynthetic as it nears the end of the section. This method of fabric installation proved beneficial in that the roll was placed on fresh tack coat in a straight line, and was always in tension so no creases formed. The chip seal was placed after the geosynthetic installation, followed by the HMA placement.

3.3.3 Sensor Installation

Asphalt strain gages are typically installed in new roads above the base material and then paved over. In this project, however, the sensors were installed into the pre-existing pavement so they would sit below the overlay and reinforcement layer. Each sensor is 0.75 inches in height so it was necessary to place them 1.25 inches in to the existing pavement so they would be 2.0 inches below the surface of the 1.5 inch overlay. Sensor installation took place on the night of August 25 after having constructed the outside northbound overlay but before construction of the outside southbound overlay.



The first step was to mark the locations of each individual sensor with a prefabricated stencil in the shape of the asphalt strain gages. This is shown in Figure 23 a. A circular saw with a concrete saw blade was then used to cut in to the asphalt to a depth of 1.25 inches. A network of channels was then cut to be able to feed the wires to the edge of the pavement. This is shown by Figure 23 b. The cuts were then excavated using a crow bar and the sensors were placed in the holes. This is shown by Figure 23 c. A mixture of asphalt cement and sand was placed over each sensor and compacted to be flush with the pre-existing pavement surface. Figure 24 shows each section after the sensors were installed and the patch was placed.

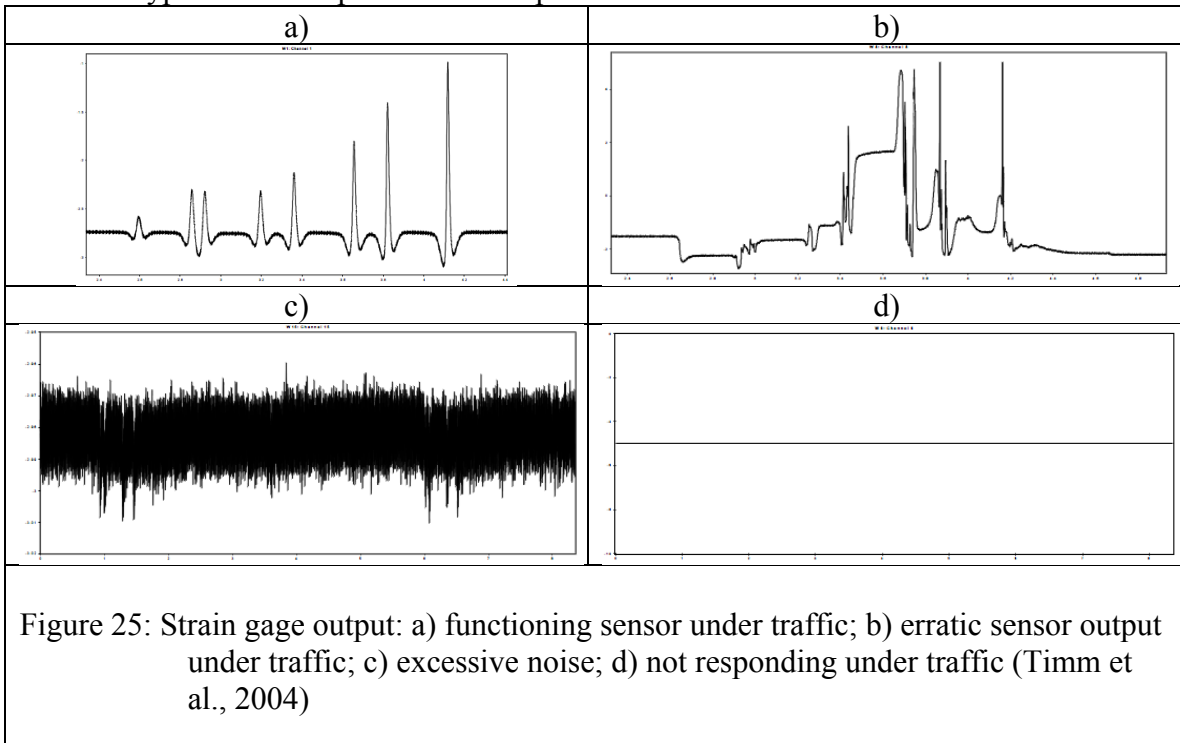


3.4 COLLECTION OF FIELD DATA

3.4.1 Strain Measurements Using Asphalt Strain Gages

Asphalt strain gages (ASG), produced by CTL Group, were used in this investigation. These strain gages are designed with durable materials to withstand high temperatures and compaction loads associated with asphalt pavement construction. They are designed with a full-bridge configuration to eliminate the need for expensive data acquisition hardware. The lead wire is protected by a braided Teflon polymer coating shielding and is meant to be resistant to abrasion and temperatures up to 205° C (CTL Group, 2017). These strain gages have been used in a number of studies involving strain measurements of asphalt layers (e.g. Correia, 2014). Installation of these sensors is

typically within a new pavement. The strain gages should have a minimum of two inches of material between the sensor and the pavement surface. It is recommended to place the strain gage on a flat surface in a patch of heated tack coat. This creates a bond so the gage does not move during the construction process. Once the gage is placed, a bitumen and sand mix should cover the gage. This allows for the placement and compaction of the HMA. Survivability of the gages can vary depending on the pre-construction placement and present construction operations (Timm et al., 2004). Typical sensor outputs are shown in Figure 25. Figure 25 a. shows a functioning sensor and the other plots show different types of sensor problematic responses.



Data reduction of strain measurements from ASG-152s can be accomplished in a number of ways. Due to the behavior of asphalt under traffic conditions, there is commonly a transition from a compressed state to a tensile state. To account for this, differential voltages due to tensile loads are determined by subtracting the minimum voltage value from the maximum voltage value, as illustrated in Figure 26. This is to account for the amount of tension required to overcome the compression and is considered the total tensile strain imparted by a particular axle load (Scholz, 2010)

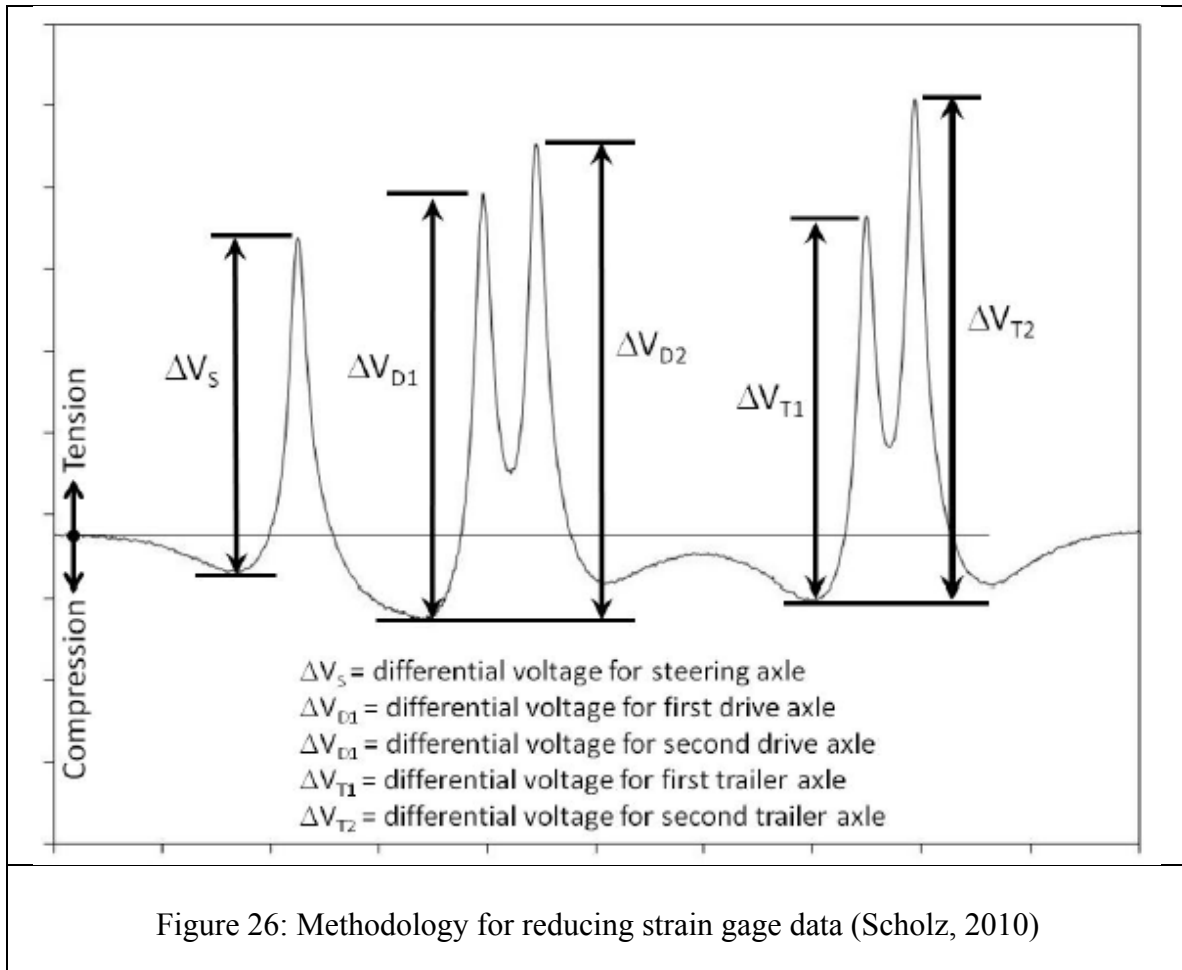



Figure 26: Methodology for reducing strain gage data (Scholz, 2010)

A study on the repeatability of asphalt strain gage measurements was conducted, which led to the following conclusions:

- Individual gage repeatability was not strongly influenced by the average strain magnitude. There was a slight decrease in the percent difference with an increased strain magnitude indicating relatively stable precision.
- FWD analysis data indicated a strain of $12\mu\epsilon$ could be used as a threshold for evaluating reliability of singular gage repetitions.
- Longitudinal gages had slightly more consistent readings than transverse gages.
- Steering axles caused lower measured absolute difference than tandem and single axles.
- Cracked sections showed more erratic strain measurements (Willis et al., 2009).

3.4.2 Asphalt Strain Gages

The strain gages used for this project were purchased from CTL Group. The model number of the sensors is ASG-152. They are asphalt strain gages designed to withstand high temperatures and compaction loads associated with pavement construction. These sensors are used to measure horizontal strains in asphalt layers. The sensors have a full bridge so no completion is required. The excitation voltage can be up to 10V and the output is about 2mV/V at 1500µε. Each sensor has a 30ft lead wire that is used to reach a central location at the edge of the pavement. The sensors are in the shape of a ‘H’ with the 5.5” middle section containing the actual sensor fitted with two 4” flanges. Figure 27 shows an image of the ASG-152 and the specifications provided by the manufacturer.

a)	b)
	<p>General Specifications</p> <p>Bridge Completion Full bridge, no completion required</p> <p>Gage Resistance 350 Ohm</p> <p>Excitation up to 10 Volts</p> <p>Output ≈ 2 mV/V @ 1500 µstrain</p> <p>Calibration Factor Individually provided</p> <p>Grid Area 0.133cm²</p> <p>Gage Area 1.22 cm² overall</p> <p>Fatigue Life <10⁵ repetitions @ +/- 1500 µstrain</p> <p>Modulus ≈ 2 340,000 psi</p> <p>Cell Material Black 6/6 nylon</p> <p>Coating Two-part polysulfide liquid polymer, encapsulate in silicone with butyl rubber outer core</p>
<p>Figure 27: ASG 152: a) image; b) specifications</p>	

3.4.2 Data Logger

3.4.2.1 DATAQ data logger

One of the data acquisition systems used for strain measurements in this study was manufactured by DATAQ Instruments. The model of the data logger is DI-718B-US. This is a stand-alone data logger with 8 channels. It has the capability of measuring temperature, pressure, flow, current, voltage, and more using specific amplifiers. Data is

stored to a SD memory card and can be downloaded via their software, WinDAQ. For measuring strains from the ASG-152 sensors, strain gage amplifiers were installed into each data logger. The amplifier used in this study was also manufactured by DATAQ Instruments. The model number for the amplifiers is DI-8B38-05. These amplifiers have an input range of $\pm 20\text{mV}$ with a $+10\text{V}$ excitation. The sensitivity is 2mV/V and they have an output range of $\pm 5\text{V}$. A combination of generators and rechargeable lithium batteries were used to provide the required 12V power.

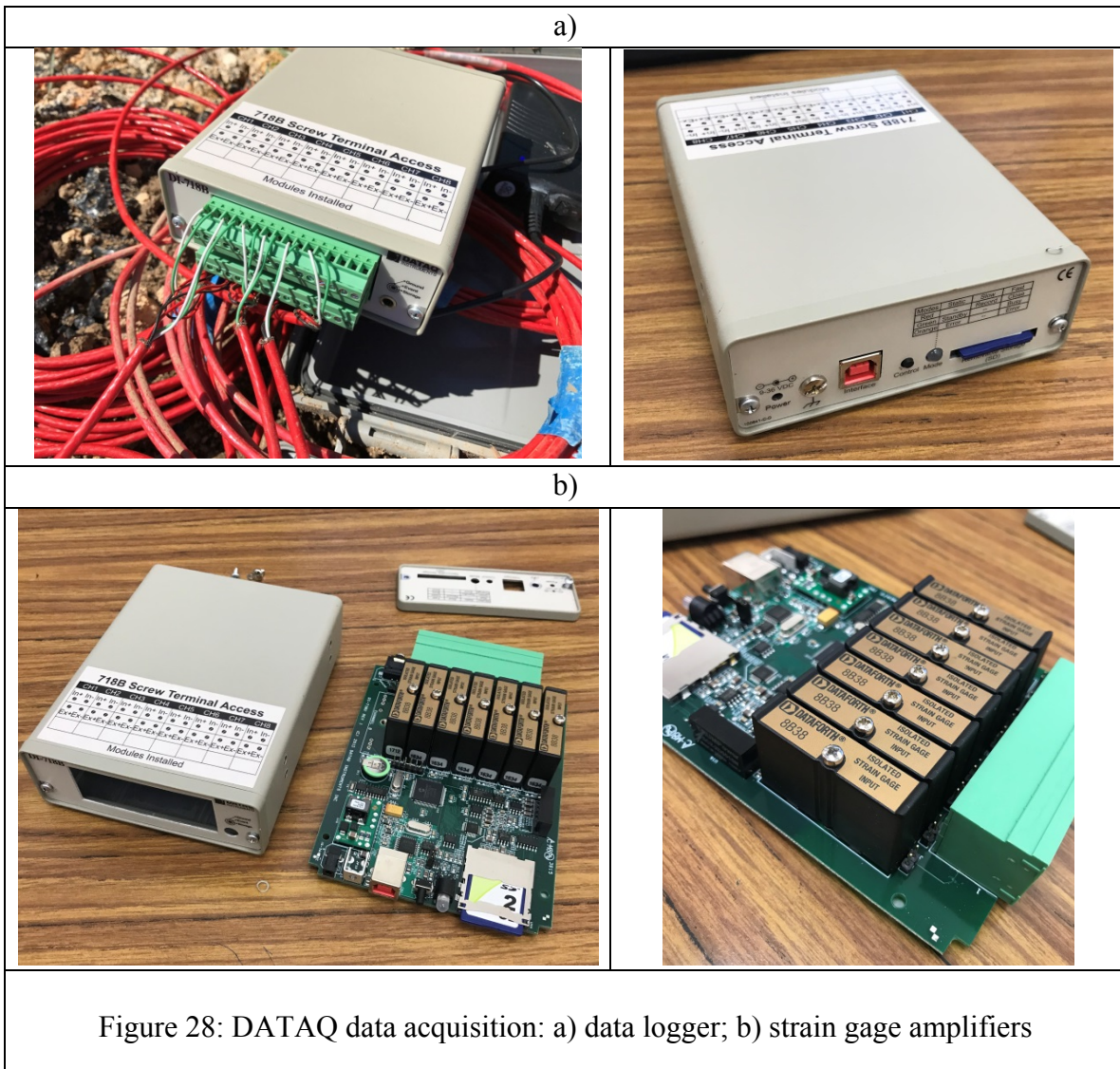


Figure 28 shows the DATAQ data logger and installed strain gage amplifiers. Figure 28 a. shows the stand-alone data logger. The green terminal remains wired to the strain gages at all times. The terminal is simply plugged into the designated data logger

and powered on to collect data. The amplifiers shown in Figure 28 b. are installed to the motherboard of the data logger. Specification for the data logger and the amplifiers are shown in Figure 29.

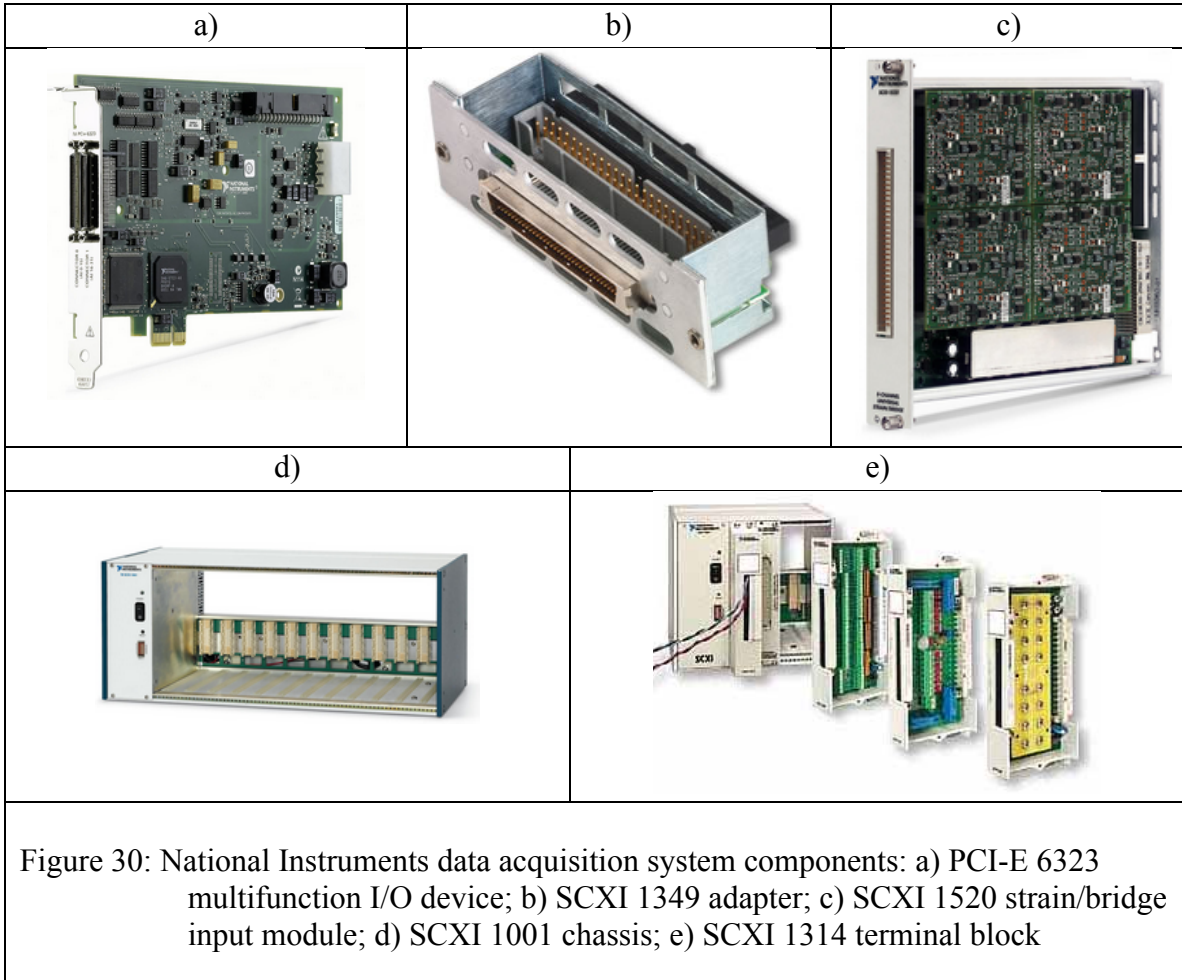
a)	b)																																																																																																																												
<table border="1"> <thead> <tr> <th colspan="2" style="text-align: center;">DI-718B Specifications</th> </tr> </thead> <tbody> <tr> <td>Analog Inputs</td> <td> Number of Channels: 8 configured for signal conditioned inputs Channel Configuration: Defined by DI-8B Module Measurement Range: Defined by DI-8B Module Accuracy: ±0.25% FSR (at 1800 S/s, averaging mode) Resolution: ±1 part in 8,192 Input Impedance: Defined by DI-8B Module Input offset voltage: Defined by DI-8B Module Channel-to-channel crosstalk rejection: -75db @ 100Q unbalance Offset temperature coefficient: 0.25µV/°C Digital filtering: Standard: Conditional over-sampling Stand-alone: None CJC Error: 1.5°C plus 8B Module </td> </tr> <tr> <td>Isolation (via DI-8B Modules)</td> <td> Input-to-Output: 1000VDC/Peak AC Channel-to-Channel: 500VDC/Peak AC </td> </tr> <tr> <td>A/D Characteristics</td> <td> Type: Successive approximation Resolution: 14-bit Monotonicity: ±2 LSB Conversion Time: 69.4µs </td> </tr> <tr> <td>Scanning Characteristics</td> <td> Max. throughput sample rate: Standard: 4,800 Hz Stand-alone: 14,400 Hz* Min. throughput sample rate: Standard: 0.0034 Hz Stand-alone: 0.0017 Hz Max. scan list size: 9 entries Sample buffer size: 2kb </td> </tr> <tr> <td>Calibration</td> <td> Calibration cycle: One year Calibration method: Calibration Software, provided. *Dependent on SD card used. Low speed SD cards can sample up to 2,000 Hz. High speed cards can sample up to 14,400 Hz. Some high speed cards cannot sample as high as 14,400 Hz but their capability can only be determined by trial and error (Model 101014-2G has been tested and approved). </td> </tr> <tr> <td>Controls (Stand-alone models)</td> <td> Single push-button: Provides manual control over Record and Standby </td> </tr> <tr> <td>Digital I/O</td> <td> Bits: 2 Inputs (Remote Storage and Remote Events) Input voltage levels: Min. required "1" 2V; Max allowed "0" 0.8V </td> </tr> <tr> <td>Ethernet Interface</td> <td> Type: 10/100Base-T Connector: RJ-45 Protocol: TCP/IP Server Type: DHCP or Fixed IP </td> </tr> <tr> <td>Removable Memory (Stand-alone models)</td> <td> Type: Standard SD (not SDHD or SDxC) Capacity: 16MB to 2GB </td> </tr> <tr> <td>Real Time Clock (Stand-alone models)</td> <td> Type: Date, hour, minute, second Resolution: 1 second Accuracy: 20 ppm </td> </tr> <tr> <td>Transfer Rate to PC</td> <td> Real Time: up to 4,800 samples per second From Memory Card: up to 3,000 samples per second </td> </tr> <tr> <td>General</td> <td> Panel indicators: Mode LED Panel Controls: Control push button (Stand-alone models) Panel Slots: Accepts MMC/SD-type flash memory Input connectors: Two, removable sixteen position terminal blocks Operating Environment: 0°C to 70°C Enclosure: Aluminum base with steel wrap-around. Dimensions: 5 7/8" D × 4 1/8" W × 1 1/2" H (13.81D × 10.48W × 3.81H cm) Weight: 14 oz. Power Requirements: USB: 9 to 36 VDC, 2 watts + 8B modules Ethernet: 9 to 36 VDC, 2.5 watts + 8B modules </td> </tr> <tr> <td>Indicators</td> <td> Stand-alone models: Three-color LED indicating Record, Standby, and Error conditions Standard models: Power LED </td> </tr> </tbody> </table>	DI-718B Specifications		Analog Inputs	Number of Channels: 8 configured for signal conditioned inputs Channel Configuration: Defined by DI-8B Module Measurement Range: Defined by DI-8B Module Accuracy: ±0.25% FSR (at 1800 S/s, averaging mode) Resolution: ±1 part in 8,192 Input Impedance: Defined by DI-8B Module Input offset voltage: Defined by DI-8B Module Channel-to-channel crosstalk rejection: -75db @ 100Q unbalance Offset temperature coefficient: 0.25µV/°C Digital filtering: Standard: Conditional over-sampling Stand-alone: None CJC Error: 1.5°C plus 8B Module	Isolation (via DI-8B Modules)	Input-to-Output: 1000VDC/Peak AC Channel-to-Channel: 500VDC/Peak AC	A/D Characteristics	Type: Successive approximation Resolution: 14-bit Monotonicity: ±2 LSB Conversion Time: 69.4µs	Scanning Characteristics	Max. throughput sample rate: Standard: 4,800 Hz Stand-alone: 14,400 Hz* Min. throughput sample rate: Standard: 0.0034 Hz Stand-alone: 0.0017 Hz Max. scan list size: 9 entries Sample buffer size: 2kb	Calibration	Calibration cycle: One year Calibration method: Calibration Software, provided. *Dependent on SD card used. Low speed SD cards can sample up to 2,000 Hz. High speed cards can sample up to 14,400 Hz. Some high speed cards cannot sample as high as 14,400 Hz but their capability can only be determined by trial and error (Model 101014-2G has been tested and approved).	Controls (Stand-alone models)	Single push-button: Provides manual control over Record and Standby	Digital I/O	Bits: 2 Inputs (Remote Storage and Remote Events) Input voltage levels: Min. required "1" 2V; Max allowed "0" 0.8V	Ethernet Interface	Type: 10/100Base-T Connector: RJ-45 Protocol: TCP/IP Server Type: DHCP or Fixed IP	Removable Memory (Stand-alone models)	Type: Standard SD (not SDHD or SDxC) Capacity: 16MB to 2GB	Real Time Clock (Stand-alone models)	Type: Date, hour, minute, second Resolution: 1 second Accuracy: 20 ppm	Transfer Rate to PC	Real Time: up to 4,800 samples per second From Memory Card: up to 3,000 samples per second	General	Panel indicators: Mode LED Panel Controls: Control push button (Stand-alone models) Panel Slots: Accepts MMC/SD-type flash memory Input connectors: Two, removable sixteen position terminal blocks Operating Environment: 0°C to 70°C Enclosure: Aluminum base with steel wrap-around. Dimensions: 5 7/8" D × 4 1/8" W × 1 1/2" H (13.81D × 10.48W × 3.81H cm) Weight: 14 oz. Power Requirements: USB: 9 to 36 VDC, 2 watts + 8B modules Ethernet: 9 to 36 VDC, 2.5 watts + 8B modules	Indicators	Stand-alone models: Three-color LED indicating Record, Standby, and Error conditions Standard models: Power LED	<table border="1"> <thead> <tr> <th colspan="3" style="text-align: center;">SPECIFICATIONS</th> </tr> <tr> <td colspan="3" style="text-align: center;">Typical at T_A = +25°C and +5V Power</td> </tr> <tr> <td></td> <th style="text-align: center;">DI-8B38-0x</th> <th style="text-align: center;">DI-8B38-3x</th> </tr> </thead> <tbody> <tr> <td>Input Range</td> <td colspan="2" style="text-align: center;">±10mV to ±100mV</td> </tr> <tr> <td>Input Bias Current</td> <td colspan="2" style="text-align: center;">±0.5nA</td> </tr> <tr> <td>Input Resistance</td> <td colspan="2"> Normal: 50MΩ Power Off: 100kΩ Overload: 100kΩ </td> </tr> <tr> <td>Input Protection</td> <td colspan="2"> Continuous: 240VAC Transient: ANSIIEEE C37.90.1 </td> </tr> <tr> <td>Excitation Output (-x1)</td> <td colspan="2" style="text-align: center;">+3.333V ±2mV</td> </tr> <tr> <td>Load Resistance</td> <td colspan="2" style="text-align: center;">100Ω to 2kΩ</td> </tr> <tr> <td>Excitation Output (-2x, -5x)</td> <td colspan="2" style="text-align: center;">+10V ±5mV</td> </tr> <tr> <td>Load Resistance</td> <td colspan="2" style="text-align: center;">300Ω to 2kΩ</td> </tr> <tr> <td>Excitation Load Regulation</td> <td colspan="2" style="text-align: center;">1.5ppm/mA</td> </tr> <tr> <td>Excitation Stability</td> <td colspan="2" style="text-align: center;">50ppm/°C</td> </tr> <tr> <td>Excitation Protection</td> <td colspan="2" style="text-align: center;">120VAC</td> </tr> <tr> <td>CMV Input to Output</td> <td colspan="2" style="text-align: center;">1500Vrms max</td> </tr> <tr> <td>Transient Input to Output</td> <td colspan="2" style="text-align: center;">ANSIIEEE C37.90.1</td> </tr> <tr> <td>CMR (50Hz or 60Hz)</td> <td colspan="2" style="text-align: center;">100dB</td> </tr> <tr> <td>NMR</td> <td colspan="2" style="text-align: center;">100dB per decade above 8kHz</td> </tr> <tr> <td>Accuracy[†]</td> <td colspan="2" style="text-align: center;">±0.05% Span</td> </tr> <tr> <td>Nonlinearity</td> <td colspan="2" style="text-align: center;">±0.02% Span</td> </tr> <tr> <td>Stability</td> <td colspan="2"> Offset: ±25ppm/°C Gain: ±100ppm/°C </td> </tr> <tr> <td>Noise</td> <td colspan="2"> Output, 100kHz: 1500µVrms 200µVrms </td> </tr> <tr> <td>Bandwidth, -3dB</td> <td colspan="2" style="text-align: center;">8kHz</td> </tr> <tr> <td>Response Time, 90% Span</td> <td colspan="2" style="text-align: center;">70µs</td> </tr> <tr> <td>Output Range</td> <td colspan="2" style="text-align: center;">±5V</td> </tr> <tr> <td>Output Protection</td> <td colspan="2"> Continuous Short to Ground: ANSIIEEE C37.90.1 Transient: ±5VDC ±5% </td> </tr> <tr> <td>Power Supply Voltage</td> <td colspan="2" style="text-align: center;">+5VDC ±5%</td> </tr> <tr> <td>Power Supply Current</td> <td colspan="2"> 110mA No Exc. Load 150mA Full Exc. Load </td> </tr> <tr> <td>Power Supply Sensitivity</td> <td colspan="2" style="text-align: center;">±50ppm/%</td> </tr> <tr> <td>Mechanical Dimensions</td> <td colspan="2" style="text-align: center;"> 1.11" × 1.65" × 0.40" (28.1mm × 41.9mm × 10.2mm) </td> </tr> <tr> <td>Environmental</td> <td colspan="2"> Operating Temperature: -40°C to +85°C Storage Temperature: -40°C to +85°C Relative Humidity: 0 to 95% Noncondensing </td> </tr> <tr> <td colspan="3"> [†]240VAC between + and -/+EXC/-EXC terminals. 120VAC between - and +EXC/-EXC terminals and between +EXC and -EXC terminals. *Includes nonlinearity, hysteresis, and repeatability. </td> </tr> </tbody> </table>	SPECIFICATIONS			Typical at T _A = +25°C and +5V Power				DI-8B38-0x	DI-8B38-3x	Input Range	±10mV to ±100mV		Input Bias Current	±0.5nA		Input Resistance	Normal: 50MΩ Power Off: 100kΩ Overload: 100kΩ		Input Protection	Continuous: 240VAC Transient: ANSIIEEE C37.90.1		Excitation Output (-x1)	+3.333V ±2mV		Load Resistance	100Ω to 2kΩ		Excitation Output (-2x, -5x)	+10V ±5mV		Load Resistance	300Ω to 2kΩ		Excitation Load Regulation	1.5ppm/mA		Excitation Stability	50ppm/°C		Excitation Protection	120VAC		CMV Input to Output	1500Vrms max		Transient Input to Output	ANSIIEEE C37.90.1		CMR (50Hz or 60Hz)	100dB		NMR	100dB per decade above 8kHz		Accuracy[†]	±0.05% Span		Nonlinearity	±0.02% Span		Stability	Offset: ±25ppm/°C Gain: ±100ppm/°C		Noise	Output, 100kHz: 1500µVrms 200µVrms		Bandwidth, -3dB	8kHz		Response Time, 90% Span	70µs		Output Range	±5V		Output Protection	Continuous Short to Ground: ANSIIEEE C37.90.1 Transient: ±5VDC ±5%		Power Supply Voltage	+5VDC ±5%		Power Supply Current	110mA No Exc. Load 150mA Full Exc. Load		Power Supply Sensitivity	±50ppm/%		Mechanical Dimensions	1.11" × 1.65" × 0.40" (28.1mm × 41.9mm × 10.2mm)		Environmental	Operating Temperature: -40°C to +85°C Storage Temperature: -40°C to +85°C Relative Humidity: 0 to 95% Noncondensing		[†] 240VAC between + and -/+EXC/-EXC terminals. 120VAC between - and +EXC/-EXC terminals and between +EXC and -EXC terminals. *Includes nonlinearity, hysteresis, and repeatability.		
DI-718B Specifications																																																																																																																													
Analog Inputs	Number of Channels: 8 configured for signal conditioned inputs Channel Configuration: Defined by DI-8B Module Measurement Range: Defined by DI-8B Module Accuracy: ±0.25% FSR (at 1800 S/s, averaging mode) Resolution: ±1 part in 8,192 Input Impedance: Defined by DI-8B Module Input offset voltage: Defined by DI-8B Module Channel-to-channel crosstalk rejection: -75db @ 100Q unbalance Offset temperature coefficient: 0.25µV/°C Digital filtering: Standard: Conditional over-sampling Stand-alone: None CJC Error: 1.5°C plus 8B Module																																																																																																																												
Isolation (via DI-8B Modules)	Input-to-Output: 1000VDC/Peak AC Channel-to-Channel: 500VDC/Peak AC																																																																																																																												
A/D Characteristics	Type: Successive approximation Resolution: 14-bit Monotonicity: ±2 LSB Conversion Time: 69.4µs																																																																																																																												
Scanning Characteristics	Max. throughput sample rate: Standard: 4,800 Hz Stand-alone: 14,400 Hz* Min. throughput sample rate: Standard: 0.0034 Hz Stand-alone: 0.0017 Hz Max. scan list size: 9 entries Sample buffer size: 2kb																																																																																																																												
Calibration	Calibration cycle: One year Calibration method: Calibration Software, provided. *Dependent on SD card used. Low speed SD cards can sample up to 2,000 Hz. High speed cards can sample up to 14,400 Hz. Some high speed cards cannot sample as high as 14,400 Hz but their capability can only be determined by trial and error (Model 101014-2G has been tested and approved).																																																																																																																												
Controls (Stand-alone models)	Single push-button: Provides manual control over Record and Standby																																																																																																																												
Digital I/O	Bits: 2 Inputs (Remote Storage and Remote Events) Input voltage levels: Min. required "1" 2V; Max allowed "0" 0.8V																																																																																																																												
Ethernet Interface	Type: 10/100Base-T Connector: RJ-45 Protocol: TCP/IP Server Type: DHCP or Fixed IP																																																																																																																												
Removable Memory (Stand-alone models)	Type: Standard SD (not SDHD or SDxC) Capacity: 16MB to 2GB																																																																																																																												
Real Time Clock (Stand-alone models)	Type: Date, hour, minute, second Resolution: 1 second Accuracy: 20 ppm																																																																																																																												
Transfer Rate to PC	Real Time: up to 4,800 samples per second From Memory Card: up to 3,000 samples per second																																																																																																																												
General	Panel indicators: Mode LED Panel Controls: Control push button (Stand-alone models) Panel Slots: Accepts MMC/SD-type flash memory Input connectors: Two, removable sixteen position terminal blocks Operating Environment: 0°C to 70°C Enclosure: Aluminum base with steel wrap-around. Dimensions: 5 7/8" D × 4 1/8" W × 1 1/2" H (13.81D × 10.48W × 3.81H cm) Weight: 14 oz. Power Requirements: USB: 9 to 36 VDC, 2 watts + 8B modules Ethernet: 9 to 36 VDC, 2.5 watts + 8B modules																																																																																																																												
Indicators	Stand-alone models: Three-color LED indicating Record, Standby, and Error conditions Standard models: Power LED																																																																																																																												
SPECIFICATIONS																																																																																																																													
Typical at T _A = +25°C and +5V Power																																																																																																																													
	DI-8B38-0x	DI-8B38-3x																																																																																																																											
Input Range	±10mV to ±100mV																																																																																																																												
Input Bias Current	±0.5nA																																																																																																																												
Input Resistance	Normal: 50MΩ Power Off: 100kΩ Overload: 100kΩ																																																																																																																												
Input Protection	Continuous: 240VAC Transient: ANSIIEEE C37.90.1																																																																																																																												
Excitation Output (-x1)	+3.333V ±2mV																																																																																																																												
Load Resistance	100Ω to 2kΩ																																																																																																																												
Excitation Output (-2x, -5x)	+10V ±5mV																																																																																																																												
Load Resistance	300Ω to 2kΩ																																																																																																																												
Excitation Load Regulation	1.5ppm/mA																																																																																																																												
Excitation Stability	50ppm/°C																																																																																																																												
Excitation Protection	120VAC																																																																																																																												
CMV Input to Output	1500Vrms max																																																																																																																												
Transient Input to Output	ANSIIEEE C37.90.1																																																																																																																												
CMR (50Hz or 60Hz)	100dB																																																																																																																												
NMR	100dB per decade above 8kHz																																																																																																																												
Accuracy[†]	±0.05% Span																																																																																																																												
Nonlinearity	±0.02% Span																																																																																																																												
Stability	Offset: ±25ppm/°C Gain: ±100ppm/°C																																																																																																																												
Noise	Output, 100kHz: 1500µVrms 200µVrms																																																																																																																												
Bandwidth, -3dB	8kHz																																																																																																																												
Response Time, 90% Span	70µs																																																																																																																												
Output Range	±5V																																																																																																																												
Output Protection	Continuous Short to Ground: ANSIIEEE C37.90.1 Transient: ±5VDC ±5%																																																																																																																												
Power Supply Voltage	+5VDC ±5%																																																																																																																												
Power Supply Current	110mA No Exc. Load 150mA Full Exc. Load																																																																																																																												
Power Supply Sensitivity	±50ppm/%																																																																																																																												
Mechanical Dimensions	1.11" × 1.65" × 0.40" (28.1mm × 41.9mm × 10.2mm)																																																																																																																												
Environmental	Operating Temperature: -40°C to +85°C Storage Temperature: -40°C to +85°C Relative Humidity: 0 to 95% Noncondensing																																																																																																																												
[†] 240VAC between + and -/+EXC/-EXC terminals. 120VAC between - and +EXC/-EXC terminals and between +EXC and -EXC terminals. *Includes nonlinearity, hysteresis, and repeatability.																																																																																																																													

Figure 29: Specification sheet for: a) DATAQ data logger; b) strain gage amplifier

3.4.2.2 National Instruments (NI) data logger

A National Instruments data acquisition system was the main system used during the testing series described in this thesis. It consists of a PC fit with a PCI-E 6323 card. This is connected to a SCXI 1349 adapter that contains a SCXI 1520 strain/bridge input module. It is housed in a SCXI 1001 chassis with a SCXI 1314 terminal block. The sensors connect to the terminal block and strain data can be viewed in real time with the PC monitor. It was powered by a generator during the testing series. This system provided the most user friendly interface that allowed for simple organization of the

many acquired data files. The main components of this data acquisition system are shown in Figure 30.

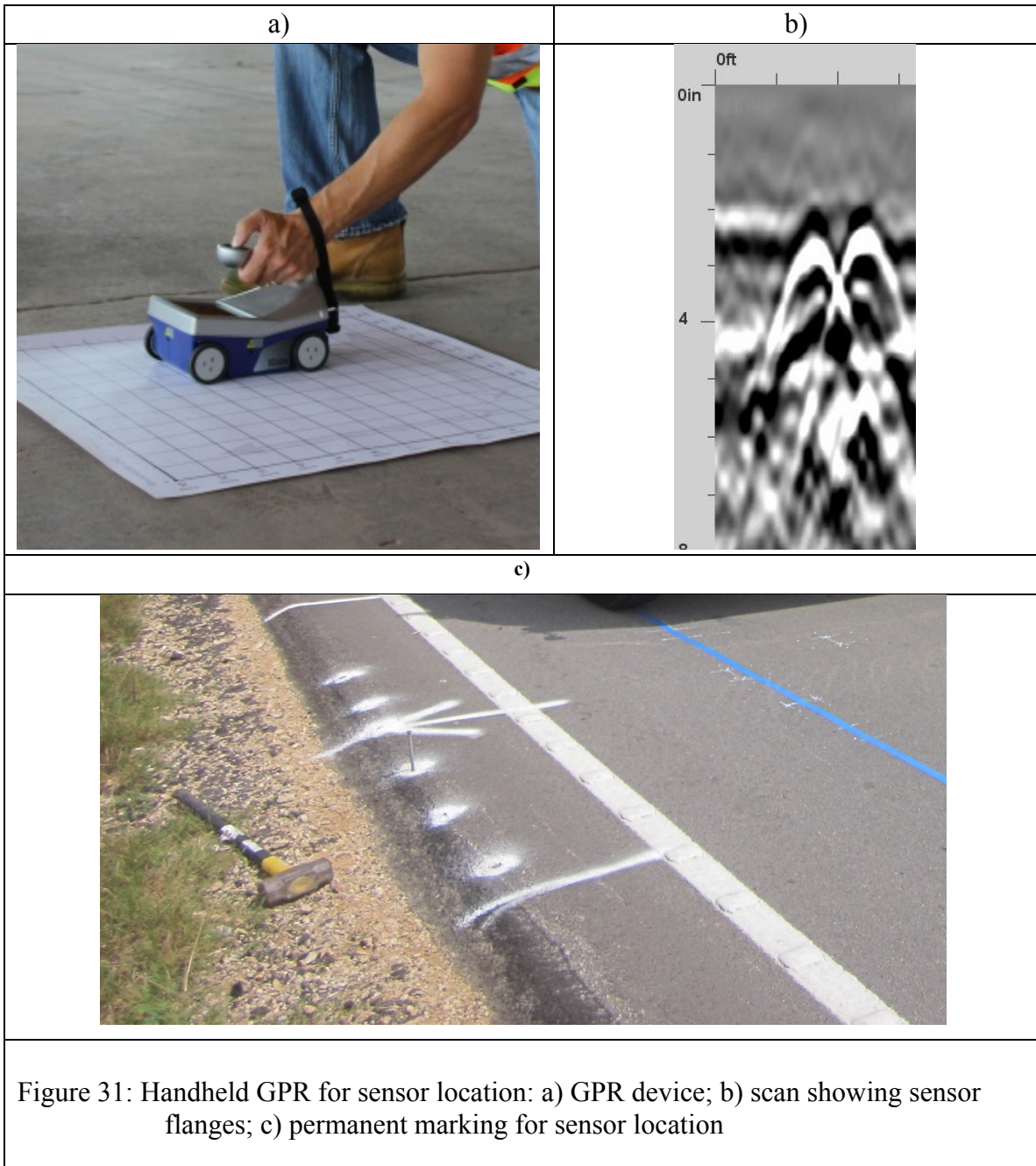


Chapter 4. Field Testing Campaign

On the days of June 26 and 27 of 2017, a series of controlled loading tests were conducted with the help of TxDOT. These tests included heavy load passes directly over the wheel paths at different speeds, heavy load passes offset towards the white line at different speeds, light load passes directly over the wheel paths at different speeds, FWD directly on each working sensor, and static loading with the heavy truck directly over the wheel paths. The purpose of this loading program was to generate accurate strain results for comparison among the different test sections.

4.1 IDENTIFICATION OF SENSOR LOCATIONS

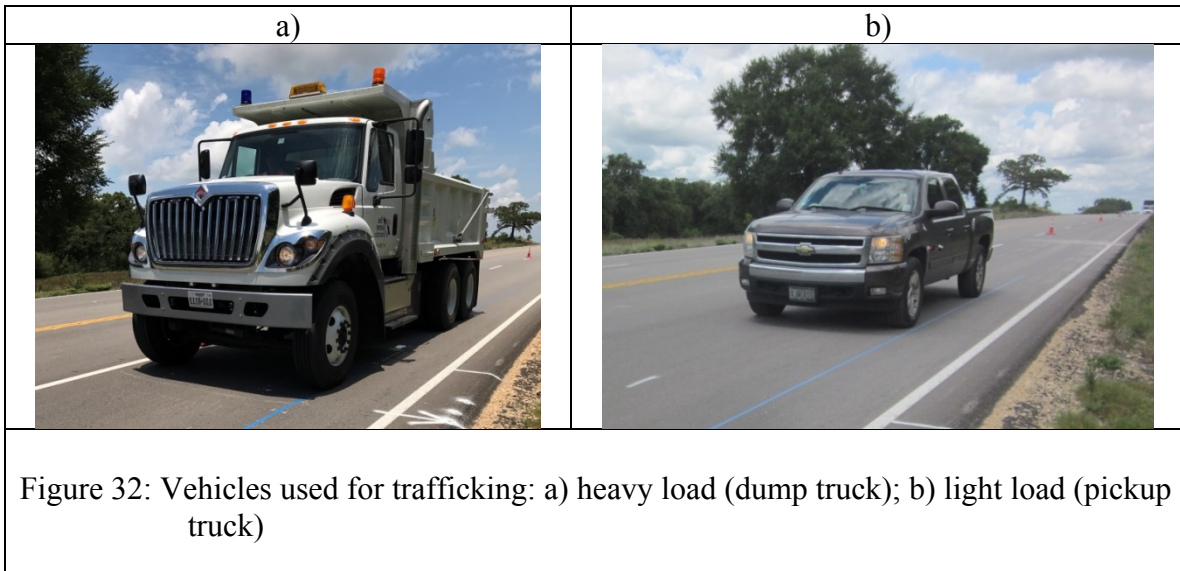
The installed sensors were located previous to the start of the testing campaign. This was done using a handheld GPR, such as that shown in Figure 31 a. The GPR had a screen that showed the scan directly below the device. The sensors were found by locating the flanges in one direction then the center component in the other direction. Figure 31 b. is a scan from the GPR showing the flanges of a strain gage. After locating and marking each sensor, a path was laid out for the vehicles to travel directly over them. The location of each sensor was also marked with a large nail on the shoulder and the perpendicular distance from the nail to the sensor was noted. Figure 31 c. shows the nail partially driven into the pavement. This was done so the sensors can be easily found in the future.

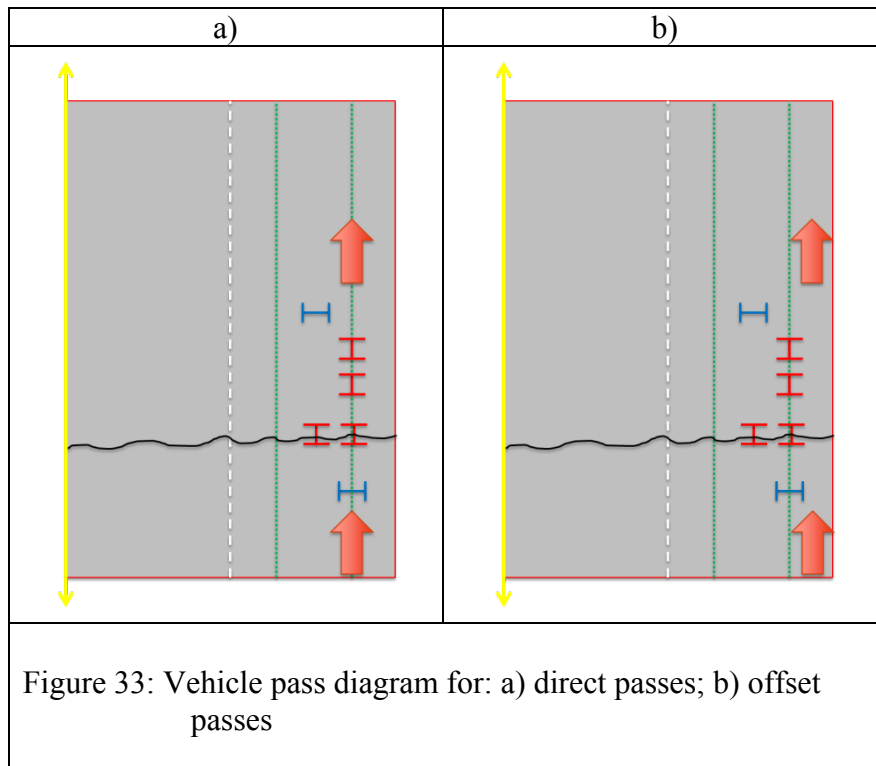


4.2 VEHICLE PASSES

The vehicle passes were conducted using two vehicles of different weights. The heavy vehicle passes were performed by a TxDOT employee driving a dump truck loaded with base material from a local stockpile. The dump truck has three total axles including the front steering axle and a rear tandem axle. The truck was weighed at a local feed stored showing a total weight of 48,460 lbs. The tire pressure was 120psi. The truck conducted 10 passes directly in the wheel path and 10 passes offset from the wheel paths towards the shoulder at 15mph. The direct and offset passes were then repeated with an increased velocity of 25mph. Figure 33 shows the vehicle trajectory for direct and offset passes.

The light vehicle passes were performed by the research team driving a pickup truck. The pickup truck is a standard, two-axle truck. It was weighed at a local feed stored showing a total weight of 6,240 lbs. The tire pressure was 40psi. The truck conducted 10 passes directly in the wheel path at 15mph and 10 passes directly in the wheel path at 25mph. Figure 32 shows the vehicles used for traffic passes.





4.3 FALLING WEIGHT DEFLECTOMETER TESTING

Falling weight deflectometer (FWD) testing was conducted by a TxDOT employee. The FWD is typically used for correlating strength and thickness values of the different pavement layers to the vertical deflections induced by the impulse load. For the purpose of this study, the induced strains were measured for each drop. This was done by maneuvering the testing equipment so that the actual impulse load would be directly over a given sensor. The test consisted of five drops at different energy levels. The first two drops were at 6,000 lbs. and were meant to be the seating load. The third drop was also at 6,000 lbs. followed by a 9,000 lb. drop and a 12,000 lb. drop. The data acquisition system measuring strain response captured each of the drops from the FWD tests. Due to the consistency among the drops and the ability to target the exact location of the sensors, this testing series was expected to be conducted with comparatively higher precision as compared to traffic loading. Figure 34 shows a schematic of the deflection basin and the equipment used during the testing campaign.



Figure 34: FWD equipment used during controlled testing campaign

4.4 STATIC LOADING

Static testing was performed using the same dump truck with a total weight of 48,460 lbs. The driver of the truck maneuvered directly on the wheel path with the

passenger side tires. The truck moved forward at a slow speed until the front tire was directly over a given sensor at which point the driver was instructed to stop for a two-second count. This was done for each of the four sensors located in the wheel path, and then conducted again for the second axle of the vehicle. Each of the sections was tested twice. The purpose of this testing series was to clearly capture the induced compressional and tensile strains associated with vehicle passes. Figure 35 shows the dump truck placing the front tire directly on a sensor.



Figure 35: Maneuvering dump truck directly on the sensors during static testing

Chapter 5. Results of Field Campaign

5.1 CONTROLLED TESTING CAMPAIGN

5.1.1 Traffic Loading

Vehicle passes were conducted in order to represent public traffic traveling along the project site. A number of scenarios were considered for this analysis including heavy passes by a dump truck and light passes by a pickup truck. The passes were made at 15mph and 25mph. The impact of variability on the wheel trajectory was assessed by conducting passes directly in the wheel path as well as offset towards the shoulder.

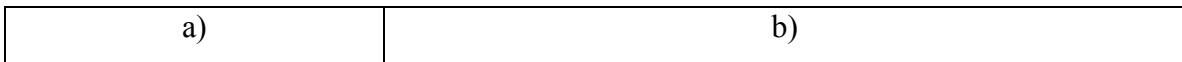
5.1.1.1 Data Evaluation

To evaluate the strains for a given sensor, each pass is plotted with the maximum strain magnitude at the intersection of the y-axis. Figure 36 a. shows this plot for Sensor 14 from the 15mph passes with a dump truck. Figure 1 b. shows the plot corresponding to the light weight pickup truck pass at 15mph for the same sensor. The range is then taken from the maximum strain value to the minimum strain value that occurs immediately before. The range is taken because the asphalt goes into a compressional, or tensile, state as the vehicle approaches and is then subjected to a peak strain level as the vehicle is directly on the sensor. This then allows for the entire strain response to be measured instead of just one component of the strain response. Not every pass occurred directly over a given sensor so detailed notes were taken during the time of testing that said whether the pass was direct or offset to the left or right. The plot is also analyzed to identify any passes that characterized as outliers. It was found that approximately 7 out of every 10 passes were directly over the sensors in the wheel path.



Figure 36: Example asphalt strain gages data recorded under controlled trafficking: a) heavy load (dump truck) trafficking; b) light load (pickup truck)

Once the range was found from each pass, the minimum value, first quartile, median value, third quartile, and max value were used to create a column chart. This chart, called a bar and whisker plot, shows the bulk of the range values within the colored section with the max and min values shown as error bars. Figure 37 shows an example bar and whisker plot for Sensor 14 as well as the range values found from Figure 36 a. Extra passes would be conducted if there was a noticeable error in trajectory or an equipment malfunction as shown by the 13 passes in Figure 37 a. This plot allows analysis of all the passes statistically and is beneficial to evaluate variability and sensitivity. The bar and whisker plots will be used throughout the results chapter to evaluate vehicle passes.



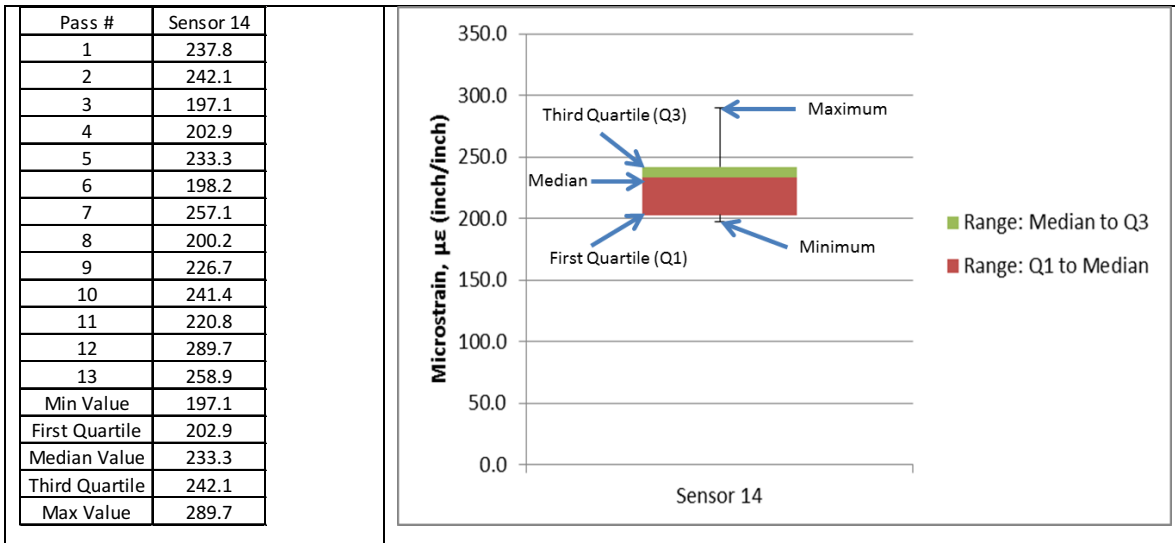


Figure 37: Example of vehicle pass strain data shown in: a) tabular form; b) bar and whisker plot

5.1.1.2 Heavy Load Passes Directly Over Sensors

A loaded dump truck was used for the Heavy Load passes with a total weight of 48,460 lbs. This was done by marking the exact location of each of the sensors and laying out a pathway directly over each of the sensors in the wheel path. An experienced driver then carefully drove along the marked pathway for 10 passes at a lower speed of 15mph and 10 passes at a higher speed of 25mph. This was done for each of the three sections. The accuracy of each pass was monitored via a camera overlooking the right side front tire.

In this section, the obtained strain data from heavy load passes is compared within each test section, among various sensors, as well as among the various test sections for the sensors installed with the same layout configuration.

5.1.1.2.1 Comparison of Strain Data within Each Test Section

Strain comparisons within this section include readings from sensors placed on a crack versus sensors placed away from a crack and longitudinal sensors versus transverse sensors. The sensor comparisons are laid out in the following list.

Placement – Crack vs. No Crack

- i. ASG 1, ASG 2 vs. ASG 3, ASG 4, ASG 5, ASG 6
- ii. ASG 8, ASG 9 vs. ASG 7, ASG 10, ASG 11, ASG 12
- iii. ASG 14, ASG 15 vs. ASG 13, ASG 16, ASG 17, ASG 18

Preexisting cracks allow for the asphalt layers to act independently on each side of the preexisting crack, with areas of increased stress intensity at the crack locations typically leading to early reflective cracking through new pavement layers. An evaluation of strains measured at the crack locations was expected to indicate the likeliness of reflective cracking to occur.

In addition, the comparison of longitudinal versus transverse strain gages in each section follows the order shown in the list below.

Orientation – Longitudinal vs. Transverse Strain Gage

- i. ASG 1, ASG 2, ASG 4, ASG 6 vs. ASG 3, ASG 5*
- ii. ASG 7, ASG 8, ASG 9, ASG 11 vs. ASG 10, ASG 12*
- iii. ASG 14, ASG 15, ASG 16, ASG 17 vs. ASG 13, ASG 18*

Longitudinal strain gages measure strain in the direction of traffic flow whereas transverse strain gages measure strains in the lateral direction of the road. There are different trends in the asphalt strains as a vehicle approaches a given location from when it is directly on top of a given location, and finally as it moves away. The asphalt layers experience strains both in tension and compression.

The comparison among sections is for each sensor location. There are two sensors in each section that are located between the wheel path and four sensors located within the right hand wheel path. As a vehicle passes directly over the wheel path, stresses are transferred to areas between the wheel paths. The comparison of sensor location includes the following sensors for each section.

Location – Wheel Path vs. Between Wheel Paths

- i. ASG 1, ASG 3, ASG 4, ASG 6 vs. ASG 2, ASG 5*
- ii. ASG 7, ASG 9, ASG 10, ASG 11 vs. ASG 8, ASG 12*
- iii. ASG 13, ASG 14, ASG 16, ASG 17 vs. ASG 15, ASG 18*

Sensors 1 through 6 are evaluated to capture the strains developed in Section 1 from the heavy load passes. All but Sensor 2 were operational during the time of the 15mph passes, and Sensor 3 stopped working before the 25mph passes were completed. Sensors 1, 3, 4, and 6 are in the wheel path and Sensor 5 is between the wheel paths. Sensor 3 and 5 are in the transverse orientation and the rest are longitudinal. Sensor 1 is the only working sensor in Section 1 placed on a crack. Section 1 is reinforced with a polyester geosynthetic.

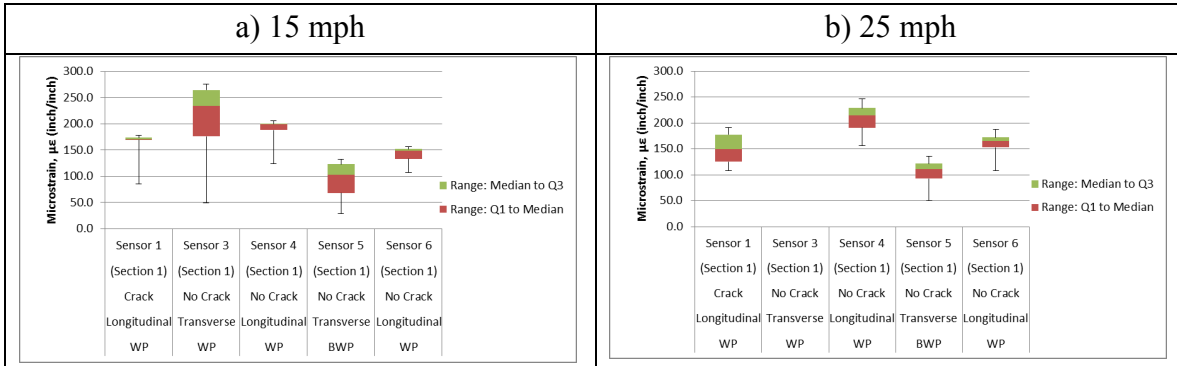


Figure 38: Section 1 Strain Response for Heavy Loading: a) trafficking at 15mph; b) trafficking at 25mph.

Figure 38: a. shows the strain response of each sensor within Section 1 for heavy passes at 15mph. The maximum strain response for each sensor in the order shown (Sensor 1, Sensor 3, Sensor 4, Sensor 5, Sensor 6) was $178\mu\epsilon$, $276\mu\epsilon$, $206\mu\epsilon$, $132\mu\epsilon$, and $157\mu\epsilon$, respectively (also compare the 3rd quartile values). Sensor 1 is the only working sensor in this section placed on a crack and it shows a lower strain response than sensor 4 but higher strains than sensor 6. Sensor 1 also shows a consistent response with the median and third quartile values being close to the maximum value. It is expected that strains around a crack would be greater due to the discontinuity of the pavement layers but the crack behavior can be difficult to predict. Sensor 3 is in the transverse direction and shows the greatest maximum strain reading as well as the most variability. It is more sensitive to small changes in the wheel's trajectory because it captures strains in the lateral direction. Sensor 5 is also in the transverse orientation and shows more variability than other sensors. It has the lowest maximum strain reading due to its location between the wheel paths.. The last comparison is between sensor 4 and sensor 6. Each of these sensors are located in the wheel path oriented and placed away from a crack. It is expected that the sensors would have very similar strain responses but that is not the case here with sensor 4 showing nearly $50\mu\epsilon$ more than sensor 6.

Figure 38 b. shows the strain response of each of the sensors within Section 1 for heavy passes at an increased speed of 25mph. The maximum strain response for each sensor in the order shown (Sensor 1, Sensor 4, Sensor 5, Sensor 6) is $191\mu\epsilon$, $246\mu\epsilon$, $136\mu\epsilon$, and $188\mu\epsilon$ respectively. Each of the working sensors during this testing series show the same trend as the lower speed passes with the exception of increased variability among wheel path sensors and decreased variability from Sensor 5. The strain readings from a given sensor are similar from both velocities.

The sensors within Section 2 are Sensor 7 through Sensor 12. Only Sensor 8 and Sensor 12 were working during the heavy load passes. Sensor 8 was placed on a crack between the wheel paths in the longitudinal direction, and Sensor 12 is in the transverse direction placed away from a crack also located between the wheel paths. Section 2 is reinforced with a polyvinyl geosynthetic.

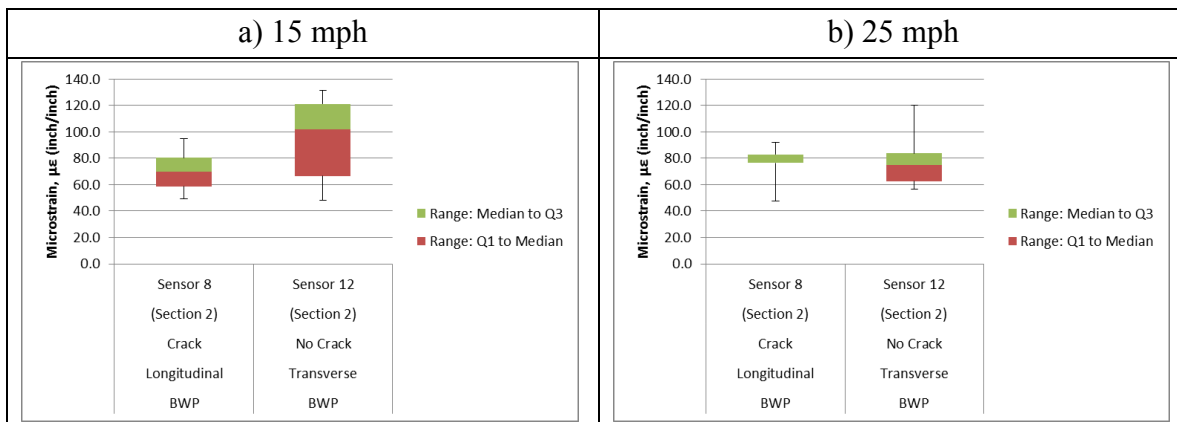


Figure 39: Section 2 Strain Response for Heavy Loading: a) trafficking at 15mph; b) trafficking at 25mph.

Figure 39 shows the strain response from each working sensor within Section 2. Unfortunately, none of the sensors within the wheel path were working so the comparison of strain gage data is limited. Sensor 8 and sensor 12 had a maximum strain response of 95µε and 131µε, respectively, for the 15mph passes and 92µε and 120µε for the 25mph passes. Sensor 8 was placed on a preexisting crack in the longitudinal direction and is less sensitive to passes within the wheel path. Sensor 12 was in the transverse direction and shows greater strains from vehicle passes. The strain in the lateral direction is expected to be greater than the strain in the longitudinal direction for sensors between the wheel paths due to the presence of reinforcement. The reinforcement provides a means of load transfer to the area between the wheel paths. It is also expected that the transverse strain gage will have more variability due to different wheel trajectories and that is shown here by Sensor 12.

The 25mph passes resulted in slightly lower strain readings and decreased variability. This is expected due to the asphalt acting more rigidly from the faster loading rate. It transfers the vehicle load to the area between the wheel paths more efficiently.

Sensors 13 through 18 are used to capture the strains developed in Section 3 for the heavy vehicle passes. Sensor 13, 14, and 17 are each in the wheel path. Sensor 14 and

Sensor 15 are placed on a crack in the longitudinal direction. Sensor 13 and Sensor 18 are in the transverse direction. There is no reinforcement installed in Section 3.

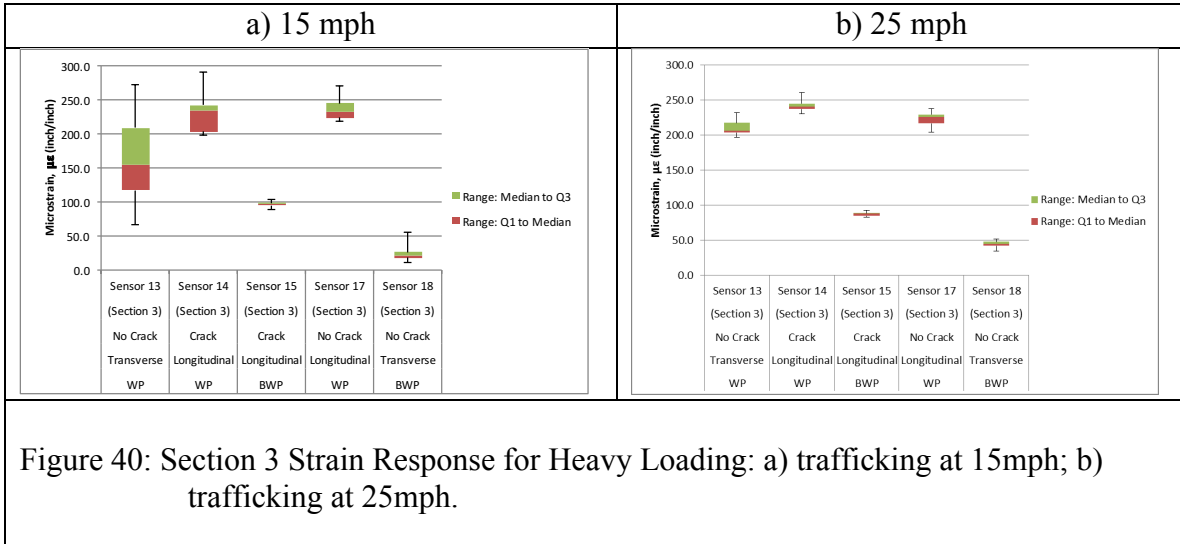


Figure 40: Section 3 Strain Response for Heavy Loading: a) trafficking at 15mph; b) trafficking at 25mph.

Figure 40 a. shows the strain response for each of the working sensors within Section 3 during the 15mph passes. The maximum strain readings for each sensor in the order shown (Sensor 13, Sensor 14, Sensor 15, Sensor 17, Sensor 18) are $272\mu\epsilon$, $290\mu\epsilon$, $104\mu\epsilon$, $271\mu\epsilon$, and $56\mu\epsilon$. Figure 40 b. shows the strain response during the 25mph passes. The maximum strain readings for each sensor during the higher speed passes in the order shown (Sensor 13, Sensor 14, Sensor 15, Sensor 17, Sensor 18) are $232\mu\epsilon$, $261\mu\epsilon$, $93\mu\epsilon$, $238\mu\epsilon$, and $52\mu\epsilon$. Strain comparisons within this section include crack versus no crack, longitudinal versus transverse, and wheel path versus between wheel paths. Sensor 14 is on a preexisting crack in the wheel path and shows the greatest strain response at each speed. Sensor 15 is also on a preexisting crack and shows greater strains than Sensor 18. This is different than in Section 2 because there is no reinforcement in this section. The lack of reinforcement allows sensors between the wheel paths to act more independently from loading within the wheel paths, so it is expected that the crack will have a greater effect on strain response. It is also shown here that Sensor 13 has significant variability during the 15mph passes. This is expected because it is oriented in the transverse direction and is more sensitive to wheel trajectory. Lastly, it is clear here that the strain readings from sensors within the wheel path are greater than the sensor between the wheel paths. This is expected due to them being loaded directly by the vehicle tire.

5.1.1.2.2 *Comparison of Strain Data among Different Test Sections*

Each section contains sensors placed in the same configuration. This includes six total sensors per section, four of which are in the wheel path with the other two located between the wheel paths. Of the four wheel path sensors, three are in the longitudinal direction with one of them on a crack, and the fourth is in the transverse direction. The sensors between the wheel paths are in the longitudinal direction on a crack as well as in the transverse direction away from a crack.

Section 1 is reinforced with a polyester (PET) geosynthetic interlayer, Section 2 is reinforced with a stiffer, polyvinyl (PVA) geosynthetic interlayer, and Section 3 is unreinforced. The strain comparisons among different sections aim at providing insight into the structural benefits of interlayer reinforcement as well as the benefits regarding the retardation of reflective cracking. This is achieved by comparing the longitudinal and transverse strain results from a given section to their matching counterparts within other sections, as well as the comparison of longitudinal strains developed on preexisting cracks from each section. These comparisons include the following sensors from each section.

- a. Longitudinal ASG in Wheel Path Not on Crack
 - i. ASG 4, ASG 6
 - ii. ASG 7, ASG 11
 - iii. ASG 16, ASG 17
- b. Transverse ASG in Wheel Path Not on Crack
 - i. ASG 3
 - ii. ASG 10
 - iii. ASG 13
- c. Transverse ASG Between Wheel Paths Not on Crack
 - i. ASG 5
 - ii. ASG 12
 - iii. ASG 18
- d. Longitudinal ASG in Wheel Path on Crack
 - i. ASG 1
 - ii. ASG 9
 - iii. ASG 14
- e. Longitudinal ASG Between Wheel Paths on Crack
 - i. ASG 2
 - ii. ASG 8
 - iii. ASG 15

5.1.1.2.2.1 Longitudinal Strain in Wheel Path

The longitudinal strain in the wheel path is measured by two sensors in each section. Sensor 4 and 6 are in Section 1, Sensor 7 and 11 are in Section 2, and Sensor 16 and 17 are in Section 3. Sensor 7, 11, and 16 did not work at the time of the heavy load passes so there is no data shown from them. Section 1 is reinforced with a polyester geosynthetic, Section 2 is reinforced with a polyvinyl geosynthetic, and Section 3 is unreinforced.

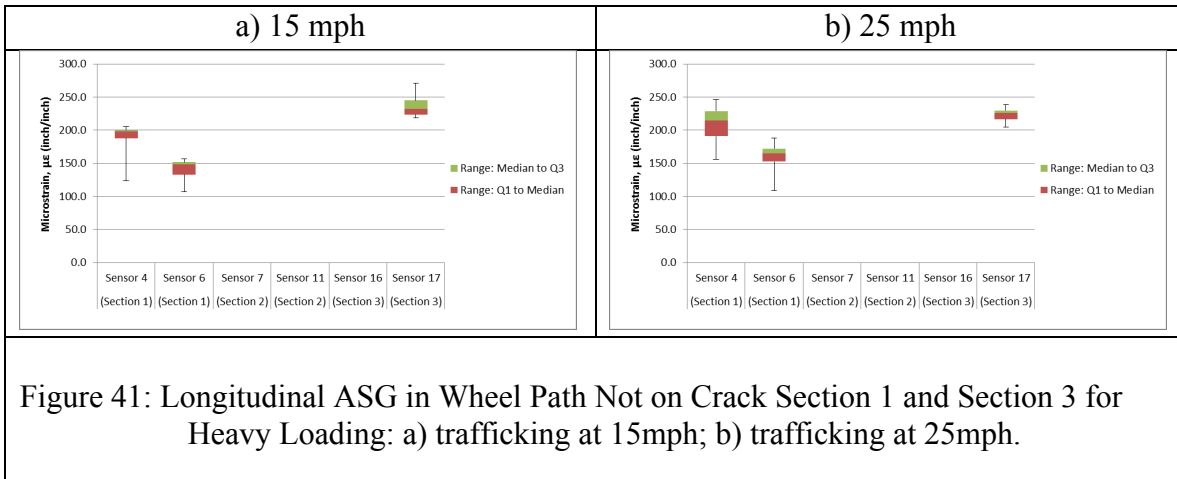


Figure 41: Longitudinal ASG in Wheel Path Not on Crack Section 1 and Section 3 for Heavy Loading: a) trafficking at 15mph; b) trafficking at 25mph.

Figure 41 a. shows the longitudinal strain gages in the wheel path placed away from a preexisting crack for each section during the 15mph passes. Sensor 17 has the greatest maximum strain response of 271µε followed by Sensor 4 at 206µε and Sensor 6 at 157µε. The reinforcement within Section 1 is expected to resist the tensile stresses from a given load that results in less tensile strain. This is clearly shown in the strain results from the 15mph passes.

Figure 41 b. shows the same strain gages in each section during the 25mph passes. In this case, Sensor 4 shows the greatest maximum strain reading of 246µε followed by Sensor 17 at 238µε and Sensor 6 at 188µε. Although this is not the expected order of maximum strain readings, the third quartile and median values are greater from Sensor 17 than the others. This indicates the strain readings are consistently higher in Section 3 where there is no reinforcement.

5.1.1.2.2.2 Transverse Strain in Wheel Path

The transverse strain in the wheel path is measured by Sensor 3 in Section 1, Sensor 10 in Section 2, and Sensor 13 in Section 3. Sensor 10 was not operational during

the time of the heavy vehicle passes and Sensor 3 stopped working before the 25mph passes were completed so no data is shown.

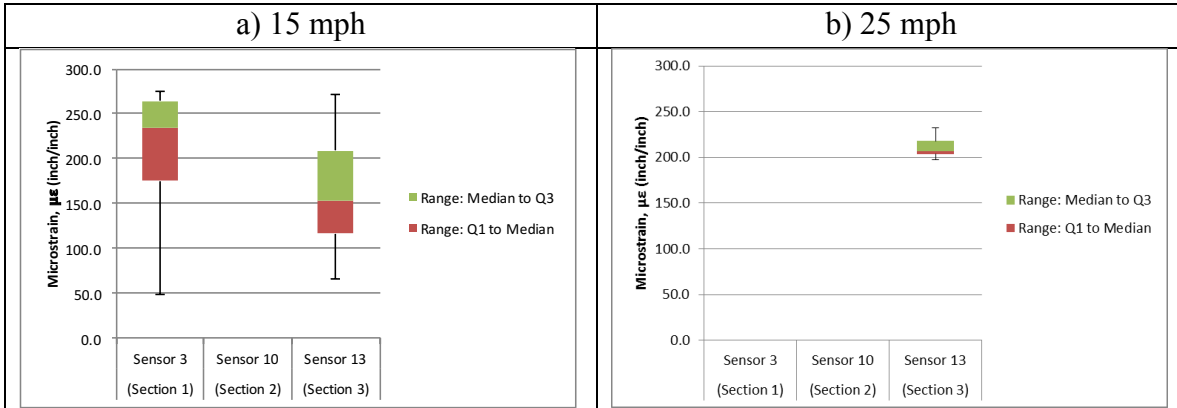


Figure 42: Transverse ASG in Wheel Path Not on Crack Section 1 and Section 3 for Heavy Loading: a) trafficking at 15mph; b) trafficking at 25mph.

Figure 42 shows the transverse strain gages in the wheel path placed away from a crack for each section. From the 15mph passes, Sensor 3 shows a maximum strain response of 276µε which is greater than the response from sensor 13 of 272µε. Although the maximum strain readings are very similar, this is not expected due to the presence of reinforcement within Section 1. From the 25mph passes, Sensor 13 shows a maximum strain response of 232µε. Although this is slightly lower than the max reading from the 15mph passes, the bulk of the passes led to larger developed strains.

5.1.1.2.2.3 Transverse Strain between Wheel Paths

The transverse strain between the wheel paths is measured by Sensor 5 in Section 1, Sensor 12 in Section 2, and sensor 18 in Section 3. Section 1 is reinforced with a polyester geosynthetic, Section 2 is reinforced with a polyvinyl geosynthetic, and Section 3 is unreinforced.

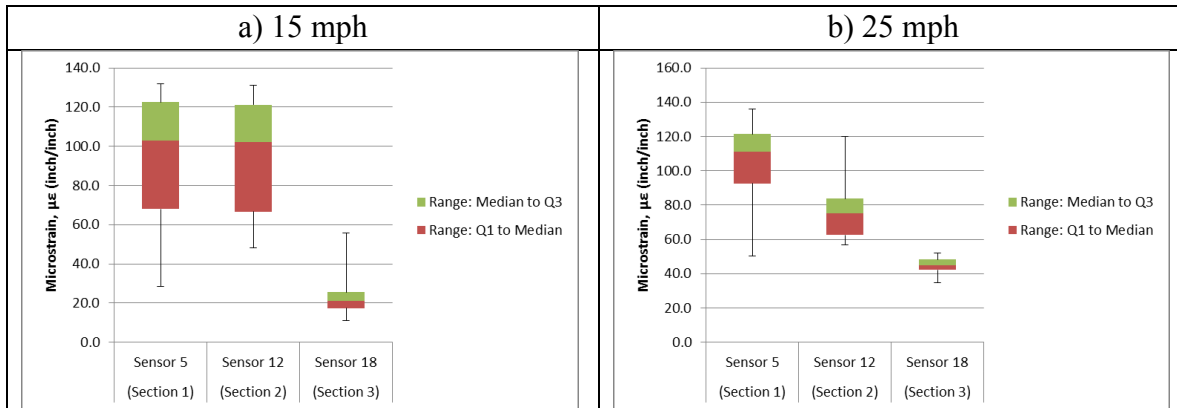


Figure 43: Transverse ASG Between Wheel Paths Not on Crack Section 2 and Section 3 for Heavy Loading: a) trafficking at 15mph; b) trafficking at 25mph.

Figure 43 shows the transverse strain gages between the wheel paths away from a crack for each section. The low speed passes gave maximum strain readings from Sensor 5, 12, and 18 of 132 $\mu\epsilon$, 131 $\mu\epsilon$, and 56 $\mu\epsilon$, respectively. The high speed passes gave maximum strain readings of 136 $\mu\epsilon$ for Sensor 5, 120 $\mu\epsilon$ for sensor 12, and 52 $\mu\epsilon$ for sensor 18. The reinforcement within Section 1 and Section 2 transfers the stresses from the wheel path to the area between the wheel paths and renders greater strains in the transverse direction. The lack of reinforcement within Section 3 causes the stresses and associated strains to act locally, therefore the area between the wheel paths do not undergo significant strains.

The low speed passes show strain readings that are slightly lower for each of the sensors. This indicates that the pavement structure behaves rigidly during the high speed passes and the load from the wheels is transferred to the area between the wheel paths.

5.1.1.2.2.4 Longitudinal Strain in Wheel Path on a Preexisting Crack

The longitudinal strain in the wheel path on a preexisting crack is monitored by Sensor 1 from Section 1, Sensor 9 from Section 2, and Sensor 14 from Section 3. Sensor 9 does not work so there is only data shown from Sensor 1 and Sensor 14. Section 1 is reinforced with a polyester geosynthetic and Section 3 is unreinforced.

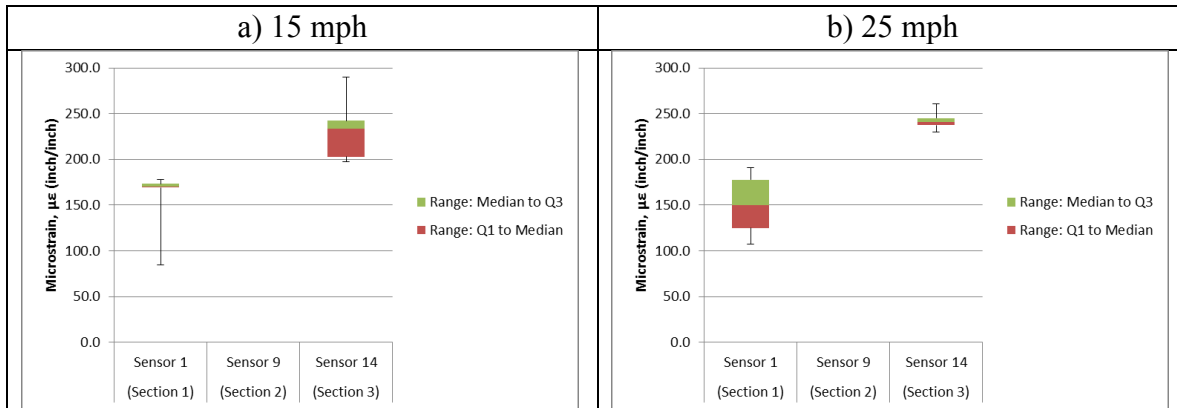


Figure 44: Longitudinal ASG in Wheel Path on Crack Section 1 and Section 3 for Heavy Loading: a) trafficking at 15mph; b) trafficking at 25mph.

Figure 44 shows the longitudinal strain gages within the wheel path placed on a crack for each section. Sensor 9 from Section 2 did not work during testing, so there are no results shown. During the 15mph passes, Sensor 1 and Sensor 14 show maximum strain readings of 178µε and 290µε, respectively. The 25mph passes gave maximum strain readings of 191µε from Sensor 1 and 261µε from Sensor 14. The reinforcement in Section 1 creates continuity within the pavement structure that decreases the differential movement on either side of the crack. This leads to lower strains as shown here. Section 3 is unreinforced so the asphalt overlay is the only layer within the pavement that is continuous. The increased strain at the preexisting crack location may eventually lead to propagation through the new overlay.

5.1.1.2.2.5 Longitudinal Strain between Wheel Paths on a Preexisting Crack

The longitudinal strain between the wheel paths on a preexisting crack is measured by Sensor 2 from Section 1, Sensor 8 from Section 2, and Sensor 15 from Section 3. Sensor 2 from Section 1 did not work so there is only data shown from Sensor 8 and Sensor 15. Section 2 is reinforced with a polyvinyl geosynthetic reinforcement and Section 3 is unreinforced.

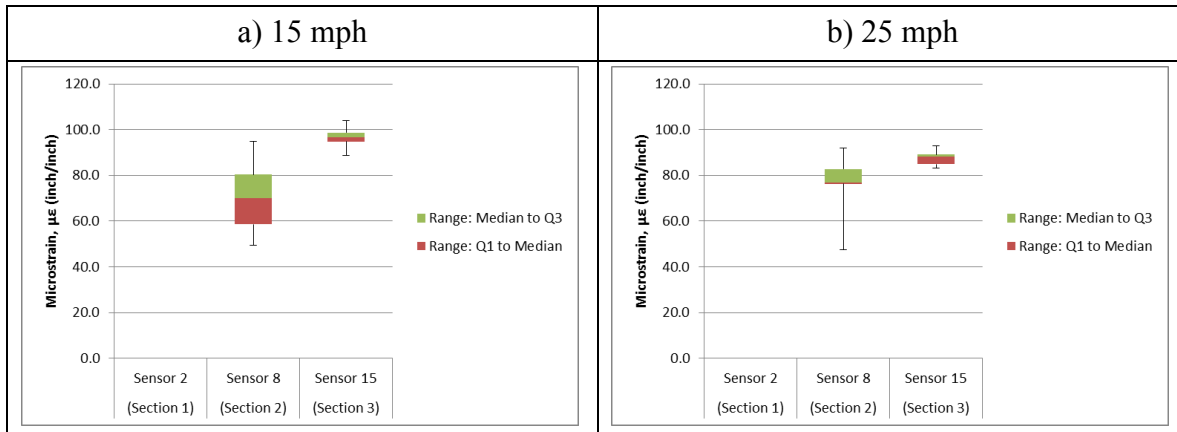


Figure 45: Longitudinal ASG Between Wheel Paths on Crack Section 2 and Section 3 for Heavy Loading: a) trafficking at 15mph; b) trafficking at 25mph.

Figure 45 shows the longitudinal strain gages located between the wheel paths on a crack for each section. From the 15mph passes, Sensor 8 has a maximum strain reading of $95\mu\epsilon$ and Sensor 15 has a max reading of $104\mu\epsilon$. This indicates that the crack in Section 3 allows more strain development due to the lack of reinforcement and can eventually lead to the propagation of reflective cracking.

From the 25mph passes, the maximum strain readings for Sensor 8 and Sensor 15 are $92\mu\epsilon$ and $93\mu\epsilon$, respectively. The third quartile and median value are nearly $10\mu\epsilon$ less for Sensor 8 than for Sensor 15. Therefore, the higher speed passes follow the same trend as the low speed passes showing greater strains on the crack where there is no reinforcement.

The strain response from Sensor 8 is very similar from both velocities with the 15mph passes showing slightly more variation. Sensor 15, however, shows an increased strain response during the slower passes. This is expected due to the slower loading rate on a viscoelastic material.

5.1.1.3 Light Load Passes Directly Over Sensors

A pickup truck was used for the Light Load passes with a total weight of 6,240 lbs. This was done by marking the exact location of each of the sensors and laying out a pathway directly over each of the sensors in the wheel path. The truck was then carefully driven along the marked pathway for 10 passes at a lower speed of 15mph and 10 passes

at a higher speed of 25mph. This was done for each of the three sections. The accuracy of each pass was monitored via a camera overlooking the right side front tire.

5.1.1.3.1 *Comparison of Strain Data within Each Test Section*

Sensor 1 through Sensor 6 is used to capture the strains developed in Section 1 from the light load passes. Sensor 1, 4, and 6 were the only working sensors during this time. Each of them is in the wheel path oriented in the longitudinal direction and Sensor 1 is placed on a crack. Section 1 is reinforced with a polyester geosynthetic.

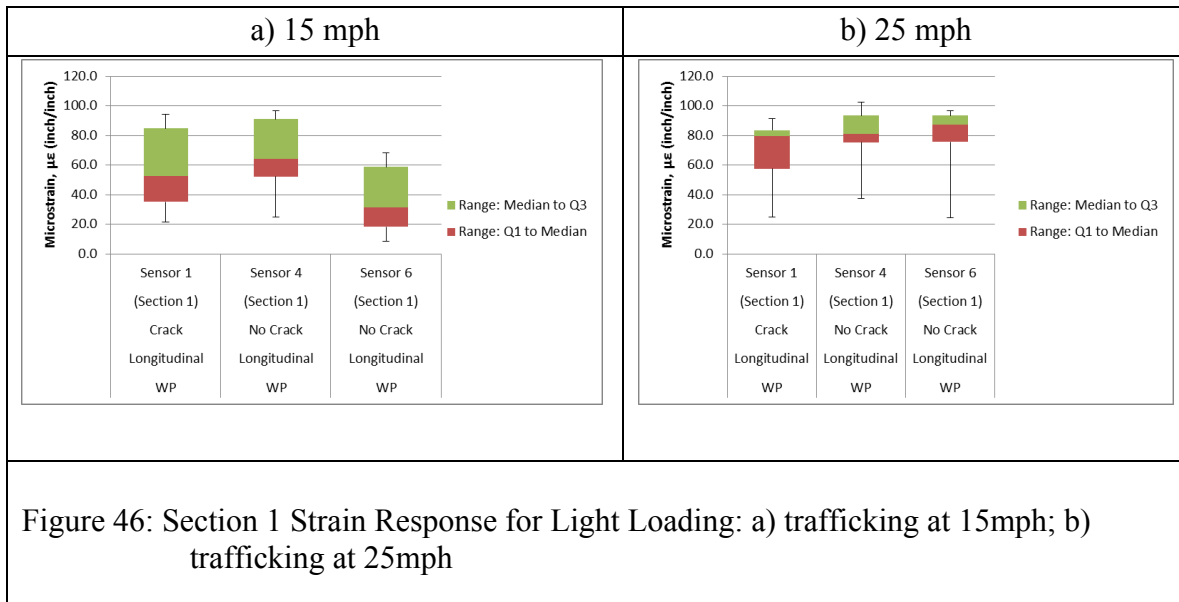


Figure 46: Section 1 Strain Response for Light Loading: a) trafficking at 15mph; b) trafficking at 25mph

Figure 46a. shows the strain response of each of the sensors within Section 1 for the 15mph passes. The maximum strain response for each sensor in the order shown (Sensor 1, Sensor 4, Sensor 6) is 94µε, 97µε, and 68µε respectively. Strain comparisons within this section include crack versus no crack and repeated sensors. Sensor 1 is the only sensor in this section placed on a preexisting crack and it shows greater strains than Sensor 6 but slightly less than Sensor 4. It is expected that strains around a crack would be greater due to the discontinuity of the pavement layers but Sensor 4 has shown consistently higher strains than the other sensors within Section 1. The last comparison is between Sensor 4 and Sensor 6. Each of these sensors are located in the wheel path in the longitudinal direction and placed away from a crack. It is expected that the sensors would have very similar strain responses but that is not the case here with Sensor 4 showing nearly 30µε more than Sensor 6.

Figure 46 b. shows the strain response within Section 1 for the 25mph passes. The maximum strain response for each sensor in the order shown (Sensor 1, Sensor 4, Sensor 6) is 92µε, 103µε, and 97µε respectively. Strain comparisons within this section are the

same as the 15mph passes. Sensor 1 shows the lowest strains although it is placed on a preexisting crack. Sensor 4 shows higher strain readings than Sensor 6, which is consistent to results from other testing series. The strain readings from Sensor 1 for both velocities are comparable to the strains measured by other sensors. This indicates that the reinforcement decreases the effects of the crack and creates a more uniform longitudinal strain profile within the wheel path.

Section 2 includes Sensors 7 through 12. Similar to the heavy vehicle passes, only Sensor 8 and Sensor 12 were working during this time. Sensor 8 is placed on a preexisting crack between the wheel paths in the longitudinal direction, and Sensor 12 is in the transverse direction placed away from a crack also located between the wheel paths. Section 2 is reinforced with a polyvinyl geosynthetic.

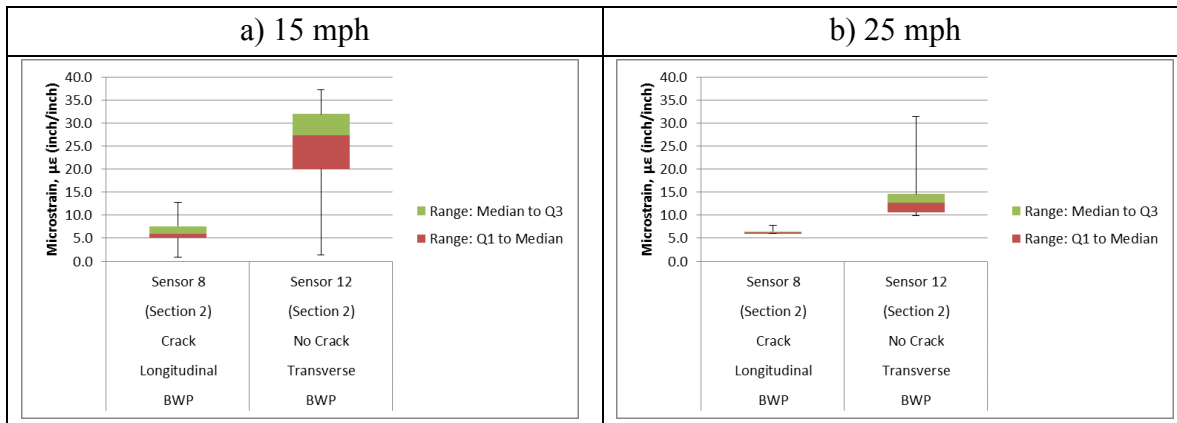


Figure 47: Section 2 Strain Response for Light Loading: a) trafficking at 15mph; b) trafficking at 25mph

Figure 47 a. shows the strain response from each working sensor within Section 2. Both sensors shown are located between the wheel paths. Sensor 12 shows a greater maximum strain response of $37\mu\epsilon$ compared to Sensor 8 at $13\mu\epsilon$. Figure 47 b. shows the strain response from the same sensors for the 25mph passes. Similarly, Sensor 12 shows a greater maximum strain response of $32\mu\epsilon$ compared to Sensor 8 at $8\mu\epsilon$. This is expected due to the transverse orientation of Sensor 12 in a reinforced section. As mentioned before, the reinforcement allows for more load transfer to the area between the wheel paths. This load acts laterally from the wheel paths as a vehicle passes and leads to higher strains in the transverse direction. The reinforcement also decreases the effects of the crack by decreasing the stress intensity at the crack location. This leads to less strain development at the location of Sensor 8. There is a slightly lower strain response from

each sensor during the higher velocity passes. This is expected due to the faster loading rate of the asphalt, which leads to a more rigid response and less strain.

Sensors 13 through 18 are used to capture the strains developed in Section 3 for the light vehicle passes. Sensor 13 and Sensor 16 were not working at this time so there is no data shown. Sensor 14 is placed on a crack in the longitudinal direction within the wheel path. Sensor 17 is also within the wheel path in the longitudinal direction but placed away from a crack. Sensor 15 is between the wheel paths on a crack in the longitudinal direction. Sensor 18 is between the wheel paths in the transverse direction. There is no reinforcement installed in Section 3.

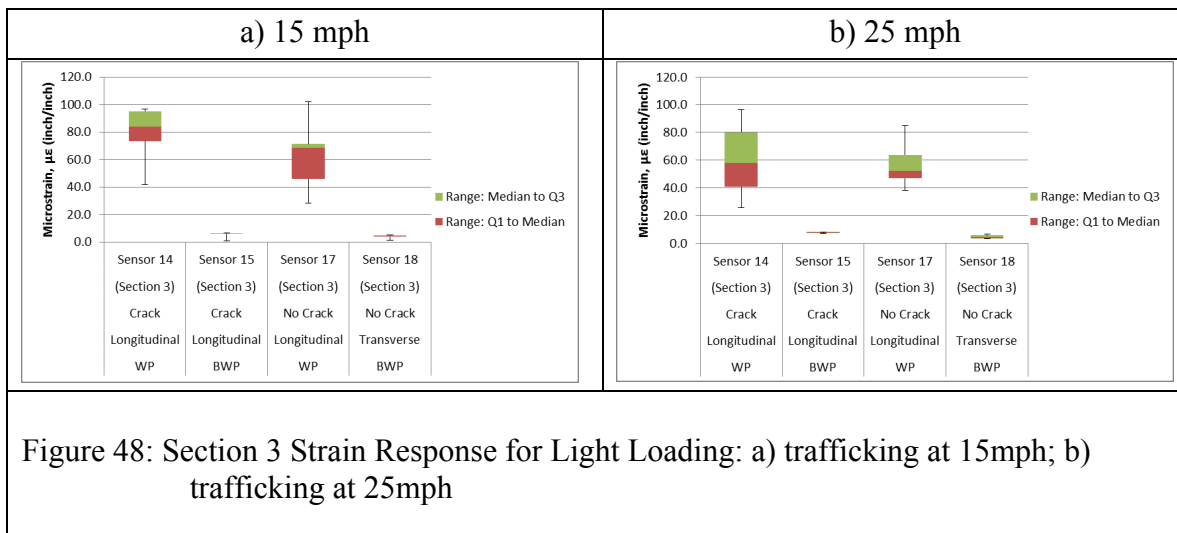


Figure 48: Section 3 Strain Response for Light Loading: a) trafficking at 15mph; b) trafficking at 25mph

Figure 48 a. shows the strain response for each of the working sensors within Section 3 during the 15mph passes. The maximum strain reading for each sensor in the order shown (Sensor 14, Sensor 15, Sensor 17, Sensor 18) is $97\mu\epsilon$, $7\mu\epsilon$, $102\mu\epsilon$, and $5\mu\epsilon$. Strain comparisons within this section include crack versus no crack, longitudinal versus transverse, and wheel path versus between wheel paths. Sensor 14 is on a crack in the wheel path and shows slightly lower strains than Sensor 17. This is not expected due to Sensor 14 being placed on a crack but the behavior can be unpredictable. Sensor 15 is also on a crack and shows slightly greater strains than Sensor 18. Unlike Section 2, there is no reinforcement. The lack of reinforcement allows sensors between the wheel paths to act more independently from loading within the wheel paths, so it is expected that the crack will have a greater effect on strain response. The strains measured from between the wheel paths are very small. This means the light load has a minimal effect on the area between the wheel paths.

Figure 48 b. shows the strain response for the same sensors during the 25mph passes. The maximum strain reading for each sensor in the order shown (Sensor 14, Sensor 15, Sensor 17, Sensor 18) is $96\mu\epsilon$, $8\mu\epsilon$, $85\mu\epsilon$, and $6\mu\epsilon$. Sensor 14 is on a crack in the wheel path and shows higher strain readings than Sensor 17. This is expected due to Sensor 14 being placed on a crack. Similar to the 15mph passes, Sensor 15 shows slightly greater strains than Sensor 18. There is no reinforcement in this section so the crack is expected to generate a greater strain response. The response from each of the sensors is very similar for the different vehicle velocities. This indicates that the loading rate effects are minimal with the lighter load.

5.1.1.3.2 Comparison of Strain Data among Different Test Sections

The comparison of strain data among different test sections for the light vehicle passes is the same as the section comparisons for the heavy vehicle passes. Note that Section 1 is reinforced with a polyester (PET) geosynthetic, Section 2 is reinforced with a polyvinyl (PVA) geosynthetic, and Section 3 is not reinforced.

5.1.1.3.3.1 Longitudinal Strain in Wheel Path

The longitudinal strain in the wheel path is measured by two sensors in each section. Sensor 4 and 6 are in Section 1, Sensor 7 and 11 are in Section 2, and Sensor 16 and 17 are in Section 3. Sensor 7, 11, and 16 did not work at the time of the light load passes so there is no data shown from them. Section 1 is reinforced with a polyester geosynthetic, Section 2 is reinforced with a polyvinyl geosynthetic, and Section 3 is unreinforced.

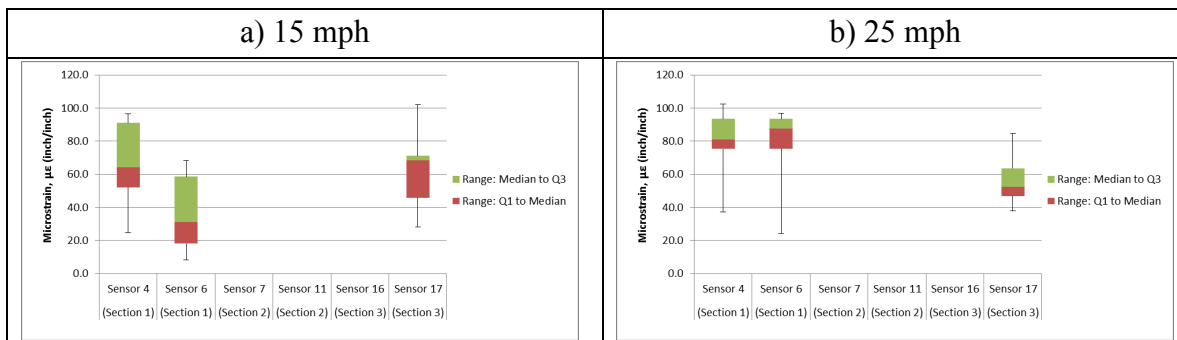


Figure 49: Longitudinal ASG in Wheel Path Not on Crack Section 1 and Section 3 for Light Loading: a) trafficking at 15mph; b) trafficking at 25mph.

Figure 49 a. shows the longitudinal strain gages in the wheel path placed away from a crack in Section 1 and Section 3. Sensor 17 shows the greatest maximum strain

response of $102\mu\epsilon$ followed by sensor 4 at $97\mu\epsilon$ and sensor 6 at $68\mu\epsilon$. The median value of Sensor 17 is also higher than the Section 1 sensors, but Sensor 4 has the highest third quartile value. Ignoring the consistently high strains shown by Sensor 4, this is the expected strain response of Section 3 compared to the reinforced Section 1.

Figure 49 b. shows the same sensors as before for the 25mph passes. Sensor 4 shows the greatest maximum strain reading of $103\mu\epsilon$ followed by Sensor 6 at $97\mu\epsilon$ and Sensor 17 at $85\mu\epsilon$. It is expected that there will be less strain from sensors within Section 1 due to it being reinforced but that is not the case here. The strains shown in Section 1 from the higher speed are larger than the strains from the lower speed. This is not expected because there is a faster loading rate that typically leads to a more rigid response and less strain development.

5.1.1.3.3.2 Transverse Strain between Wheel Paths

The transverse strain between the wheel paths is measured by Sensor 5 in Section 1, Sensor 12 in Section 2, and sensor 18 in Section 3. Sensor 5 did not work during the light load passes so no data is shown for that sensor. Section 2 is reinforced with a polyvinyl geosynthetic and Section 3 is unreinforced.

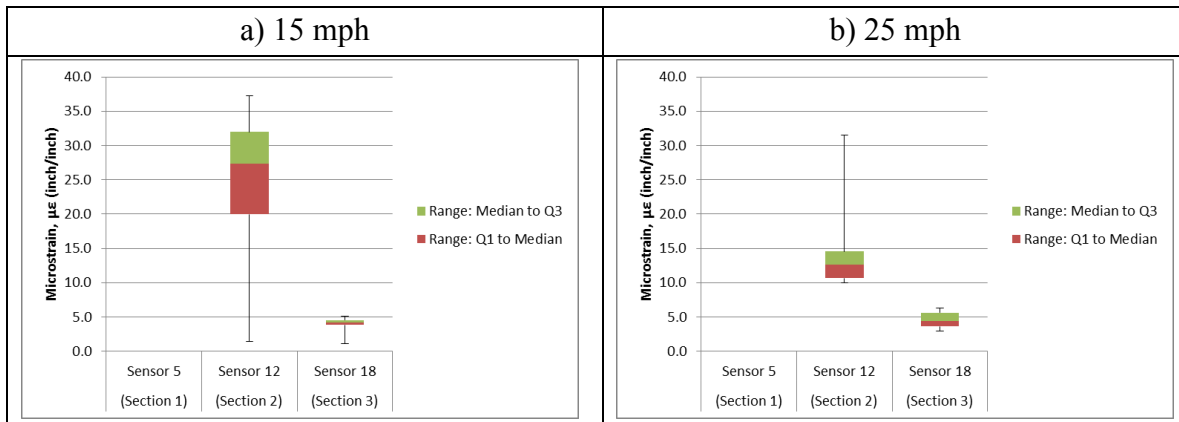


Figure 50: Transverse ASG Between Wheel Paths Not on Crack Section 2 and Section 3 for Light Loading: a) trafficking at 15mph; b) trafficking at 25mph.

Figure 50 shows the transverse strain gages located between the wheel paths away from a preexisting crack in Section 2 and Section 3. The low speed passes gave a maximum strain reading from Sensor 12 and 18 of $37\mu\epsilon$ and $5\mu\epsilon$, respectively. The high speed passes gave maximum strain readings of $32\mu\epsilon$ for Sensor 12 and $6\mu\epsilon$ for Sensor 18. The reinforcement within Section 2 transfers the stresses from the wheel path to the area between the wheel paths and renders greater strains in the transverse direction. The lack

of reinforcement within Section 3 causes the stresses and associated strains to act locally, therefore, the area between the wheel paths do not undergo significant strains. The difference between the two velocities do not significantly affect the strain measurements.

5.1.1.3.3.3 *Longitudinal Strain in Wheel Path on a Preexisting Crack*

The longitudinal strain in the wheel path on a preexisting crack is monitored by Sensor 1 from Section 1, Sensor 9 from Section 2, and Sensor 14 from Section 3. Sensor 9 does not work so there is only data shown from Sensor 1 and Sensor 14. Section 1 is reinforced with a polyester geosynthetic and Section 3 is unreinforced.

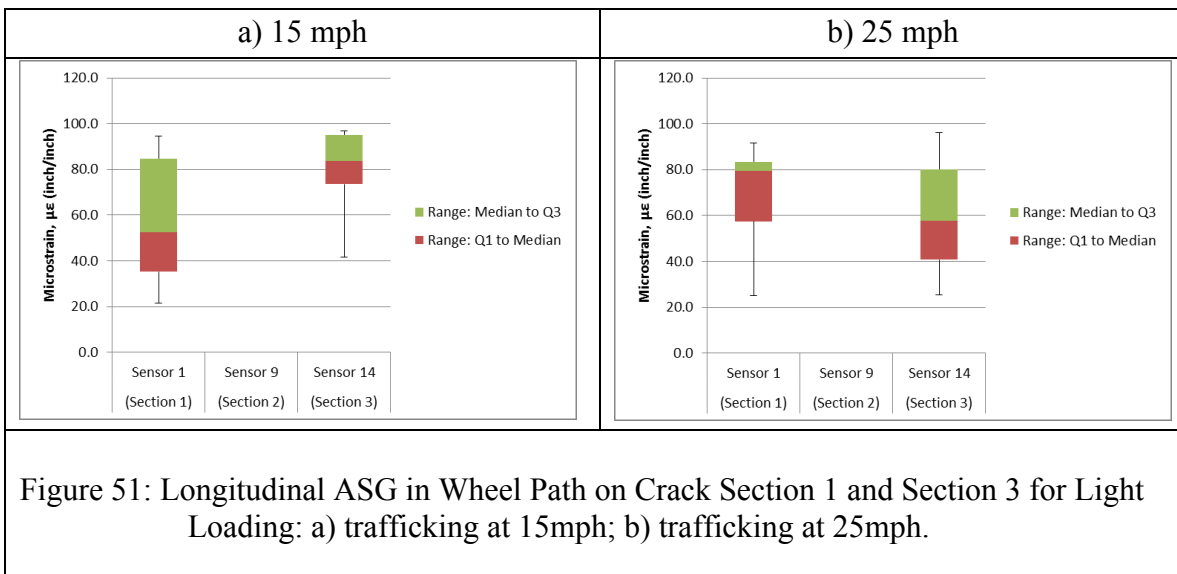


Figure 51 shows the longitudinal sensors in the wheel path placed on a crack for Section 1 and Section 3 during the light vehicle passes. For the 15mph passes, Sensor 1 has a maximum strain reading of 94μ ϵ and Sensor 14 shows 97μ ϵ . There is more variation in Sensor 1 than in Sensor 14 as well as a lower third quartile and median value. This is expected due to the reinforcement in Section 1. The reinforcement works to decrease the strains from a crack by distributing the induced stresses through the grid. The results from the 25mph passes are similar to the lower speed. Sensor 14 shows the greatest maximum strain reading of 96μ ϵ compared to Sensor 1 at 92μ ϵ . The effects of pass velocity do not seem to change the strain response for the light load.

5.1.1.3.3.4 *Longitudinal Strain between Wheel Paths on a Preexisting Crack*

The longitudinal strain between the wheel paths on a preexisting crack is measured by Sensor 2 from Section 1, Sensor 8 from Section 2, and Sensor 15 from Section 3. Sensor 2 from Section 1 did not work during testing so there is only data

shown from Sensor 8 and Sensor 15. Section 2 is reinforced with a polyvinyl geosynthetic reinforcement and Section 3 is unreinforced.

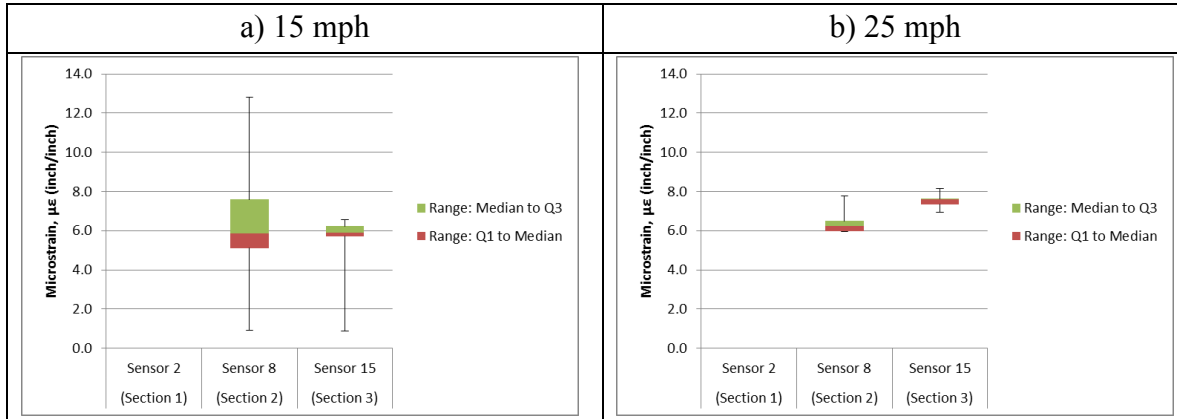


Figure 52: Longitudinal ASG Between Wheel Paths on Crack Section 2 and Section 3 for Light Loading: a) trafficking at 15mph; b) trafficking at 25mph.

Figure 52 shows the longitudinal strain gages located between the wheel path on a crack for Section 2 and Section 3 during the light vehicle passes. For the 15mph passes, Sensor 8 shows the highest maximum strain reading of $13\mu\epsilon$ compared to sensor 15 at $7\mu\epsilon$. This is a little more variable than the measured strains during the 25mph passes, in which both sensors show a max value of $8\mu\epsilon$. It is expected that Sensor 15 would have higher strains due to the lack of reinforcement on a crack, as shown by Figure 45: Longitudinal ASG Between Wheel Paths on Crack Section 2 and Section 3 for Heavy Loading: a) trafficking at 15mph; b) trafficking at 25mph. during the heavy load passes. The measured strains during this testing series are very small so the heavy load passes can be considered more reliable.

5.1.1.4 Effect of Driving Offset of Sensors

A loaded dump truck was used for the heavy load passes with a total weight of 48,460 lbs. This was done by marking the exact location of each of the sensors and laying out a pathway directly over each of the sensors in the wheel path. An experienced driver then carefully drove between the marked pathway and the white line for 10 passes at a lower speed of 15mph and 10 passes at a higher speed of 25mph. This was done for each of the three sections. The location of each pass was monitored via a camera overlooking the right side front tire and the location was noted based on its distance away from the white line.

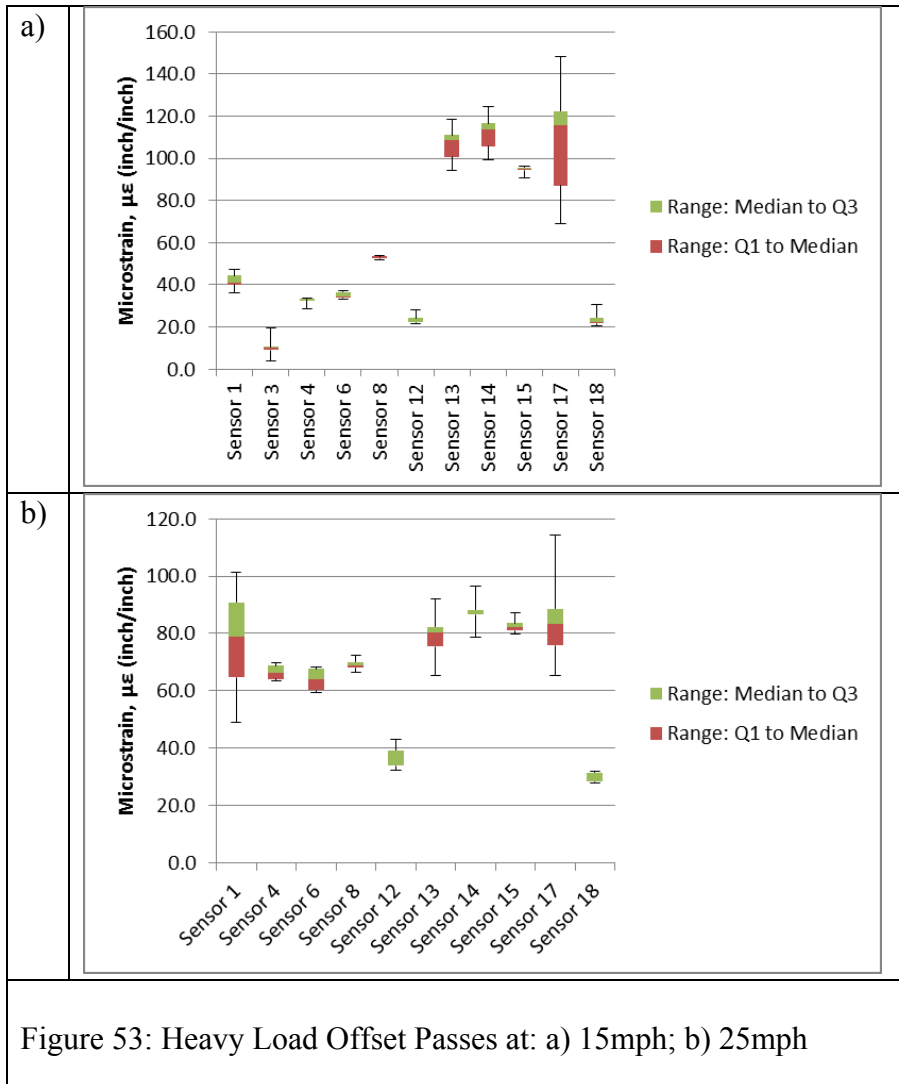


Figure 53: Heavy Load Offset Passes at: a) 15mph; b) 25mph

Figure 53 shows the offset passes for each sensor at 15 and 25mph. Note that Sensors 1 through 6 are from Section 1, Sensors 8 through 12 are from Section 2, and Sensors 13 through 18 are from Section 3. It is shown here that Section 1 is affected more by offset passes at a higher speed. The strain readings from Section 1 at the lower speed are all less than $60\mu\epsilon$, whereas the readings from the higher speed passes are between $60\mu\epsilon$ and $100\mu\epsilon$. Section 2 also shows an increased strain response from the higher speeds. At the lower speed, sensor 8 and 12 have strain readings around $5\mu\epsilon$ and $20\mu\epsilon$ respectively, but the readings are at $70\mu\epsilon$ and $40\mu\epsilon$ for the higher speed. Section 3 shows a trend that is opposite from the other two sections. It is shown on the first plot that Section 3 reaches strains at or above $120\mu\epsilon$ for the sensors within the wheel path, however they do not go above $120\mu\epsilon$ for the higher speed.

5.1.2 Falling Weight Deflectometer Tests

Falling Weight Deflectometer (FWD) tests were conducted directly on each of the working sensors. This included a series of 5 drops with 3 drops at a load of 6,000 lbs., 1 drop at 9,000 lbs., and the last drop at 12,000 lbs. The data acquisition system measuring strain response captured each of the drops from the FWD tests. Due to the consistency among the drops and the ability to target the exact location of the sensors, this testing series was expected to be conducted with comparatively higher precision as compared to traffic loading.

5.1.2.1 Data Analysis

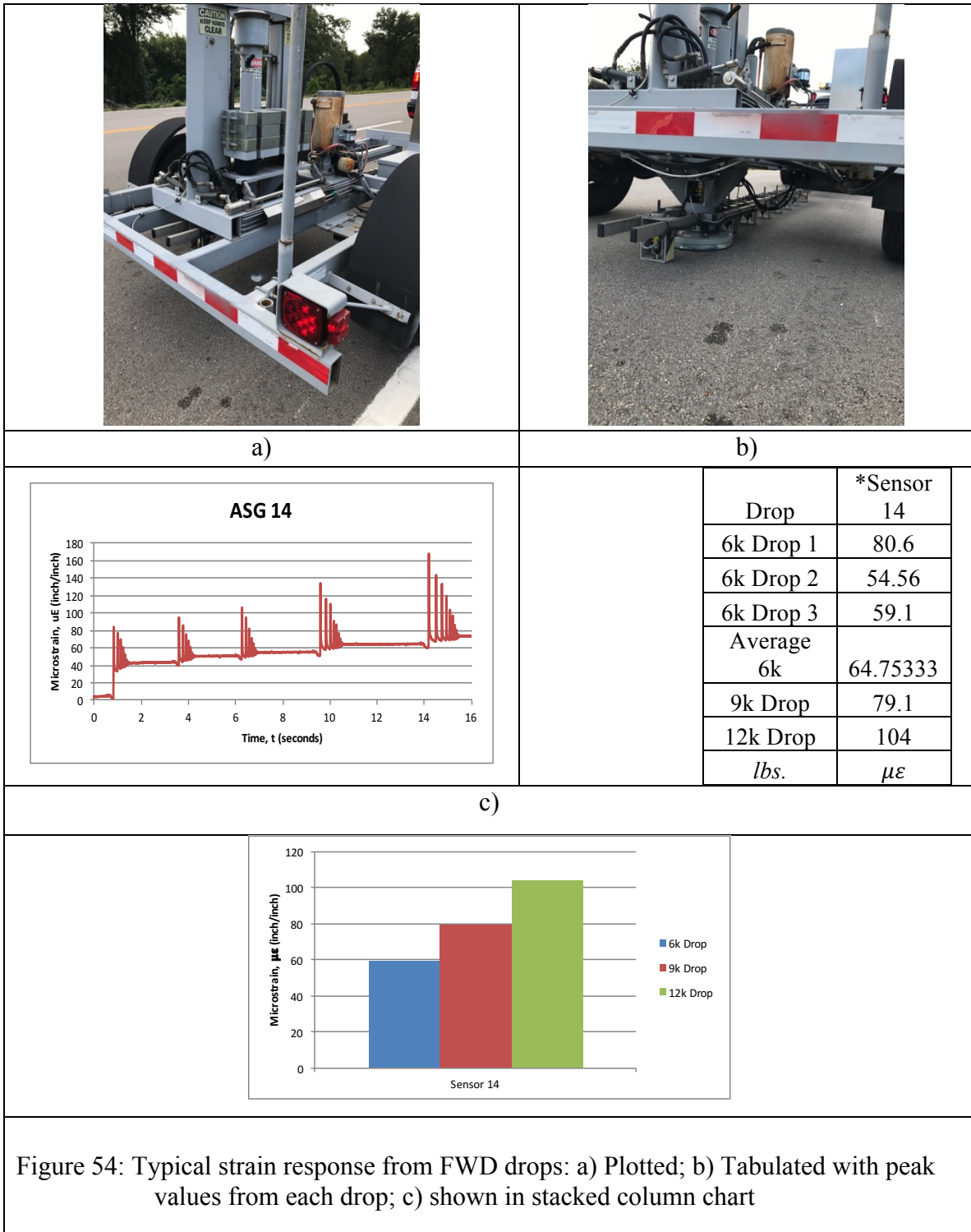


Figure 54: Typical strain response from FWD drops: a) Plotted; b) Tabulated with peak values from each drop; c) shown in stacked column chart

Figure 54 a. shows a typical strain response from the FWD drops. The plot is zeroed on the y-axis in order to show the only strains associated with the loading. As the drops were conducted, the weight would begin bouncing from the asphalt surface. That can be seen as the smaller spike directly following a peak value. The maximum value is taken from a given drop and plugged in to a table like the one shown in Figure 54 b. This is then plotted in a column chart as shown by Figure 54 c. The first column is measured strain from the third drop at 6,000 lbs. The middle column is the measured strain from the 9,000 lb. drop, and the third column section is the measured strain from the 12,000 lb. drop.

5.1.2.2 Comparison of Strain Data

The analysis of the FWD data is similar to the vehicle passes. It is divided in to four charts showing sensors from each section that have the same location, orientation, and proximity to preexisting cracks. The following list details each of the comparative models.

- a. Longitudinal ASG in Wheel Path Not on Crack
 - i. ASG 4, ASG 6
 - ii. ASG 7, ASG 11
 - iii. ASG 16, ASG 17
- b. Transverse ASG Between Wheel Paths Not on Crack
 - i. ASG 5
 - ii. ASG 12
 - iii. ASG 18
- c. Longitudinal ASG in Wheel Path on Crack
 - i. ASG 1
 - ii. ASG 9
 - iii. ASG 14
- d. Longitudinal ASG Between Wheel Paths on Crack
 - i. ASG 2
 - ii. ASG 8
 - iii. ASG 15

The first strain comparison is for longitudinal sensors placed within the wheel path away from a crack. The sensors with this configuration are Sensor 4 and 6 from Section 1, Sensor 7 and 11 from Section 2, and Sensor 16 and 17 from Section 3.

Unfortunately, Sensor 7, 11, and 16 did not work during the time of FWD testing so there is no data shown for those sensors.

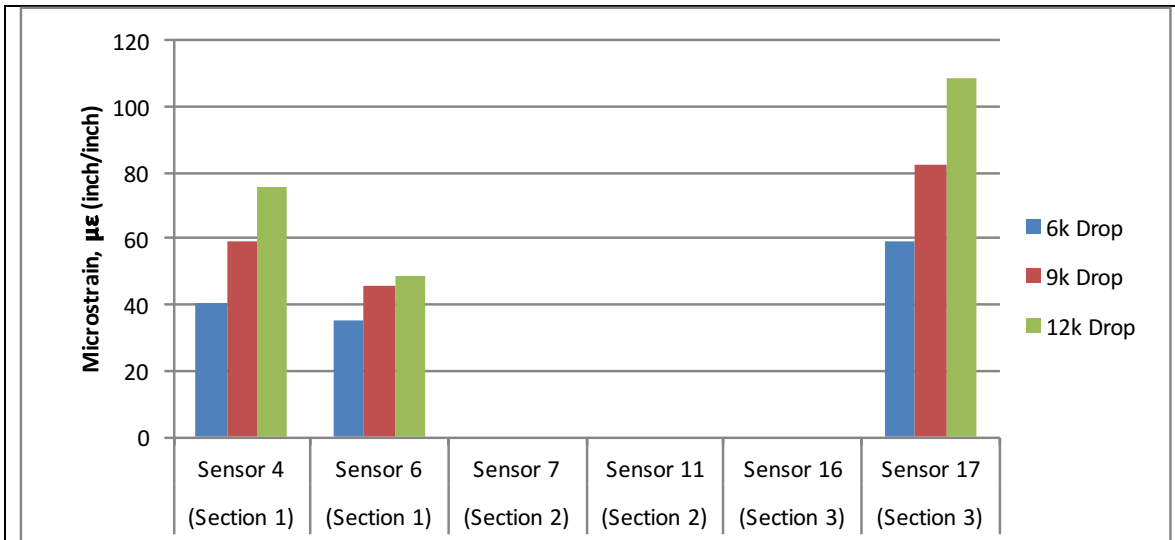


Figure 55: Longitudinal strain in wheel path away from a crack for FWD testing

Figure 55 shows longitudinal strain in the wheel path away from a crack. The working sensors are Sensor 4, Sensor 6, and Sensor 17. The measured strain for the 6,000 lb. drop for each sensor is 40 $\mu\epsilon$, 35 $\mu\epsilon$, and 59 $\mu\epsilon$, respectively. The measured strain for the 9,000 lb. drop is 59 $\mu\epsilon$, 46 $\mu\epsilon$, and 83 $\mu\epsilon$, respectively. Lastly, the measured strain for the 12,000 lb. drop is 75 $\mu\epsilon$, 48 $\mu\epsilon$, and 108 $\mu\epsilon$, respectively. Sensor 4 and Sensor 6 show a similar strain response for the 6k drop while Sensor 17 shows a value nearly 20 $\mu\epsilon$ higher. Sensor 6 then shows the least increase in strain from the 9k drop followed by Sensor 4 then Sensor 17. This trend continues with the final drop showing Sensor 17 with the greatest measured strain. This is similar to the trend seen from the heavy vehicle passes in which Sensor 17, within Section 3, has greater strains than the same sensors within Section 1. This is a different loading mechanism than the vehicle passes, in that the sensors undergo a point load and experience purely tensile strain. The reinforcement within Section 1 is expected to absorb some of the tensile stresses and that is indicated by the presented strain data.

The second comparison is for transverse sensors located between the wheel paths and away from a crack. The sensors with this configuration are Sensor 5 in Section 1, Sensor 12 in Section 2, and Sensor 18 in Section 3. Sensor 5 did not work during the time of testing so there is only data shown for Sensor 12 and 18.

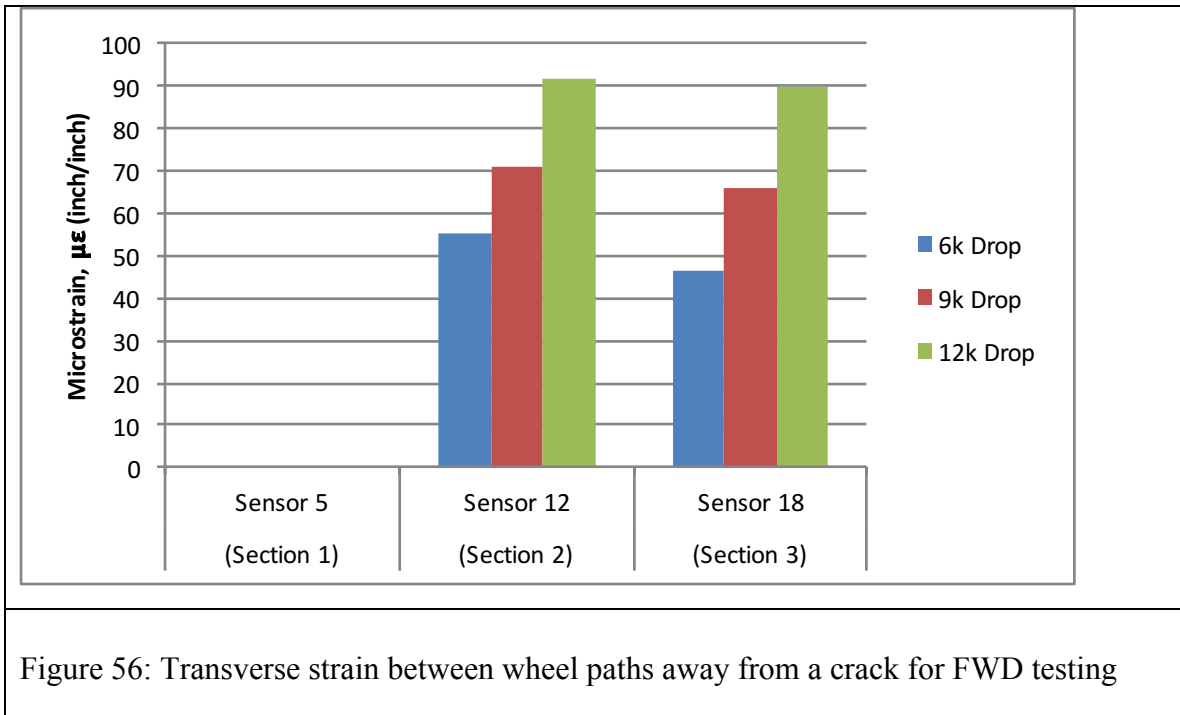


Figure 56: Transverse strain between wheel paths away from a crack for FWD testing

Figure 56 shows the transverse strains from between the wheel paths away from a crack. The working sensors in this configuration are Sensor 12 in Section 2 and Sensor 18 in Section 3. The measured strain for the 6,000 lb. drop is 55µε for Sensor 12 and 47µε for Sensor 18. The measured strain for the 9,000 lb. drop is 71µε for Sensor 12 and 66µε for Sensor 18. Lastly, the measured strain for the 12,000 lb. drop is 92µε for Sensor 12 and 90µε for Sensor 18. Sensor 18 shows a greater strain increase for the 9,000 and 12,000 lb. drop, but Sensor 12 still had the highest maximum strain measurement. Sensor 12 also showed greater strains during the vehicle passes, but the higher strain readings were attributed to load transfer through the reinforcement to the area between the wheel paths. It is expected that the FWD will cause less strain in Section 2 due to the reinforcement but that is not shown here.

The third comparison is for longitudinal sensors within the wheel path placed on a preexisting crack. The sensors with this configuration are Sensor 1 in Section 1, Sensor 9 in Section 2, and Sensor 14 in Section 3. Sensor 9 was not working during the time of FWD testing so there is only data from Sensor 1 and 14 shown.

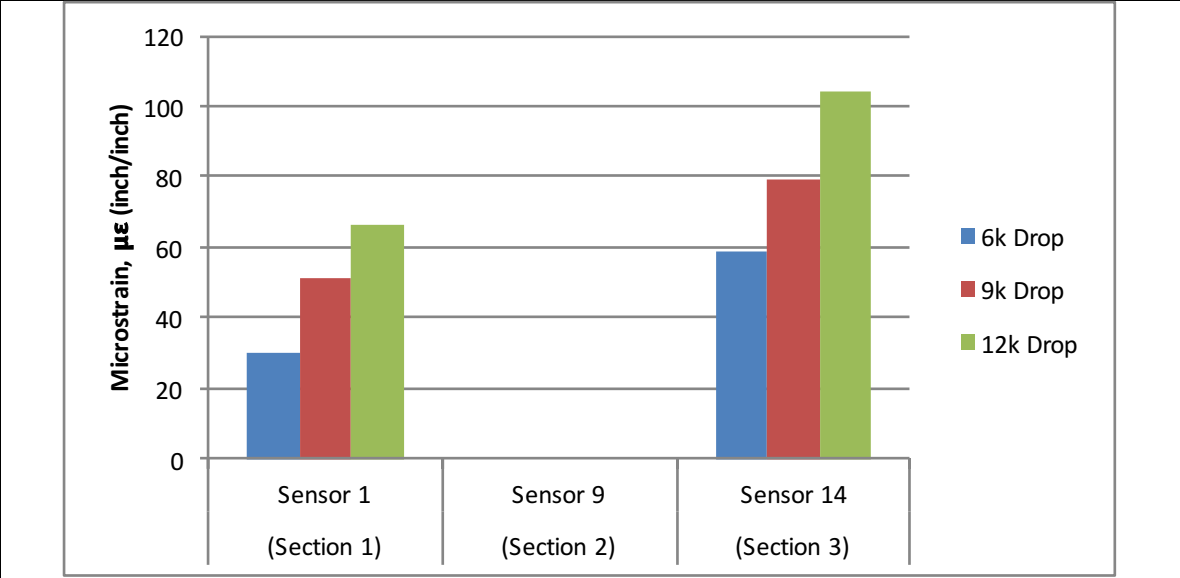


Figure 57: Longitudinal strain in wheel path on a crack for FWD testing

Figure 57 shows the longitudinal strain within the wheel path on a crack. The working sensors in this configuration are Sensor 1 in Section 1 and Sensor 14 in Section 3. The measured strain for the 6,000 lb. drop is 30με for Sensor 1 and 59με for Sensor 14. The measured strain for the 9,000 lb. drop is 52με for Sensor 1 and 79με for Sensor 14. Lastly, the measured strain for the 12,000 lb. drop is 66με for Sensor 1 and 104με for Sensor 14. Sensor 14 shows a significantly higher strain response than Sensor 1 for each energy level. This indicates that the reinforcement within Section 1 does not allow significant differential movement in the pavement at the crack location.

The last comparison is for longitudinal sensors located between the wheel paths placed on a crack. The sensors with this configuration are Sensor 2 in Section 1, Sensor 8 in Section 2, and Sensor 15 in Section 3.

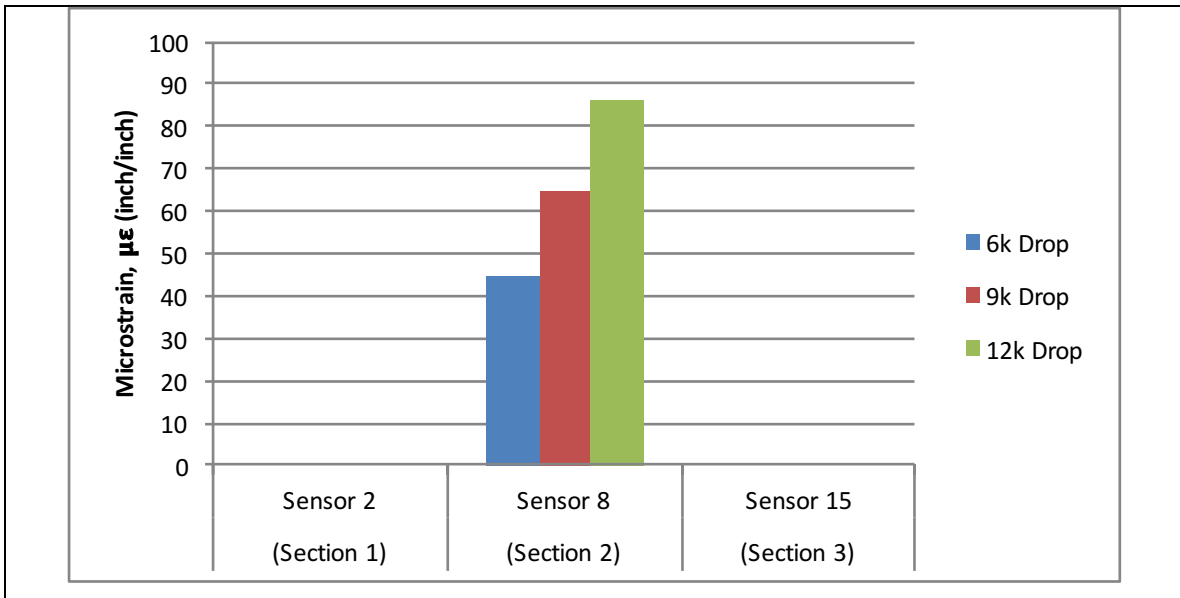


Figure 58: Longitudinal strain between wheel paths on a crack for FWD testing

Figure 58 shows the longitudinal strain between the wheel paths on a crack. Sensor 8 was the only working sensor in this configuration during the FWD testing. The measured strain for the 6,000, 9,000, and 12,000 lbs. drop is $44\mu\epsilon$, $65\mu\epsilon$, and $86\mu\epsilon$, respectively. This is greater than the measured strain response for Sensor 1, but less than Sensor 14. Although those sensors are within the wheel path and have experienced significantly more direct loading from traffic, it is still a fair comparison. This is also a very similar response to the measured strains from Sensor 12. It seems that the presence of a preexisting crack does not have a significant effect on the strain response.

5.1.3 Static Testing

Static testing was done using the same dump truck with the total weight of 48,460 lbs. The driver of the truck maneuvered directly on the wheel path with the passenger side tires. The truck moved forward at a slow speed until the front tire was directly over the sensors at which point the driver was instructed to stop for a two-second count. This was done for each of the four sensors located in the wheel path, and then conducted again for the second axle of the vehicle.

5.1.3.1 Data Analysis

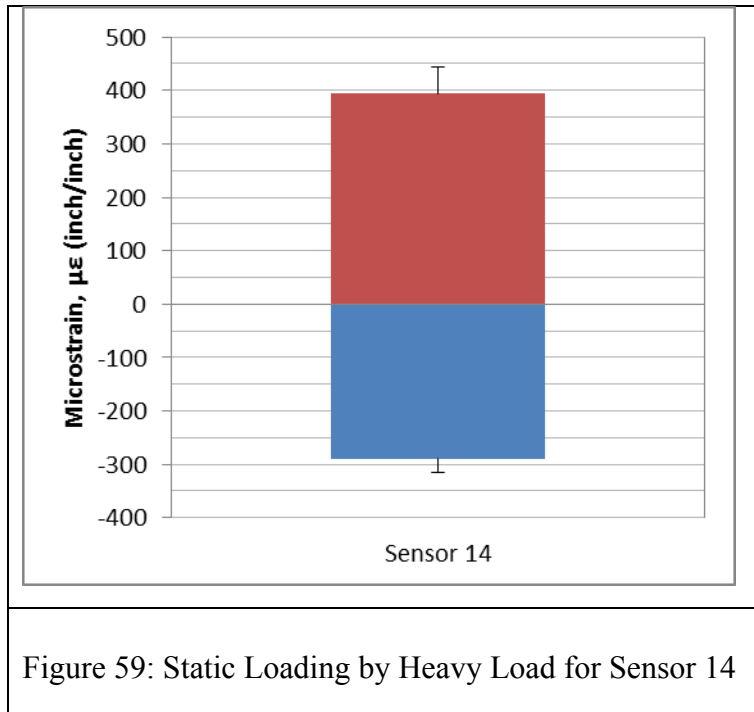


Figure 59: Static Loading by Heavy Load for Sensor 14

Figure 59 shows the strain readings for Sensor 14 from static testing with the dump truck. Positive strain values indicate tensile strain while negative indicates compressional strain. Each load cycle was conducted twice so the columns indicate the lower magnitude strains with the error bars extending to the maximum strain measured. The first axle of the dump truck was analyzed for the strain gages located in the wheel path, and the second axle was analyzed for the sensors between the wheel paths. This was done because the second axle showed a clearer strain response for the sensors between the wheel paths.

5.1.3.2 Comparison of Strain Data

The analysis of the static loading data is similar to the FWD and vehicle pass analysis. It is divided in to four charts showing sensors from each section that have the same location, orientation, and proximity to preexisting cracks. The following list details each of the comparative models.

- a. Longitudinal ASG in Wheel Path Not on Crack
 - i. ASG 4, ASG 6
 - ii. ASG 7, ASG 11
 - iii. ASG 16, ASG 17
- b. Transverse ASG Between Wheel Paths Not on Crack
 - i. ASG 5

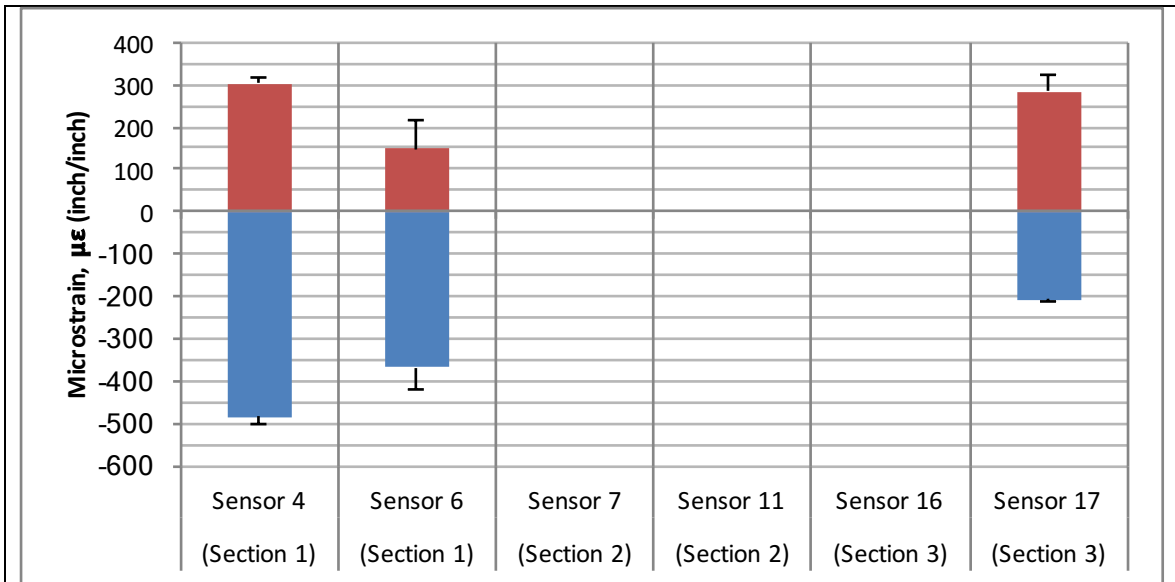


Figure 60: Longitudinal strain in wheel path away from a crack for static testing

Figure 60 shows the longitudinal strain readings from sensors in the wheel path away from a crack. The maximum tensile strain for each sensor in the order shown is $317\mu\epsilon$ for Sensor 4, $216\mu\epsilon$ for Sensor 6, and $323\mu\epsilon$ for Sensor 17. The maximum compressive strain for each working sensor is $-501\mu\epsilon$ for Sensor 4, $-422\mu\epsilon$ for Sensor 6, and $-210\mu\epsilon$ for Sensor 17. Sensor 17 shows the greatest tensile strain. This is expected due to the lack of reinforcement within Section 3. As seen from other testing series, Sensor 4 has a greater strain response than its repeat, Sensor 6. Both sensors in Section 1 have a significantly higher compressive strain response than Sensor 17 in Section 3. Although the reinforcement in Section 1 is not expected to provide compressive resistance, the strain magnitude is unusually high.

The second comparison is for transverse sensors located between the wheel paths and away from a crack. The sensors with this configuration are Sensor 5 in Section 1, Sensor 12 in Section 2, and Sensor 18 in Section 3. Sensor 5 was not working during the time of testing so there is only data shown for Sensor 12 and 18.

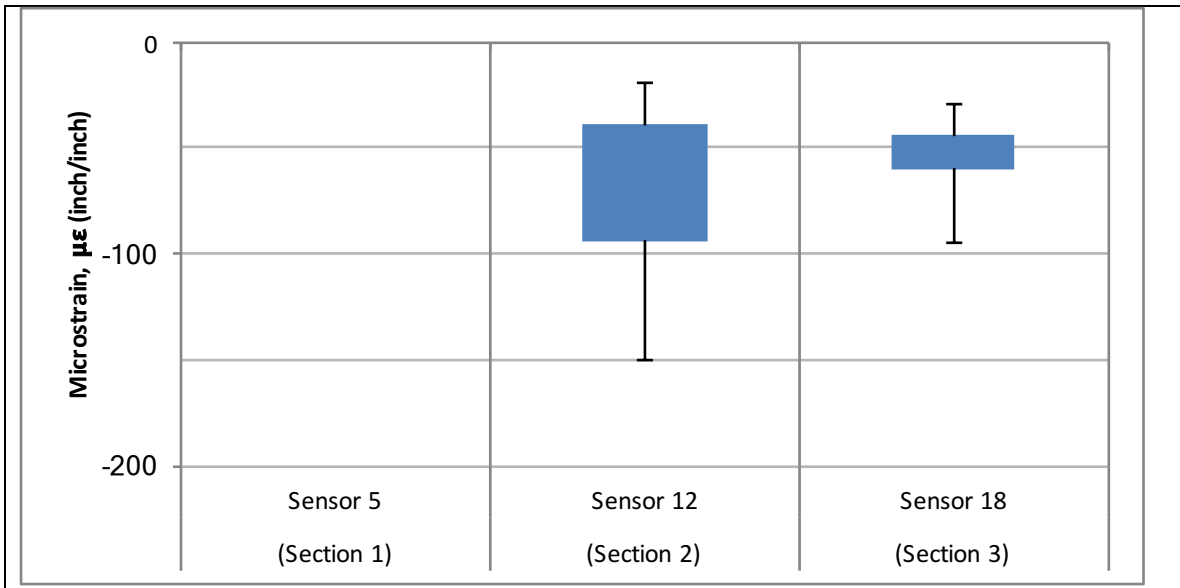


Figure 61: Transverse strain between wheel paths away from a crack for static testing

Figure 61 shows the transverse strains between the wheel paths during the static testing. The sensors remained in compression during the tests, so the upper end of the red column is the minimum compressive strain and the lower end is the maximum compressive strain with the error bars encompassing the total maximum and minimum compression from the two static passes. The maximum compressive strain measured for each sensor in the order shown is $-150\mu\epsilon$ for Sensor 12 and $-95\mu\epsilon$ for Sensor 18. Due to the reinforcement, Sensor 12 is more sensitive to wheel path loading because the load is transferred to the area between the wheel paths. The measured strains in Sensor 18 are relatively low when compared to the response from the vehicle passes so it is expected that there is more localized strain in the area of the wheel path that is not transferred to the area between the wheel paths.

The third comparison is for longitudinal sensors within the wheel path placed on a crack. The sensors with this configuration are Sensor 1 in Section 1, Sensor 9 in Section 2, and Sensor 14 in Section 3. Sensor 9 was not working during the time of static testing so there is only data from Sensor 1 and 14 shown.

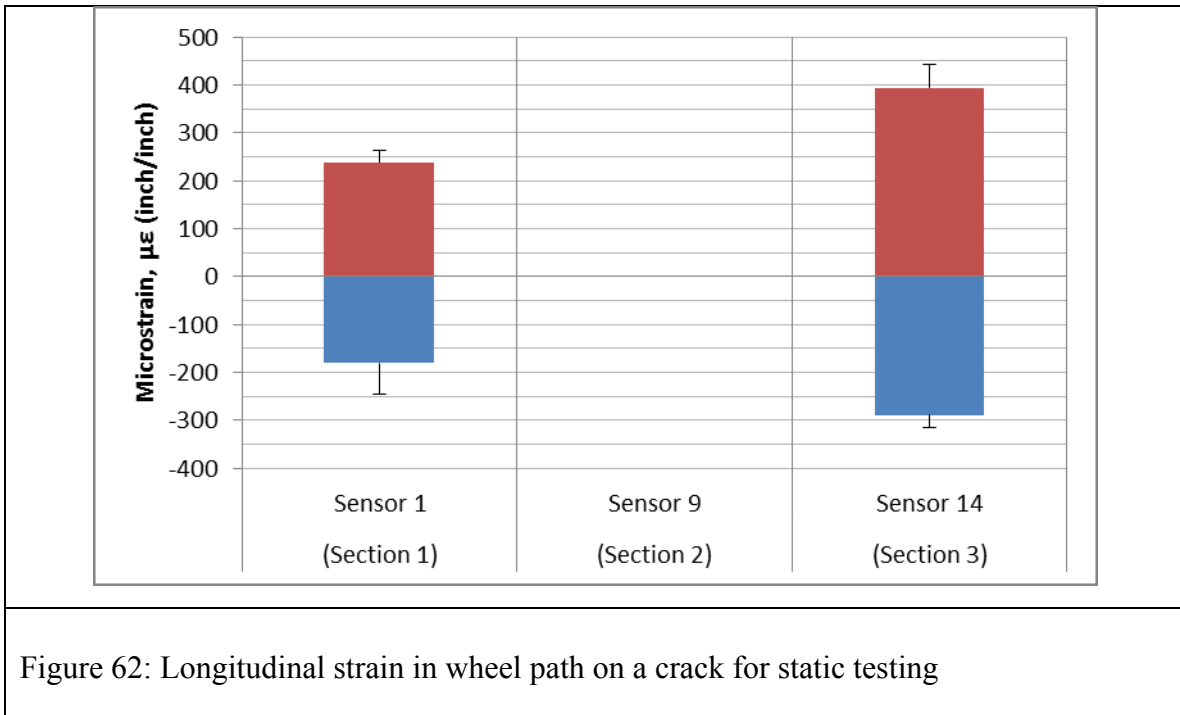


Figure 62: Longitudinal strain in wheel path on a crack for static testing

Figure 62 shows the longitudinal strains in the wheel path on a crack. The maximum tensile strain for each working sensor in the order shown is $262\mu\epsilon$ for Sensor 1 and $443\mu\epsilon$ for Sensor 14. The maximum compressive strain for each working sensor is $-246\mu\epsilon$ for Sensor 1 and $-316\mu\epsilon$ for Sensor 14. The lower tensile strain from Sensor 1 indicates that the reinforcement keeps the asphalt from undergoing movement. Sensor 14 shows high strain readings because there is no reinforcement and this may eventually lead to reflective cracking through the asphalt overlay.

The last comparison is for longitudinal sensors located between the wheel paths placed on a crack. The sensors with this configuration are Sensor 2 in Section 1, Sensor 8 in Section 2, and Sensor 15 in Section 3.

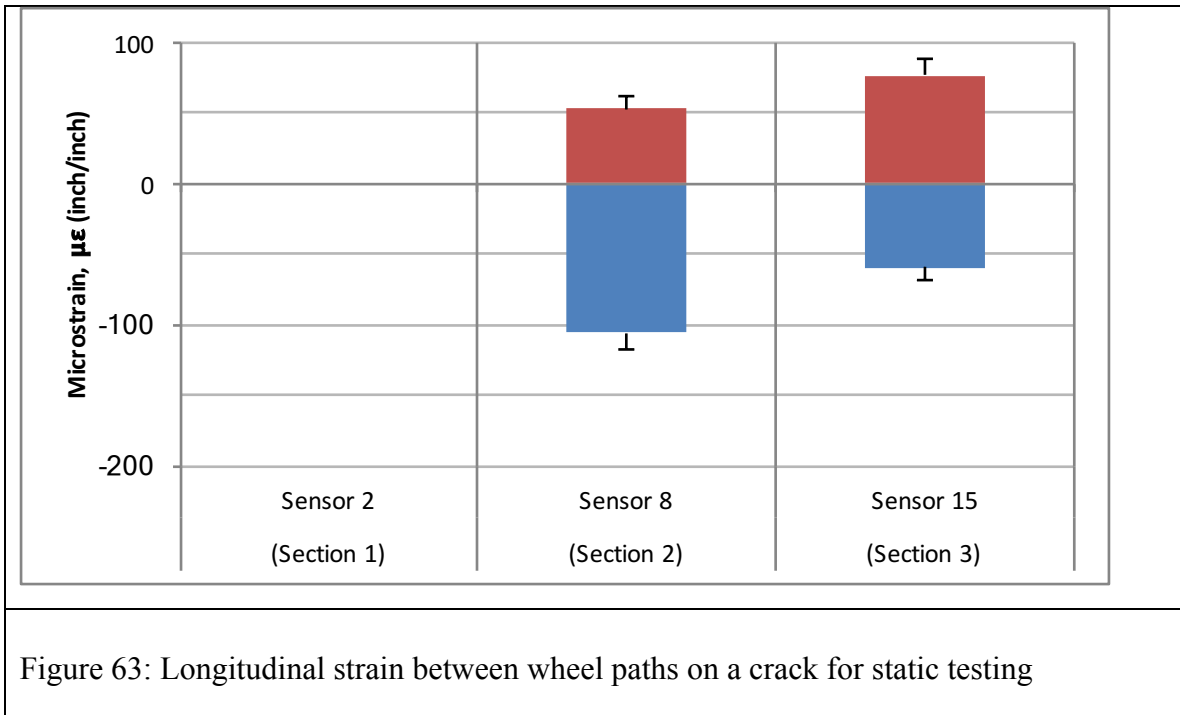


Figure 63: Longitudinal strain between wheel paths on a crack for static testing

Figure 63 shows the longitudinal strain from between the wheel paths on a crack. The maximum tensile strain from each working sensor in the order shown is $61\mu\epsilon$ for Sensor 8 and $88\mu\epsilon$ for Sensor 15. The maximum compressive strain is $-118\mu\epsilon$ for Sensor 8 and $-68\mu\epsilon$ for Sensor 15. It is expected that the reinforcement in Section 2 will decrease the amount of tensile strain from a crack and that is shown here.

5.2 DISCUSSION

The results of each testing series shed light on the benefits of interlayer geosynthetics. The two main benefits focused on during this study are the structural benefits shown by a decrease in tensile strain development, and the mitigation of reflective cracking shown by strain development on preexisting cracks.

5.2.1 Structural Benefits from Geosynthetics in Asphalt Overlays

Asphalt interlayer reinforcement provides a high tensile strength at low strains. As an asphalt layer experiences tensile stresses, the strength is mobilized and keeps the asphalt from straining in tension. Traffic loads cause the area below each wheel to experience vertical strains similar to a beam being loaded vertically. As a result, the strains in the horizontal direction are in compression at the top, and tension on the bottom with the neutral axis being somewhere in the middle. The reinforcement is placed at an area under tension but allows less tensile strain for a given stress,

therefore the asphalt experiences less strain. This allows the bitumen to maintain its bond with the aggregates for more loading cycles which increases the fatigue life of the asphalt thus providing a structural benefit.

The sensors that were directly loaded during each of the testing series show that there is less tensile straining in the reinforced sections. These sensors include the longitudinal strain gages in the wheel path in Section 1 and Section 3. In most cases, Sensor 17 showed greater tensile strains than Sensor 4 and Sensor 6.

Another indication of the structural benefits of reinforcement is the load transfer to the area between the wheel paths. Sensor 5 and Sensor 12 showed greater strains than Sensor 18 during the vehicle passes. The load beneath the wheel is spread through the reinforcement across a greater area, which will eventually lead to decreased rutting in the wheel paths.

5.2.2 Mitigation of Reflective Cracks by Geosynthetics in Asphalt Overlays

Cracks within a roadway create a discontinuity in the asphalt layers. When an overlay is constructed where there are preexisting cracks, it becomes the only continuous layer. Wheel loads begin to induce bending and shear stresses at the crack location, and these stresses are transferred through the overlay, thus leading to reflective cracking. Asphalt interlayer reinforcement provides an additional layer that extends across preexisting cracks. As a crack tip reaches the interlayer, the stresses are then transferred laterally through the length of the reinforcement. This keeps the crack from extending through the new overlay and increases its service life.

The sensors that were placed on a crack within reinforced sections show less tensile straining than the unreinforced section. In each of the testing series, Sensor 1 showed less tensile strains than Sensor 14. Similarly, Sensor 8 exhibited less tensile strain than Sensor 15. This indicates that the reinforcement in Section 1 and Section 2 performed well by providing additional strength and relieving the stresses across a discontinuous layer.

Chapter 6. Conclusions

This research included the construction of two inch-thick asphalt overlays reinforced using polyester (PET) and polyvinyl (PVA) geosynthetic interlayers to be compared with an unreinforced control section. 500 ft. sections of the PET and PVA reinforcement were placed in sequence with the control. These test sections were constructed in an area within a road overlay project that had comparatively small elevation changes, road curvature, and uniform subsurface conditions.

Each of the monitored sections contained six asphalt strain gages. These asphalt strain gages were arranged in a configuration that included two longitudinal strain gages in the wheel path, one transverse strain gage in the wheel path, one transverse strain gage between the wheel paths, one longitudinal strain gage in the wheel path on a crack, and one longitudinal strain gage between the wheel paths on a crack for each section. This configuration was chosen to observe the strain development from different orientations and locations in the road in order to understand the structural benefits of reinforcement. Strain gages were placed over preexisting cracks to provide information on the reinforcement's ability to retard reflective cracks.

A series of controlled field tests was conducted with the assistance of TxDOT to measure the strains developed in each section by different loading mechanisms. The first test series involved vehicle passes by a heavy vehicle. The passes were conducted at different velocities and locations within the lane. The next test series involved passes by a light vehicle. These passes were also conducted at different speeds. Static loading was then conducted by the heavy vehicle. The last testing series involved FWD loading directly on each sensor.

The overall purpose of this research was to evaluate the effect of interlayer reinforcements on the strain development within the asphaltic layer. Specifically, the strain gages installed within the preexisting asphalt allowed evaluation of the development of strain within the old asphalt. These strain gages were arranged in a way that can provide evidence of performance under different loading conditions. Based on the analysis of the strain measurements, the following conclusions can be made:

- Evaluation of the data obtained from the heavy load passes, light load passes at 15mph, FWD loading, and static loading indicated that the longitudinal strains in the wheel path were greater in the unreinforced section than in the PET section. This finding suggests that the PET reinforcement minimizes the development of tensile strains within the asphaltic layer. This is expected to lead to an extended design life of the pavement due to the decreased fatigue.

- Evaluation of the data obtained from the heavy load, light load, and static passes for the PVA reinforcement, and the heavy load passes for the PET section indicates that the transverse strains between the wheel paths were greater in the PET and PVA reinforced section than the unreinforced section. This finding suggests that the reinforcement led to a distribution of stresses over a comparatively larger area, which is beneficial to minimize rutting depth.
- The longitudinal strains in the wheel path at the location of preexisting cracks were found to be greater in the unreinforced section than in the PET section. This finding suggests the PET reinforcement mitigated the stresses induced by traffic in the cracked asphalt, which may lead to decreased rate of crack propagation. This observation was made based on the data obtained from the heavy load passes, light load passes, FWD loading, and static loading.
- Longitudinal strains between the wheel paths at the location of preexisting cracks were found to be greater in the unreinforced section than in the PVA reinforced section. This indicates the PVA reinforcement distributed the bending and shear stresses and may lead to decreased crack propagation. This observation was made in the data obtained from the heavy load passes, light load passes at 25mph, and the static loading.

Overall, the geosynthetic-reinforcement layer provided additional tensile strength to the asphaltic layer, resulting in lower tensile strains and, consequently, longer fatigue lives. Additionally, the geosynthetic-reinforcement caused the asphalt to behave as a system of relatively uniform stresses by distributing them across a comparatively larger area. This led to reduction of peak strain values, which can lead to reduced permanent deformations. The decreased strains developed within the wheel paths for the PET section compared to the unreinforced section provides evidence for the structural benefits added by the reinforcement. The increased strain response between the wheel paths from both reinforced sections as compared to the control section indicate that the reinforced sections behave more uniformly.

Cracks within a road establish a discontinuity in the asphalt layers. Construction of an overlay on preexisting cracks result in a continuous layer of small thickness. Wheel loads begin to induce bending and shear stresses at the crack location and these stresses are transferred through the overlay, thus leading to reflective cracking. Asphalt interlayer reinforcement is intended to provide an additional layer that extends across preexisting cracks. As a crack tip reaches the interlayer, the stresses are then transferred laterally through the length of the reinforcement. This slows the crack development into the new overlay and increases its service life. This is evidenced by a decreased tensile strain

response on preexisting cracks within the PET and PVA reinforced pavement sections compared to the unreinforced pavement section. Low tensile strains minimize crack widening.

The observations and correlations from this experiment correspond to the specific pavement structure and materials used in this study. Extrapolation of the results from this research to other materials requires careful considerations. Recommendations for further analysis of the performance of interlayer geosynthetics in a field site include the use of different geogrid polymers types and varying overlay thicknesses. Furthermore, the installation of additional strain gages would be beneficial to account for malfunctioning of sensors after their installation.

References

- Al-Qadi, Dessouky, Kwon, and Tutumluer. 2008. "Geogrids in flexible pavements: validated mechanism." (Transportation Research Record 2045) 102-109.
- Brown, Thom, and Sanders. 2001. "A study of grid reinforced asphalt to combat reflection cracking." *The Association of Asphalt Paving Technologies* 543-569.
- Chen, Tebaldo, Roque, Lopp, and Exline. 2013. *A mechanistic test to evaluate effects of interface condition characteristics on hot-mix asphalt overlay reflective cracking performance*. Road Materials and Pavement Design.
- Correia, Natalia. 2014. *Performance of flexible pavements enhanced using geogrid-reinforced overlays*. University of Sao Paulo.
- Ferrotti, Canestrari, Pasquini, and Virgili. 2012. "Experimental evaluation of the influence of surface coating on fiberglass geogrid performance in asphalt pavements." *Geotextiles and Geomembranes* 11-18.
- Jones, Louw, and Wu. 2016. *Full-Depth reclamation: cost effective rehabilitation strategy for low-volume roads*. Journal of the transportation research board.
- Khodaii, Ali, Shahab Fallah, and Nejad. 2009. "Effects of geosynthetic on reduction of reflection cracking in asphalt overlays." *Geotextiles and Geomembranes*.
- Montestruque, Bernucci, Fritzen, and Goretti da Motta. 2012. *Stress relief asphalt layer and reinforcing polyester grid as anti-reflective cracking composite interlayer system in pavement rehabilitation*. RILEM International Conference on Cracking in Pavements.
- Nguyen, Blanc, Kerzreho, and Hornyh. 2013. "Review of Glass Fiber Grid use for Pavement Reinforcement and APT Experiments at IFSTTAR." *Road materials and Pavement Design* (IFSTTAR).
- Paris, and Erdogan. 1963. "A critical analysis of crack propagation laws." *Journal of Basic Engineering*.
- Perkins, Christopher, Thom, Montestruque, Korkiala-Tanttu, and Want. 2010. "Geosynthetic in pavement reinforcement applications." *Proceedings of the 9th International Conference on Geosynthetic* 1: 165-192.
- Roodi. 2016. "Analytical, experimental, and field evaluations of soil-geosynthetic interaction under small displacements." *Ph.D dissertation* (Univ. of Texas, Austin).

- Roodi, and Zornberg. 2017. "Stiffness of soil-geosynthetic composite under small displacements: II. Experimental Evaluation." *JGGE* 143 (10).
- Roodi, Morsy, and Zornberg. 2017. "Experimental Evaluation of the Interaction between Geosynthetic Reinforcements and Hot Mix Asphalt." *International Conference on Highway Pavement & Airfield Technology* (ASCE) 428-439.
- Scholz. 2010. "Instrumentation for Mechanistic Design Implementation." (Transportation Research and Education Center).
- Sobhan, and Tandon. 2008. *Mitigating reflection cracking in asphalt overlays using geosynthetic reinforcements*. Lavoisier, Paris: Road Materials and Pavement design.
- Timm, Priest, and McEwen. 2004. *Design and instrumentation of the structural pavement experiment at the NCAT test track*. NCAT.
- Vanelstraete. 2000. *On site behaviour of interface systems*. Ottawa: 4th international RILEM conference.
- Vismara, Molenaar, Crispino, and Poot. 2012. *Toward a better understanding of benefits of geosynthetics embedded in asphalt pavements*. Washington, DC: Journal of the Transportation Research Board.
- Willis, and Timm. 2009. *Repeatability of asphalt strain gauges*. NCAT.
- Zamora-Barraza, Caldaza-Perez, Castro-Fresno, and Vega-Zamanillo. 2010. "New procedures for measuring adherence between geosynthetic material and a bituminous mixture." *Geotextiles and Geomembranes* 483-489.
- Zamora-Barraza, Calzada-Perez, Castro-Fresno, and Vega-Zamanillo. 2011. "Evaluation of anti-reflective cracking systems using geosynthetics in the interlayer zone." *Geotextiles and Geomembranes*.
- Zhang, Liu, Huang, and Fu. 2012. *Rubber modified asphalt mixture properties and mechanical testing*. Trans Tech Publications.
- Zornberg, Roodi, and Gupta. 2017. "Stiffness of soil-geosynthetic composite under small displacements: I. Model development." *JGGE* 143 (10).
- Zornberg. 2017a. "Functions and applications of Geosynthetics in Roadways: Part 1." *Geosynthetics, Industrial Fabrics Association International* 34-40.
- Zornberg. 2017b. "Functions and Applications of Geosynthetics in Roadways: Part 2." *Geosynthetics, Industrial Fabrics Association International* 34-40.

Zornberg, Roodi, Ferreira, and Gupta. 2012. "Monitoring performance of geosynthetic-reinforced and lime-treated low-volume roads under traffic loading and environmental conditions." *Proc. Geo-Congress* 1310-1319.